DYNAMIC SOIL MODELING IN SITE RESPONSE AND SOIL-LARGE PILE INTERACTION ANALYSIS

BY

CAMILO ANDRES PHILLIPS

DISSERTATION

Submitted in partial fulfillment of the requirements
for the degree of Doctor of Philosophy in Civil Engineering
in the Graduate College of the
University of Illinois at Urbana-Champaign, 2012

Urbana, Illinois

Doctoral Committee:

Professor Youssef M. A. Hashash, Chair and Director of Research
Associate Professor Scott M. Olson, Co-director of Research
Professor Erol Tutumluer
Professor Emeritus Jamshid Ghaboussi

ABSTRACT

The present research explores the use of numerical solutions in two geotechnical earthquake engineering problems; 1) one dimensional wave propagation in soil deposits and 2) the effects of lateral spreading on large pile foundations.

Two new soil damping formulations are implemented in non-linear one-dimensional site response analysis for small and large strains. The first formulation introduces an approach to construct a frequency-independent viscous damping matrix which reduces the over-damping at high frequencies, and therefore, the filtering at those frequencies. The second formulation introduces a reduction factor that modifies the extended Masing loading/unloading strain-stress relationship to match measured modulus reduction and damping curves simultaneously over a wide range of shear strains. A set of examples are introduced to illustrate the effect of using the two proposed formulations, separately and simultaneously, in non-linear site response analyses.

Three-dimensional numerical models are developed and calibrated using the displacement, acceleration, and pore water pressure time histories recorded in a free-field lateral spreading centrifuge test. The calibration process highlights the important role of small strain damping and the need for pressure-dependent dilation parameters to simultaneously provide the best match for measurements of pore water pressure, acceleration, and lateral displacement. The calibrated numerical model is then used to predict another free-field lateral spreading centrifuge test using the same soil profile but different input acceleration time history. The computed response shows good agreement with the centrifuge test measurements.

Lateral pressures induced by lateral spreading soils against large piles are estimated using the results of three-dimensional numerical simulations. The numerical simulations were calibrated and evaluated using displacement, acceleration, and pore water pressure time histories recorded from lateral spreading centrifuge tests with a large, rigid deep foundation element located in the path of downslope soil movement. The calibration process highlighted the important role of soil-pile interface modeling to simultaneously provide the best match for measurements of pore water pressure, acceleration, and lateral displacement. The numerical model is then employed to determine the effects of using representative permeability values and broadband input motions. Pressures extracted from these numerical analyses are used to

determine pressure profiles and bending moments and compared with current recommendations (i.e. strain wedge method and triangular net pressure distribution). The computed response agrees well with the results of the strain wedge method for the upslope side of the pile and shows the need for adjusting the triangular pressure method to estimate the lateral loads and bending moment in the pile at different depths by introducing a depth-dependent coefficient.

ACKNOWLEDGMENTS

I would like to express profound gratitude to my advisors Professors Youssef M. A. Hashash and Scott M. Olson for giving me the opportunity to be a part of this project and all the guidance and support he has given me along the way. Thanks to their advice I am leaving Urbana with a new set of tools that are going to be fundamental in this new stage of my life. I appreciate the guidance and support of my Ph.D. committee members Professors Erol Tutumluer and Jamshid Ghaboussi.

I would like to give special thanks to my family, for being incredibly supportive and patient during the course of this Ph.D. program and for reminding me that family and relationships are the real important things in life. Mother, Juan and Maxi I will be in debt all my life with the three of you, there were many times that I was going to give up but you kept me going, I know that I do not say often but you know how much I love you.

To my family at Urbana: Catalina Londoño, Gonzalo Gallo, Sara Alzate, Silvia Remolina, Juan E. Velasquez, Katia Curbelo, Andres Montaña, Juan S. Mejia, Laura Atuesta, Carlos Gomez and David Groholski I cannot express in words how grateful I am, you were with me in all the good and the bad days, giving me love, energy and support. For me Urbana will be always one of the most special places because here I had the opportunity to meet you all. To my friends: Mariela Suarez, Sebastian Loboguerrero, Camilo Quiñones, Luis F. Molina, Santiago Arambula and Esteban Ucros although we have been far away I always have felt that if I need something you are always there for me. I consider all you my brothers and sisters; I hope that you know that you can always count with me and that you will always have a home wherever I am.

Thanks to my officemates and the many friends that I met in the past five years for the help and the opportunity of sharing so many good moments.

Finally I want to dedicate this work to my father who died in January of 2007, he were one of the most amazing persons that I ever knew, I learned so many things from him and today I feel sad to know that I cannot call him to tell him that I am writing these final words in my dissertation and to my two beautiful nephews Simon and Alejandro because they bring joy to my life.

TABLE OF CONTENTS

LIST OF TABLES

LIST OF FIGURES

CHAPTER 1 - INTRODUCTION

Although it is impossible to prevent the occurrence of earthquakes, it is possible to reduce the loss of life, injuries and damages associated with strong motion shaking by means of realistic ground motion prediction for future earthquakes and the estimation of the impact on the built environment, which can be only achieved by combining source, wave-propagation, site-response and soil-structure interaction. The present research explores the use of numerical solutions in two geotechnical earthquake engineering problems; 1) one dimensional wave propagation in soil deposits and 2) the effects of lateral spreading on large pile foundations. The aforementioned problems are computationally mutually exclusive and require the use of different approaches and numerical techniques. Therefore, to assure clarity it has been decided to discuss each problem separately and divide this dissertation document into different parts.

1.1 Simplified soil modeling for nonlinear 1D site response analyses

Measurements and observations of ground shaking during large earthquakes have demonstrated the predominant role of site effects in the response of infrastructure during a seismic event. Despite significant efforts to model the hysteretic response and nonlinearity of soils due to medium and large ground motions, the most widely accepted nonlinear site response methods are not able to represent simultaneously the changes of stiffness and energy dissipation (damping) observed in both laboratory tests and during earthquake events.

In this thesis two new soil damping formulations have been developed to correctly represent the observed soil behavior for small and large strains respectively. These formulations have been implemented in the site-response analysis software DEEPSOIL [Hashash, (2006)]. The first formulation introduces an approach to construct a frequency-independent viscous damping matrix to reduce the over-damping at high frequencies, and therefore, the filtering at those frequencies. The second formulation modifies the extended Masing loading/unloading strain-stress relationship to match measured modulus reduction and damping curves simultaneously over a wide range of shear strains.

Chapter 2 presents two new soil damping formulations implemented in non-linear one-dimensional site response analysis for small and large strains. The first formulation introduces an approach to construct a frequency-independent viscous damping matrix which reduces the over-

damping at high frequencies, and therefore, the filtering at those frequencies. The second formulation introduces a reduction factor that modifies the extended Masing loading/unloading strain-stress relationship to match measured modulus reduction and damping curves simultaneously over a wide range of shear strains. A set of examples are introduced to illustrate the effect of using the two proposed formulations, separately and simultaneously, in non-linear site response analyses.

1.2 Liquefied soil-large pile interaction analysis

Population growth especially in urban regions has led to the need for more and larger bridges, buildings, roadway embankments, pipelines, etc. For bridges, increasing spans and traffic volumes result in greater foundation design loads (static and seismic lateral forces) leading to the use of large, rigid foundations (e.g., large diameter drilled shaft groups; large, closely spaced driven pile groups; or large-dimension dredged caissons) as a design solution.

Lateral displacement of gently sloping ground triggered by seismic shaking – referred to as lateral spreading – imposes large bending moments and causes serious damage to deep foundation systems and their superstructures. Although it is possible to predict if these lateral spreads will occur for a given earthquake and soil conditions the design of pile foundations in liquefied soils also requires reliable methods to calculate the effects of earthquake shaking (e.g. liquefaction induced pressures) and post-liquefaction displacements on pile foundations.

Available approaches to design flexible piles in lateral spreading soils have not been extended to nor tested for rigid foundations subjected to lateral spreading loads. Not being able to estimate earth pressures against these large foundations constitutes a major obstacle for engineering practitioners leading to "experienced guesses" which often result in highly conservative designs hindering the possibility of developing cost-effective solutions and/or mitigation alternatives.

Although in-situ blast tests and nearly full-scale shaking table experiments have shed much light on the interaction of flexible piles subjected to lateral spreading pressures, technical and economic constraints and the lack of control of the variables involved in the test hinder the application of these techniques in attempting to understand the interaction of rigid foundations and lateral spreading soils. The most common alternative to overcome the aforementioned

constraints has been the design of small scale centrifuge tests in which the controlling factors (i.e. stress and strain conditions) are modeled correctly by means of scaling of gravitational forces. Having reliable measurements of the pressures induced by lateral spreads against large rigid foundations in small scale centrifuge tests has proven to be a very difficult task. The lack of reliable lateral pressure measurements against rigid elements hinders the possibility to develop guidelines to design such elements. In this research numerical models of free-field lateral spreading soils and lateral spreading-large rigid pile interaction have been calibrated and tested using centrifuge test measurements (displacements, accelerations and pore water pressures). The results of the numerical models have been used to determine the pressure distribution and bending moments induced by the lateral spreading soils against large-rigid pile foundations. The results are compared with current recommendations and simplified methods of analysis.

Chapter 3 presents the development and the calibration of three-dimensional numerical models using the displacement, acceleration, and pore water pressure time histories recorded in a free-field lateral spreading centrifuge test. The calibration process highlights the important role of small strain damping and the need for pressure-dependent dilation parameters to simultaneously provide the best match for measurements of pore water pressure, acceleration, and lateral displacement. The calibrated numerical model is then used to predict another free-field lateral spreading centrifuge test using the same soil profile but different input acceleration time history. The computed response shows good agreement with the centrifuge test measurements.

Chapter 4 presents the calculation of lateral pressures induced by lateral spreading soils against large piles using the results of three-dimensional numerical simulations. The numerical simulations are calibrated and evaluated using displacement, acceleration, and pore water pressure time histories recorded from lateral spreading centrifuge tests with a large, rigid deep foundation element located in the path of downslope soil movement. The calibration process highlights the important role of soil-pile interface modeling to simultaneously provide the best match for measurements of pore water pressure, acceleration, and lateral displacement. The numerical model is then employed to determine the effects of using representative permeability values and broadband input motions. Pressures extracted from these numerical analyses are used to determine pressure profiles and bending moments and are compared with current recommendations (i.e. strain wedge method and triangular net pressure distribution). The

computed response agrees well with the results of the strain wedge method for the upslope side of the pile and shows the need for adjusting the triangular pressure method to estimate the lateral loads and bending moment in the pile at different depths by introducing a depth-dependent coefficient

CHAPTER 2 - DAMPING FORMULATION FOR NON-LINEAR 1D SITE RESPONSE ANALYSES

2.1 Introduction

Numerous seismic events, such as the 1985 Michoacan earthquake, the 1989 Loma Prieta earthquake, the 1994 Northridge earthquake, the 1995 Kobe earthquake, and the 1999 Chi-Chi earthquake have demonstrated the relevance of local geologic and geomorphologic conditions on the seismic ground response. The changes in the intensity and the frequency content of the motion due to the propagation of the seismic waves in soil deposits and the presence of topographic features, commonly referred to as site effects, have a direct impact on the response of the structures during an earthquake event. One dimensional site response analysis methods are widely used to quantify the effect of soil deposits on propagated ground motion. These methods can be divided in two main categories: (1) frequency domain analyses [including the equivalent linear method, e.g. SHAKE (Schnabel et al., 1972)] and (2) time domain analyses (including nonlinear analyses).

Frequency domain methods are the most widely used to estimate site effects due to their simplicity, flexibility and low computational requirements. However, there are cases (i.e. high seismic intensities at rock base and/or high strain levels in the soil layers) in which an equivalent soil stiffness and damping for each layer cannot represent the behavior of the soil column over the entire duration of a seismic event. In these cases, a non-linear time domain solution is used to represent the variation of the shear modulus (G) and the damping ratio (ξ) during shaking.

In non-linear analysis, the following dynamic equation of motion is solved (Kramer, 1996b):

$$[M]\{\ddot{u}\}+[C]\{\dot{u}\}+[K]\{u\}=-[M]\{I\}\ddot{u}_g \tag{2-1}$$

where $[M]$ is the mass matrix, $[C]$ is the viscous damping matrix, $[K]$ is the stiffness matrix, $\{\ddot{u}\}$ is the vector of nodal relative acceleration, $\{\dot{u}\}$ is the vector of nodal relative velocities and $\{u\}$ is the vector of nodal relative displacements. $\{\ddot{u}_g\}$ is the acceleration at the

base of the soil column and $\{I\}$ is the unit vector. $[M]$, $[C]$and$[K]$matrices are assembled using the incremental response of the soil layers. The soil response is obtained from a constitutive model that describes the cyclic behavior of soil. The dynamic equilibrium equation, Eq. (2-1), is solved numerically at each time step using the (Newmark, 1959) β method.

The geologic column is discretized into individual layers using a multi-degree-of freedom lumped parameter model shown in Figure 2-1, or can alternatively be represented using finite elements (Kramer, 1996b). Each individual layer *i* is represented by a corresponding mass, non-linear spring, and a dashpot for viscous damping. Lumping half the mass of each of two consecutive layers at their common boundary forms the mass matrix. The stiffness matrix is updated at each time increment to incorporate non-linearity of the soil.

In the more widely used non-linear time domain site response analysis codes [e.g. DESRA (Lee and Finn, 1978), DMOD (Matasovic, 1993), and DEEPSOIL (Hashash, 2005)] a hyperbolic model is used to represent the backbone response of the soil and the extended unload-reload Masing rules (Masing, 1926) to model hysteretic behavior. The four extended Masing rules are commonly stated as:

(1) For initial loading, the stress–strain curve follows the backbone curve

$$\tau = F_{bb}(\gamma) \tag{2-2}$$

where τ is the shear stress $F_{bb}(\gamma)$ is the backbone curve function

(2) If a stress reversal occurs at a point $(\gamma_{rev}, \tau_{rev})$, the stress–strain curve follows a path given by:

$$\frac{\tau - \tau_{rev}}{2} = F_{bb}\left(\frac{\gamma - \gamma_{rev}}{2}\right) \tag{2-3}$$

(3) If the unloading or reloading curve intersects the backbone curve, it follows the backbone curve until the next stress reversal.

(4) If an unloading or reloading curve crosses an unloading or reloading curve from the previous cycle, the stress–strain curve follows that of the previous cycle.

The hysteretic damping calculated using the unload-reload stress-strain loops has the following two shortcomings:

(a) at very small strains the response is nearly linear (hysteretic damping is nearly zero) and the use of velocity proportional viscous damping is needed. Small strain damping controls the behavior of the soil mass under dynamic loads that induce small deformations (i.e. weak amplitudes of seismic motions). Frequency dependent Rayleigh damping (Park and Hashash, 2004c) is commonly employed which can result in over or under damping (Park and Hashash, 2004c; Kwok et al., 2007b)

(b) the hysteretic damping can result in overestimation of damping at large strains. Hysteretic damping controls the energy dissipation in problems which involve large strains.

Gerolymos and Gazetas (2005) developed a phenomenological constitutive model for the non-linear 1-D ground response analysis of layered sites. The proposed model, a special form of the Bouc-Wen viscoplastic model, is able to reproduce nonlinear hysteretic behavior for different types of soils and has the ability to generate simultaneously realistic modulus and damping curves. The model requires information on anisotropic behavior of the soil and shape of the unload-reload loop. This information is not available for most soils, thus it is difficult to quantify required model constants.

Pyke (1979) proposed an alternative hypothesis to the second Masing rule. The new hypothesis states that the scale of the stress-strain relationship for initial loading is a function of the stress level on reversal for unloading and reloading and not only the use of a factor of two.

The Duncan and Chang (1970) hyperbolic model using the Cundall-Pyke hypothesis (HDCP model) has been implemented in the software TESS. Using Cundall-Pyke instead of the

Masing rules does not always generate a better match with laboratory dynamic curves. Therefore, Pyke (2000) proposes that the hysteretic damping calculated in the soil model be divided by a factor of two to achieve a match to the laboratory measurements. To provide a good fit to both modulus reduction and damping curves based on laboratory tests the HDCP model implemented a shear modulus degradation scheme in which the modulus at a reversal point is not equal to G_0 but is a function of strain and number of cycles (Pyke, 2000). The main shortcomings of using the HDCP model with shear modulus degradation matching both modulus reduction and damping curves are: (1) the shear modulus degradation seems excessive and therefore not always representative of soil behavior and (2) the resulting damping curve in most of the cases is not a smooth function.

Muravskii (2005) presented a methodology to construct loading and reloading curves based on a general function that becomes an alternative to scaling the backbone by a factor of two; as is stated in the Masing rules. Three different functions [Davidenkov (1938), Puzrin and Burland (1996) and Muravskii (1998)] are used to construct the unloading and reloading curves. These unloading and reloading curves allow matching the theoretical results to experimental data, in particular the damping properties of the model. In a later section of this chapter a series of examples are presented to highlight the most important features of using the Muravskii (2005) method.

In this chapter two new formulations to model small strain and hysteretic damping are described. The small strain damping formulation relieves the problems associated with the use of Rayleigh damping. The hysteretic damping formulation modifies the extended Masing rules and results in a better match of damping curves. The effects of the proposed formulations are illustrated in a series of one-dimensional wave propagation analyses.

2.2 Small Strain Damping:

2.2.1 Current representation via Rayleigh damping

Most of the available time-domain wave propagation codes include small strain damping by implementing the original expression proposed by Rayleigh and Lindsay (1945b), in which, the damping matrix results from the addition of two matrices; one proportional to the mass matrix and the other proportional to the stiffness matrix.

$$[C] = a_0[M] + a_1[K] \tag{2-4}$$

where [M] is the mass matrix, [K] is the stiffness matrix and a_0 and a_1 are scalar values selected to obtain the given damping value for two control frequencies.

Small strain damping calculated using the Rayleigh and Lindsay (1945b) solution is frequency dependent (ξ changes depending on the frequency of the input motion), a result that contradicts most of the available experimental data which show that material damping in soils is frequency independent at very small strain levels within the seismic frequency band of 0.001 to 10 Hz (Lai and Rix, 1998a).

Park and Hashash (2004c) and Kwok et al. (2007b) explained the frequency dependency of the viscous damping matrix $[C]$. Hudson (1994) and Park and Hashash (2004c) described the application of the full Rayleigh formulation in site response analysis. For soil profiles with constant damping ratio, scalar values of a_0 and a_1 can be computed using two significant natural modes i and j using Equation (2-5):

$$\begin{bmatrix} \xi_i \\ \xi_j \end{bmatrix} = \frac{1}{4\pi} \begin{bmatrix} \frac{1}{f_i} & f_i \\ \frac{1}{f_j} & f_j \end{bmatrix} \tag{2-5}$$

where ξ_i and ξ_j are the damping ratios for the frequencies f_i and f_j of the system respectively. For site response analysis the natural frequency of the selected mode is commonly calculated as (Kramer, 1996b):

$$f_n = (2n-1)\frac{\overline{V}_s}{4H} \tag{2-6}$$

where n is the mode number and f_n is the natural frequency of the corresponding mode. It is common practice to choose frequencies that correspond to the first mode of the soil column and a higher mode that corresponds to the predominant frequency of the input motion. Kwok et al. (2007b) recommended a value equal to five times the natural frequency, Park and Hashash (2004c) also give a series of recommendations to determine these two frequencies. Equal values of modal damping ratios are specified for the two modes.

Wilson (2005) proposed to use only the stiffness proportional damping term to solve dynamic problems involving complex structural systems, in which a large number of high frequencies (short periods) are present. In this type of problem, periods smaller than the time step have a tendency to oscillate indefinitely after they are excited. Although the stiffness proportional damping with reference frequency equal to the sampling rate frequency provides numerical stability, its behavior resembles a high pass filter, which results in a highly frequency dependent viscous damping. Common values of sampling rate frequency (i.e. 50, 100 or 200 Hz) are higher than the upper limit of the frequency content range of almost all the seismic motions and the soil deposit natural frequencies, therefore one dimensional wave propagation problems will not exhibit the aforementioned numerical instability. It should be noted that viscous damping in the solution presented in this chapter included correct representation of soil behavior; consequently the objective solution should be frequency independent rather than highly frequency dependent as the solution proposed by Wilson (2005).

Equation (2-4) can be extended so that more than two frequencies/modes can be specified, and is referred to as extended Rayleigh formulation. [i.e. Park and Hashash (2004c) implemented an extended Rayleigh scheme using four modes in the software code DEEPSOIL (Hashash, 2005)]. Using the orthogonality conditions of the mass and stiffness matrices, the damping matrix can consist of any combination of mass and stiffness matrices (Clough and Penzien, 1993), as follows:

$$[C] = [M] \sum_{b=0}^{N-1} a_b \left([M]^{-1} [K] \right)^b \tag{2-7}$$

where N is the number of frequencies/modes incorporated. The coefficient a_b is a scalar value assuming a constant damping ratio throughout the profile and is defined as follows:

$$\xi_n = \frac{1}{4\pi f_n} \sum_{b=0}^{N-1} a_b \left(2\pi f_n \right)^{2b} \tag{2-8}$$

Equation (2-8) implies that the damping matrix can be extended to include any number of frequencies/modes. The resultant matrix from Equation (2-7) is numerically ill-conditioned since coefficients $f_n^{-1}, f_n^1, f_n^3, f_n^5 \ldots f_n^{2n-1}$ differ by orders of magnitude. Having more than four

frequencies/modes can result in a singular matrix depending on f_n and a_b cannot be calculated. An increase in the frequencies/modes used in the calculation of the damping matrix also generates an increase in the number of diagonal bands of the viscous damping matrix, and therefore a significant time increase for the solution of the wave propagation problem. Incorporating an odd number of modes is also problematic since it will result in negative damping at certain frequencies (Clough and Penzien, 1993). Figure 2-2 presents a comparison of the effective damping obtained using one mode, two modes and four modes solutions.

2.2.2 New formulation to construct the viscous damping matrix

Liu and Gorman (1995) extended Rayleigh damping in terms of series having terms depending on two different indices (double series). The proposed extensions provide solutions for both negative and rational indexed series. Using the rational indexed extension and an index b equal to 1/2 in Equation (2-7), Equations (2-7) and (2-8) reduce to Equations (2-9) and (2-10) respectively. The complete procedure to obtain Equation (2-9) from Equation (2-7) is presented in Appendix A.

$$[C]=[M]\sum_{b=0}^{N-1} a_b\left([M]^{-1}[K]\right)^b = [M]\sum_{b=0}^{N-1} a_b \Phi \omega^{2b} \Phi^{-1} = [M]\sum_{b=0}^{N-1} a_{1/2} \Phi \omega \Phi^{-1} \tag{2-9}$$

$$\xi_n = \frac{1}{4\pi\ f_n}\sum_{b=0}^{N-1} a_b \left(2\pi\ f_n\right)^{2b} = \frac{1}{4\pi\ f_n}\left[a_{1/2}\left(2\pi\ f_n\right)\right] = \frac{1}{2}a_{1/2} \tag{2-10}$$
$$\rightarrow a_{1/2} = 2\xi_n$$

where (ω) is the natural frequencies diagonal matrix and (Φ) is the real modal matrix of the system.

Equation (2-10) shows that for b=1/2 the viscous damping of the system is not dependent on the frequency. The numerical cost of this solution is in calculating the natural frequencies and the real modal matrix of the system, which requires the calculation of the eigenvalues and eigenvectors of the matrix $[M]^{-1}[K]$.

2.2.3 Implementation of small strain frequency independent damping in non-linear site response analyses

All the one dimensional wave propagation problems presented in this chapter have been solved using the site response program DEEPSOIL (Hashash, 2005). To implement the new frequency independent model, a QL/QR algorithm (Press et al., 1992) with implicit shifts has been included in DEEPSOIL. The QL/QR algorithm swiftly reduces the off diagonal terms of the $[M]^{-1}[K]$ matrix until they are negligible. The algorithm repeatedly applies a similarity transformation to the result of the previous transformation until the matrix converges to a diagonal form. Once $[M]^{-1}[K]$ matrix is in a diagonal form its eigenvalues could be easily calculated, then using the definition of eigenvector and the previously calculated eigenvalues each one of the eigenvectors is calculated and the construction of the Φ matrix is completed.

Appendix B presents a flow chart of the method implemented in DEEPSOIL to obtain the damping matrix using the frequency independent scheme. One concern with the frequency independent viscous damping is the effect of the natural frequencies induced by the shear modulus reduction of the soil profile as a function of the strain level. A set of analyses were developed in which the damping matrix was calculated for each time step. These analyses showed small incidence of the change in the natural frequencies in the deposit's response.

This result agrees with the results obtained by Park and Hashash (2004c). Updating the damping matrix is computationally expensive (more than 10 times in the example presented later) and appears to be unnecessary.

2.3 Hysteretic Damping

2.3.1 Extended Masing rule hysteretic damping in the Hyperbolic Model

The hyperbolic model is defined by using two sets of equations; Equation (2-11) defines the stress-strain relationship (backbone curve) for loading, Equation (2-12) defines the stress-strain relationship for unloading-reloading conditions.

$$\tau = \frac{\gamma \cdot G_0}{1 + \beta\left(\frac{\gamma}{\gamma_r}\right)^s} \tag{2-11}$$

$$\tau = \frac{2 \cdot G_0 \cdot \left(\frac{\gamma - \gamma_{rev}}{2} \right)}{1 + \beta \left(\frac{\gamma - \gamma_{rev}}{2 \cdot \gamma_r} \right)^s} + \tau_{rev} \tag{2-12}$$

whereby, γ: given shear strain, γ_r: reference shear strain, β: dimensionless factor G_0: maximum shear modulus, and, s: dimensionless exponent. (Park and Hashash, 2004a), in order to represent the dependence of modulus on confining pressure, propose the following expression for γ_r:

$$\gamma_r = a\left(\sigma' / \sigma_{ref}\right)^c \tag{2-13}$$

where, a and c are scalars which depend on the soil type and must be determined based on laboratory test results, σ' is the effective vertical stress and σ_{ref} is a reference stress.

It can be observed that Equation (2-12) is the result of applying the second Masing rule to the backbone equation of the hyperbolic model [Equation (2-11)].

Hysteretic damping ($\xi_{hysteretic}$) is proportional to the energy lost in each cycle of vibration and therefore is also proportional to the area of the hysteretic loop generated from Equation (2-12). Equation (2-14) shows the expression used to calculate $\xi_{hysteretic}$, in which $\xi_{hysteretic}$ is proportional to the ratio of the area enclosed by the hysteretic loop and the triangular area corresponding to the work developed by an equivalent linear material (See Figure 2-3).

$$\xi_{hysteretic} = \frac{A}{4\pi \cdot B} \tag{2-14}$$

where A and B correspond to area enclosed by the hysteretic loop and triangular area presented in Figure 2-3 respectively.

Even though the non-linear model implemented in site response analysis should match both G & ξ variations with cyclic shear strain, most of the available stress-strain relationships which use the extended Masing unloading-reloading rules (Masing, 1926; Kramer, 1996b) provide greater $\xi_{hysteretic}$ for medium to large strains compared to the damping values obtained in dynamic tests when the calibration of the constitutive model parameter is based only on the

modulus reduction curve (MR) (Seed et al., 1986; Darendeli, 2001; Kwok et al., 2007b) as illustrated in Figure 2-4.

This difference between $\xi_{hysteretic}$ measured in the laboratory tests and the values obtained using the stress-strain relationships based on Masing rules leads to an underestimation of shear strains and/or surface intensities at the ground surface. A solution for this mismatch could be achieved if the parameters of the soil constitutive model are calibrated using both curves (modulus reduction and damping curves) at the same time. However, for simple non-linear models such as the hyperbolic model, this approach introduces differences in stiffness of the modeled behavior compared with the target curves for low to medium strains.

Based on the modulus reduction and damping curves obtained in laboratory tests it is possible to determine the parameters of the modified hyperbolic model that provide the best fit to one or the two curves:

MR: Modulus reduction curve is very well matched to the target curves but the damping curve is not matched due to an inherent limitation in Masing load-unload criteria.

MRD: Balance the mismatch between the modulus reduction and damping curves.

MD: Damping curve is very well matched to the target curves but the modulus reduction curve is not matched due to an inherent limitation in Masing load-unload criteria.

Figure 2-5 presents a comparison of the different procedures to fit the modulus reduction and damping curves.

A solution has been proposed by Darendeli (2001) to provide a better match for both curves (modulus reduction and damping) simultaneously. Using nearly 200 dynamic test results, Darendeli (2001) developed an empirically based modified hyperbolic model to predict the linear and nonlinear dynamic responses of different soil types. The developed model is implemented as a reduction factor [Equations (2-15) and (2-16)] which effectively alters the Masing rules:

$$\xi_{hyteretic} = DF(\gamma_m) \cdot \xi_{Masing} \tag{2-15}$$

$$DF(\gamma_m) = b_1 \left(\frac{G_{\gamma_m}}{G_0} \right)^{c_1} \tag{2-16}$$

where $DF(\gamma_m)$ is Darendeli's reduction factor, ξ_{Masing} is the hysteretic damping calculated using the Masing rules based on the modulus reduction curve, G_{γ_m} is the secant modulus corresponding to the maximum shear strain level γ_m, b_1 is a variable which depends on the soil and input motion properties (plasticity, effective stress, number of cycles, mean frequency) and c_1 is a constant with a value of 0.1.

Darendeli's reduction factor [Equation (2-16)] reduces the hysteretic damping by 40% for small strains ($\gamma < 10^{-5}$) and by 70% for large strains ($\gamma > 10^{-2}$), obtaining damping values close to the ones measured in laboratory tests. However, using this reduction factor results in a decrease of the damping for strains greater than 10^{-2} which is inconsistent with the curves obtained from laboratory tests.

2.3.2 New hysteretic damping formulation

A new expression for a damping reduction factor $F(\gamma_m)$ is introduced, this expression modifies the Masing unloading-reloading rules and provides a better agreement with the damping curves for larger shear strains, but preserves the simplicity of the solution proposed by Darendeli (2001). Equation (2-17) presents the selected functional form for the damping reduction factor:

$$F(\gamma_m) = p_1 - p_2 \left(1 - \frac{G_{\gamma_m}}{G_0} \right)^{p_3} \tag{2-17}$$

in which, p_1, p_2 and p_3 are non-dimensional parameters selected to obtain the best possible fit with the target damping curve.

The proposed functional form for $F(\gamma_m)$ was obtained by a trial and error procedure in which different types of expressions were tested to fit 50 modulus reduction and damping curves (Appendix C). Figure 2-6 illustrates the performance of the proposed functional form using four

of the fifty dynamic curves. Figure 2-6 is constructed using a four step process: (1) calculate the hysteretic damping (ξ_{Masing}) by using the modulus reduction curves and the extended Masing rules, (2) determine the target damping reduction ratio at a given strain as the ratio between the hysteretic damping measured in laboratory tests $\xi_{Laboratory}$ and ξ_{Masing}, (3) find variables p_1, p_2 and p_3 that generate the best fit to the $\xi_{Laboratory}/\xi_{Masing}$ and (4) plot the $\xi_{Masing}/\xi_{Laboratory}$ ratio versus strain. Figure 2-6 also includes the corresponding goodness of fit R^2 of Equation (2-17) using the p_1, p_2 and p_3 coefficients which are consistently high. In all the 4 curves studied, the proposed functional form is able to closely reproduce the relationship between $\xi_{Masing}/\xi_{Laboratory}$ and strain, which results in a very good fit for the corresponding damping curve.

Appendix C presents the results of the aforementioned procedure applied to the complete set of 50 selected curves. The R^2 coefficients obtained for both modulus reduction [using the hyperbolic backbone curve expression shown in Equation (2-11)] and damping curve [using the proposed damping reduction factor shown in Equation (2-17)]. The agreement is very good to excellent for all 50 sets of curves.

The modulus reduction and damping curves fitting procedures using the reduction factor (MRDF) consist of the following three steps and is implemented in DEEPSOIL:

1. Determine the best backbone curve parameters of the modified hyperbolic model to fit the modulus reduction curve
2. Calculate the corresponding damping curve using the back-bone curve (determined in the previous step) and Masing rules.
3. Estimate the reduction factor parameters (p_1, p_2 and p_3) that provide the best fit for the damping curve.

Figure 2-7 compares the damping curves obtained using the new proposed reduction factor (MRDF procedure) with MRD and MR fitting procedures whereby Darendeli's curves for sand are used as target curves. The MRDF approach provides an excellent match for the target curves. The MRDF approach does not result in a reduction in damping which is a limitation of the Darandeli reduction factor.

Figure 2-8 compares the damping curves obtained using the new proposed reduction factor (MRDF procedure) with MRD and MR fitting procedures using as target the curves proposed by Yamada et al. (2008) for clays. The new factor provides a good fit for both modulus reduction and damping curves, even for strains greater than 1%.

As discussed earlier, Muravskii (2005) proposed another procedure using three different functions [Davidenkov (1938), Puzrin and Burland (1996) and Muravskii (1998)] to modify the extended Masing rules and regulate the dependence of the damping ratio on the strain amplitude in the process of cyclic deformation of a material. Two sets of examples compare the results of the three different functions presented by Muravskii (2005). Figure 2-9 presents the comparison using as target the curves proposed by Yamada et al. (2008) for clays. Figure 2-10 presents the comparison using as a target the curves for solid waste 8 – 25% < 20 mm (Zekkos et al., 2006). The methodology proposed by Muravskii (2005) (specifically where Muravskii and Frydman (1998) function is used to construct the loading and reloading curves) generates a better fit for modulus reduction and damping curves than the use of the MR procedure. MRDF fitting procedure matches all the points of the damping curve and not only the maximum damping value as the Muravskii (2005) procedure. The use of all the points in the curve results in a better fit for both dynamics curves (as observed in Figure 2-10).

2.4 Implementation of the proposed model in non-linear site response analysis

The proposed model is implemented in the 1-D non-linear site response analysis (DEEPSOIL) by including the reduction factor to modify the unloading-reloading equations. The stress-strain model implemented in DEEPSOIL (Hashash, 2005) is an extension of the model developed by Duncan and Chang (1970) that has been used extensively in soil-structure interaction analyses of geotechnical structures (referred to in this study as extended modified hyperbolic model). Equations (2-18) and (2-19) are used to represent the loading and the unloading or reloading conditions respectively to calculate the shear stress corresponding to a given shear strain.

$$\tau = \frac{G_0 \cdot \gamma}{1 + \beta \cdot \left(\frac{\gamma}{\gamma_r} \right)^s} \tag{2-18}$$

$$\tau = F(\gamma_m) \cdot \left[\frac{2 \cdot G_0 \cdot \left(\frac{\gamma - \gamma_{rev}}{2} \right)}{1 + \beta \left(\frac{\gamma - \gamma_{rev}}{2 \cdot \gamma_r} \right)^s} - \frac{G_0 \cdot (\gamma - \gamma_{rev})}{1 + \beta \left(\frac{\gamma_m}{\gamma_r} \right)^s} \right] + \frac{G_0 \cdot (\gamma - \gamma_{rev})}{1 + \beta \left(\frac{\gamma_m}{\gamma_r} \right)^s} + \tau_{rev} \tag{2-19}$$

whereby, γ: given shear strain, γ_r: reference shear strain, β: dimensionless factor, s: dimensionless exponent, γ_{rev}: reversal shear strain, τ_{rev}: reversal shear stress, γ_m: maximum shear strain, $F(\gamma_m)$: reduction factor and G_0: initial shear modulus.

The main effect of having the damping reduction factor lower than one in Equation (2-19) is that the hysteretic paths do not follow the Masing rules. When the reduction factor decreases, the tangent shear modulus gets closer to the secant shear modulus corresponding to the maximum shear strain γ_m, and resulting in a decrease in the hysteric damping compared with the same result obtained if the model follows the Masing rules. If the reduction factor reaches a value of zero, the tangent shear modulus becomes equal to the secant shear modulus. Even though the model does not follow the second Masing rule, it follows the other three rules stated in the introduction of this chapter.

Seismic loading involves non-symmetrical unloading-reloading cycles and there is a need to properly define γ_m. γ_m can be defined either as the maximum shear strain or the maximum reversal strain. A series of one-dimensional wave propagation analyses were developed to select which option provides a more adequate response. Figure 2-11 presents a sketch of the stress-strain behavior computed for the case of non-symmetrical loading using the aforementioned γ_m definitions. The results show that when γ_m is defined as the maximum reversal shear strain, high levels of permanent plastic strain are observed; these high values of permanent plastic strain are inconsistent with field observations, therefore the option of defining γ_m as the maximum shear strain at any time was selected.

2.5 1D site response analysis using the proposed damping models

2.5.1 Linear site response with frequency independent viscous damping

A set of four linear site response analyses with constant damping (ξ = 5%) are presented to examine the influence of the proposed frequency independent viscous damping. Simi Valley Knolls School (Figure 2-12a), Treasure Island (Figure 2-12b), Anchorage (Figure 2-12c) and 1000 m soil column in the Mississippi Embayment (Figure 2-12d) profiles are analyzed to represent shallow stiff, soft clay medium depth, medium stiff glacial and deep sites respectively. The input motion in these analyses corresponds to the 1971 San Fernando earthquake motion (Figure 2-13) recorded at Pasadena Seismo Laboratory station [obtained from PEER (2000)] with a_{max} = 0.2 g. For highly non-linear analyses the Gilroy Array record [obtained from PEER (2000)] of the Loma Prieta is used (Figure 2-14); this motion has a PGA value of 0.60g.

Figure 2-15 presents a comparison of the 5% damped elastic response spectra obtained for each one of the four selected profiles using (1) frequency domain analysis, (2) time domain analysis using two modes Rayleigh damping and (3) time domain analysis using the new small strain damping model. All the analyses presented in this section are linear (no modulus reduction and constant damping during the entire time history) to establish a clear comparison between the results. The frequency domain analyses use a frequency independent damping complex shear modulus scheme (Hashash, 2005) and provide the correct solution. For stiffer soil column (Figure 2-15a) the difference between the two time domain analyses is very small. The two time domain solutions are very similar to the frequency domain solution. For medium soft clay and medium stiff glacial soil profiles (Figure 2-15 b and Figure 2-15c) an increase in spectral acceleration values between 0.1 and 0.3 seconds of period is obtained for the time domain analysis using Rayleigh damping. The overestimation of the seismic response results from lower damping values for those frequencies between the two target frequencies (see Figure 2-2). The proposed damping formulation time domain solution provides results that are very similar to those from the frequency domain solutions. For the deep, long period deposits the spectra (Figure 2-15d) obtained using the new approach is closer to the correct response (frequency domain solution) compared to the one obtained using the two modes Rayleigh damping. The observed difference of the time domain solutions for the 1000 m depth Mississippi Embayment column is a result of the important contribution of modes different from the ones selected for the Rayleigh

damping two modes solution in the deposit's dynamic response. Therefore, the over-estimation and underestimation of damping for these modes, in the two modes Rayleigh scheme, generates a decrease and an increase for those frequencies respectively.

The Anchorage soil profile (Figure 2-12c) is used to determine the effectiveness of the model when the damping through the soil profile is not constant (with small strain damping decreasing with the increase of effective stress) as presented in Figure 2-16a.

Figure 2-16b presents the response spectra comparison whereby good agreement between the frequency independent time domain solution and the frequency domain solution. Although it has been demonstrated that the model is able to capture the damping independent of the frequency, it should be noted that there are still some differences between frequency domain and time domain propagation analyses caused by the frequency cut-off (highest frequency that a layer can propagate; greater than 50 Hz in all the examples presented in this chapter) in the time domain analyses and the issues related with the number of points of the input motion in the frequency domain analyses (i.e. if the number of points cannot be expressed as 2^x the solution requires addition of zeros to the motion changing the minimum frequency in the input motion). An important advantage of the proposed model is that it is no longer necessary to estimate the modes needed in Rayleigh damping formulation.

2.5.2 Nonlinear site response with two modes Rayleigh viscous damping

A set of nonlinear site response analyses, using the Anchorage profile (Figure 2-12c), are presented to evaluate the influence of the proposed hysteretic damping reduction factor [MRDF, Equation (2-17)]. The commonly used two modes Rayleigh damping is employed to separately examine the effect of the new hysteretic damping formulation. Figure 2-17 shows the modulus reduction and damping curves used in the analyses.

The analysis results are presented in Figure 2-18 and include results using equivalent linear (EL, frequency domain), MR, MRD and the proposed MRDF time domain approaches. The EL results do not represent the correct solution in the current set of analyses. In general MR and MRD analyses give a surface response that is lower than the equivalent linear approach in the short and longer period ranges but similar results in the mid-period (0.1 to 0.4 seconds) range. The MRDF analysis provides a response that is significantly higher than both MR and

MRD analyses. The MRDF spectrum is slightly lower than the equivalent linear spectrum in the short and long period ranges but higher in the mid-period (0.1 to 0.4 seconds) range. Interestingly, the maximum shear strains profiles for all analyses are similar, except between 30 to 40 m, depths at which the maximum shear strains are higher for the MRDF analysis.

The result can be explained by the fact that in the MR analysis damping is overestimated, which results in attenuation of the spectral accelerations and strains. In the case of the MRD analysis the mismatch in the stiffness and the overestimation of the damping generates the observed decrease of the spectral accelerations for periods lower than 0.60 sec and a reduction of the maximum shear strains for the upper 40 m of the soil profile.

2.5.3 Nonlinear site response with frequency independent viscous damping

To test the complete damping scheme (frequency independent viscous damping and new hysteretic damping formulation) a series of analyses using the Anchorage profile (Figure 2-12c) and the San Fernando earthquake as input motion (Figure 2-13) were developed. EL, MR, MR+D (Modulus Reduction Fit with frequency independent viscous damping), MRDF and MRDF+D (complete model) analyses were developed. The computed maximum shear strain profile and response spectra obtained are presented in Figure 2-19.

MRDF+D analysis provides similar results to EL analysis in terms of PGA values and spectral accelerations. It should be noted that although MR, MR+D, MRDF and MRDF+D procedures are non-linear time domain analyses the results provided in this particular example differ greatly. Both maximum shears strain in the profile and spectral acceleration are greater in the MRDF+D analysis compared with the obtained values for the MR and MR+D analyses. This demonstrates that if the range of shear strains is small to medium the increase of the damping values (viscous and hysteretic damping) in the MR and MR+D models generate attenuation throughout the profile and a reduction of the maximum accelerations within the soil column. For non-linear analysis the use of the frequency independent small strain damping generates an increase in the peak ground acceleration and high frequency spectral accelerations. This result could be observed for both MR and MRDF procedures, Figure 2-19, when compared with the MR+D and MRDF+D results respectively.

The last example presented in this chapter corresponds to the use of the two new damping formulations simultaneously for a strong input motion; using as an input motion the Gilroy record of the Loma Prieta earthquake (Figure 2-14) and the Anchorage profile (Figure 2-12c). EL, MR and MRDF+D analyses were developed. The computed maximum shear strain profile and response spectra obtained are presented in Figure 2-20. Although the use of MRDF+D method results in a lower PGA value than the one obtained in the EL analysis, the spectral accelerations corresponding to periods between 0.03 to 0.3 sec (correspondent to most of the 1, 2 and 3 stories buildings constructed in the country) are higher when the MRDF+D model is used. The use of the MR model results in lower spectral acceleration values; a result that could be explained by the overestimation of the hysteretic damping in this model. The strain profiles are very similar for the two non-linear time domain analyses, however the maximum strain for the upper 20 m of the profile are higher when the MRDF+D model is used.

2.6 Tables and Figures

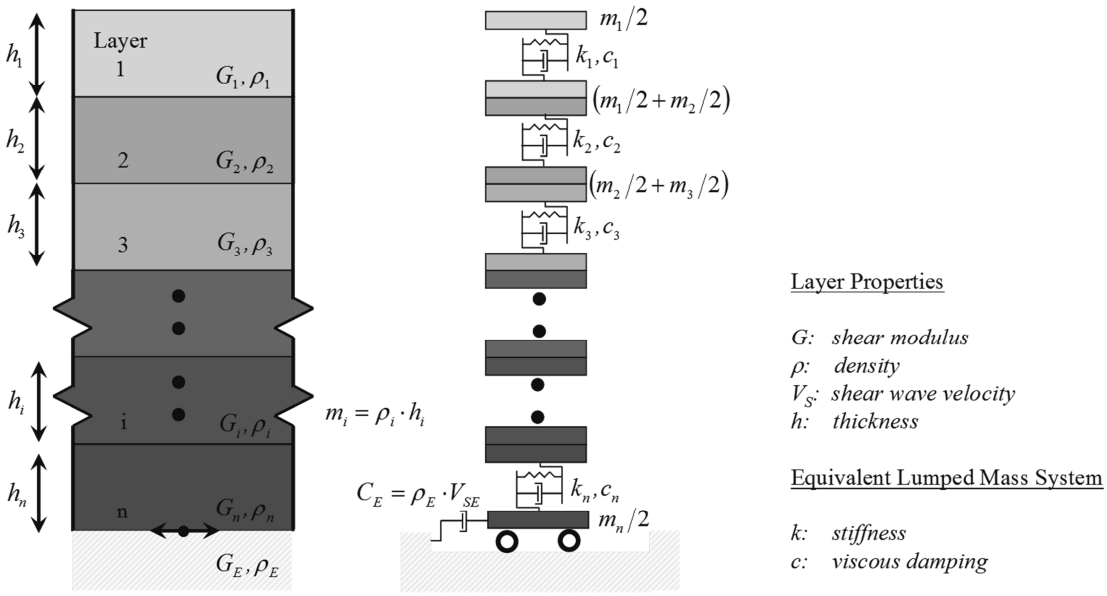

Figure 2-1: Multi-degree-of freedom lumped parameter model representation of horizontally layered soil deposit shaken at the base by a vertically propagating horizontal shear wave.

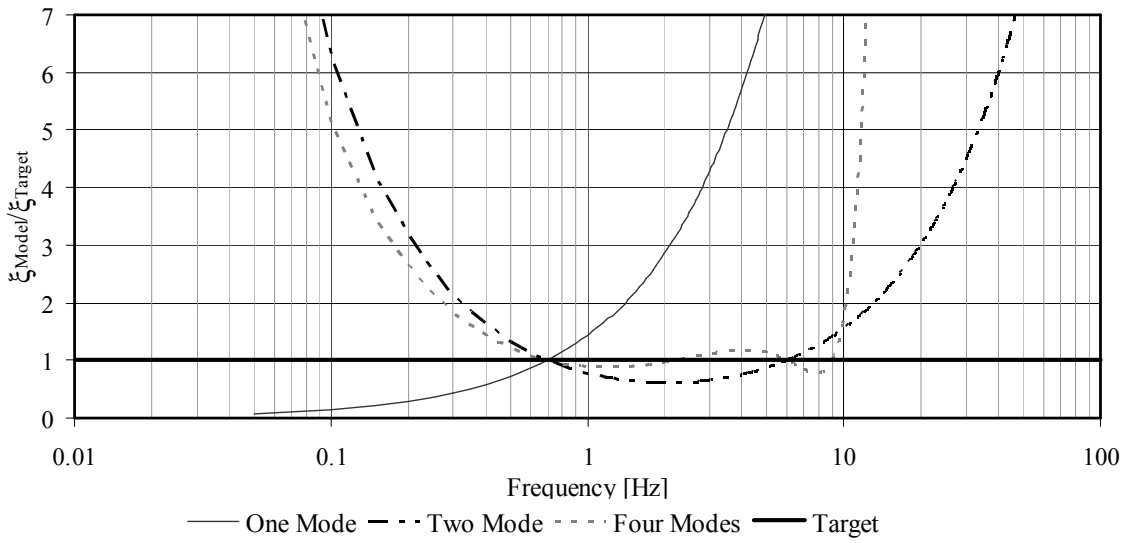

Figure 2-2: Effective damping for one, two and four (extended) modes Rayleigh formulation.

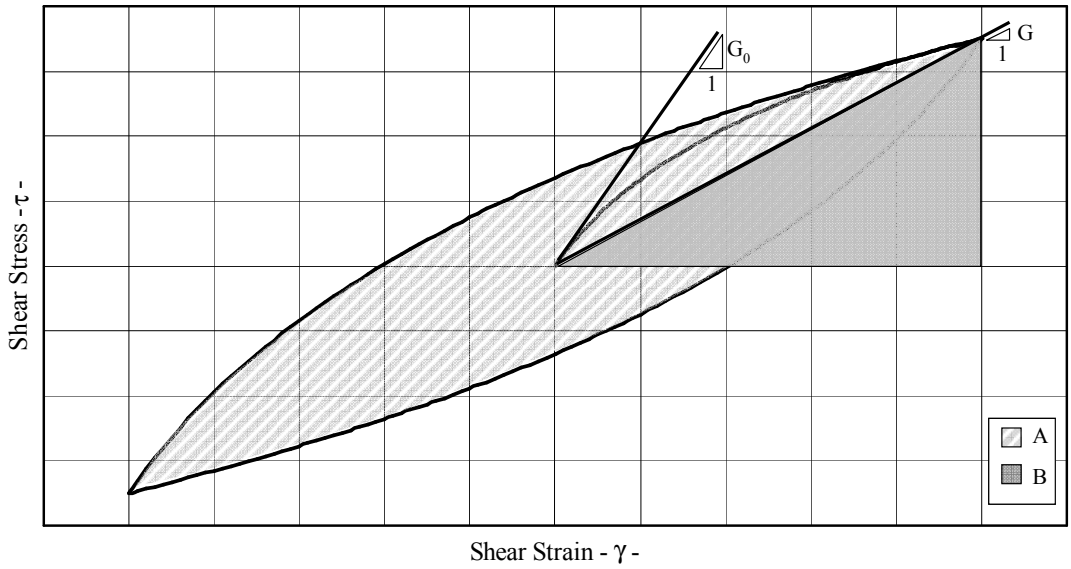

Figure 2-3: Stress-strain relationship.

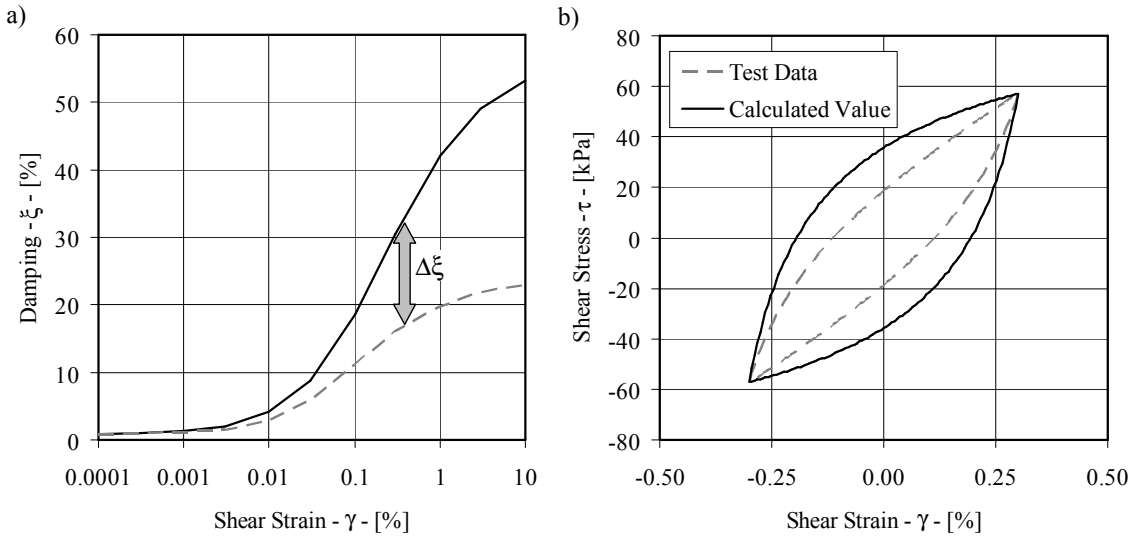

Figure 2-4: Overestimation of hysteretic damping using Masing rules. a) Damping curve. b) Hysteretic loop.

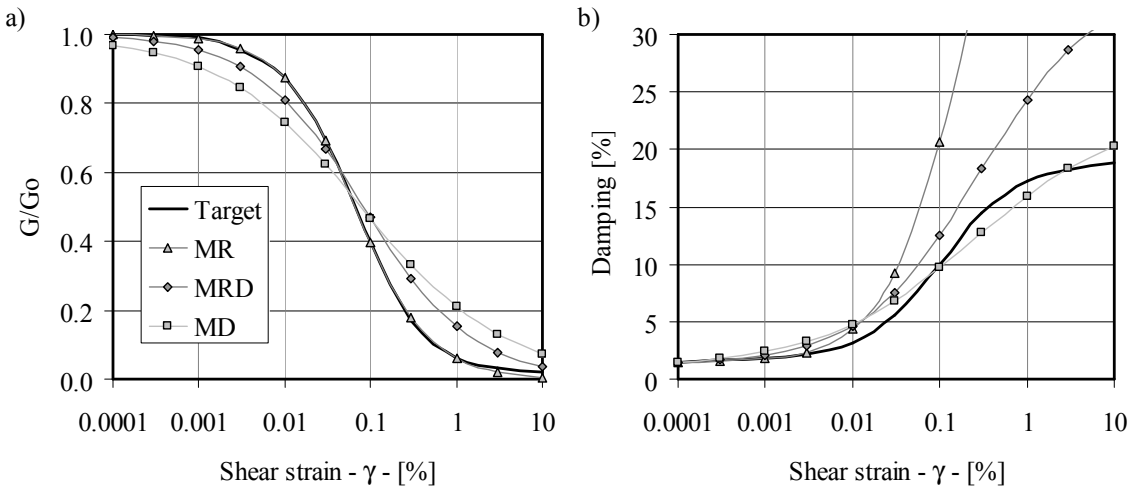

Figure 2-5: Hyperbolic model fitting procedure for sands (reference curve for clays from Yamada et al (Yamada et al., 2008)) a) modulus reduction and b) damping curve.

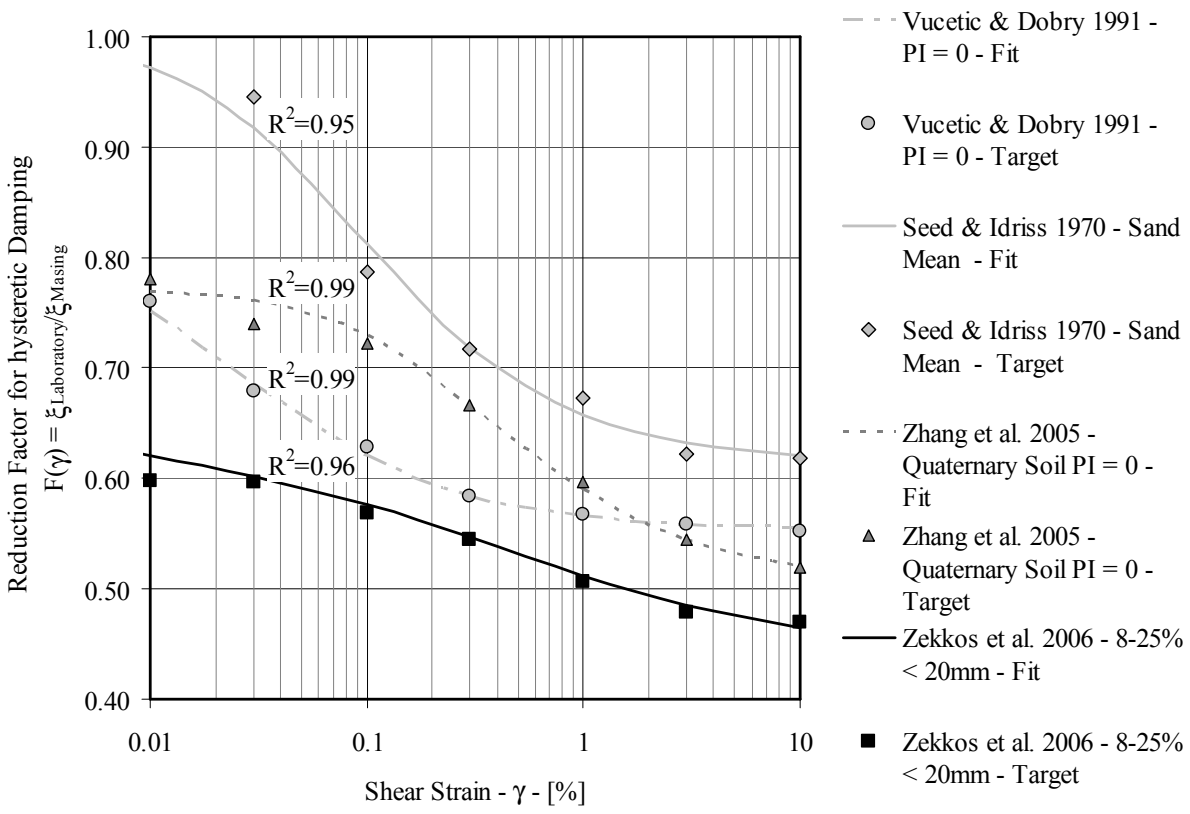

Figure 2-6: Reduction factor as a function of the shear strain.

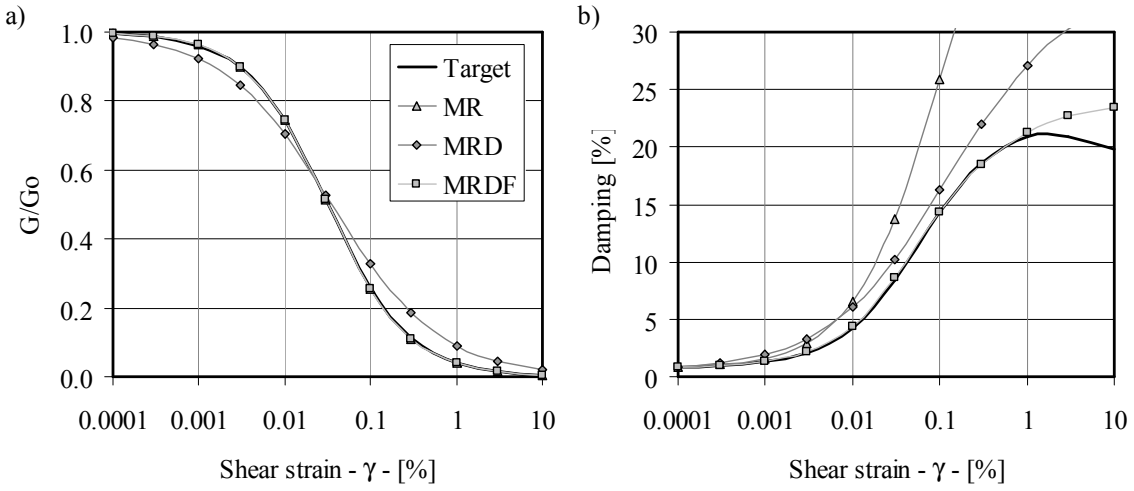

Figure 2-7 Evaluation of proposed damping reduction factor a) Modulus reduction and b) using Damping curve using Darendeli's (Darendeli, 2001) sand curves as target.

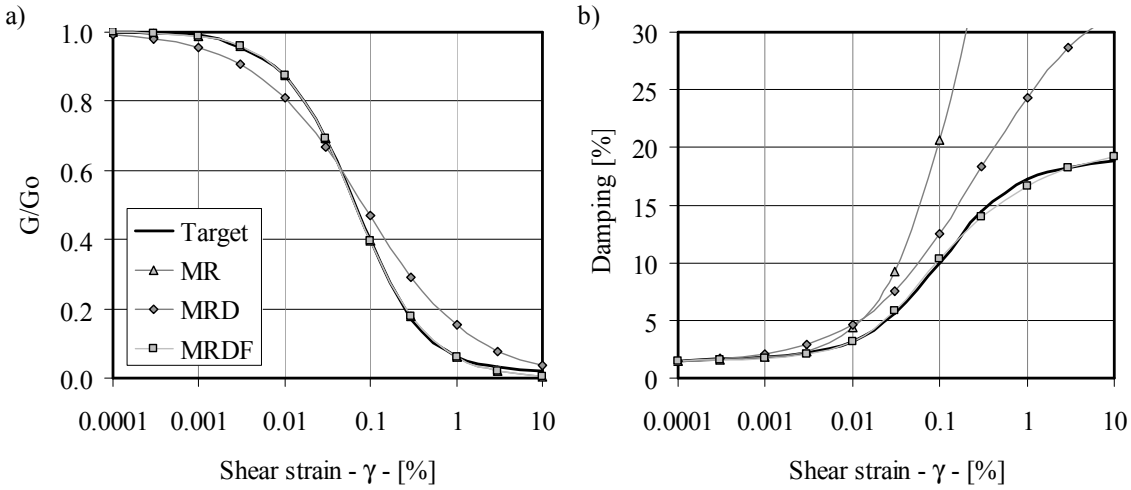

Figure 2-8: Evaluation of proposed damping reduction factor a) modulus reduction and b) damping curve using clays curves proposed by Yamada et al. (Yamada et al., 2008).

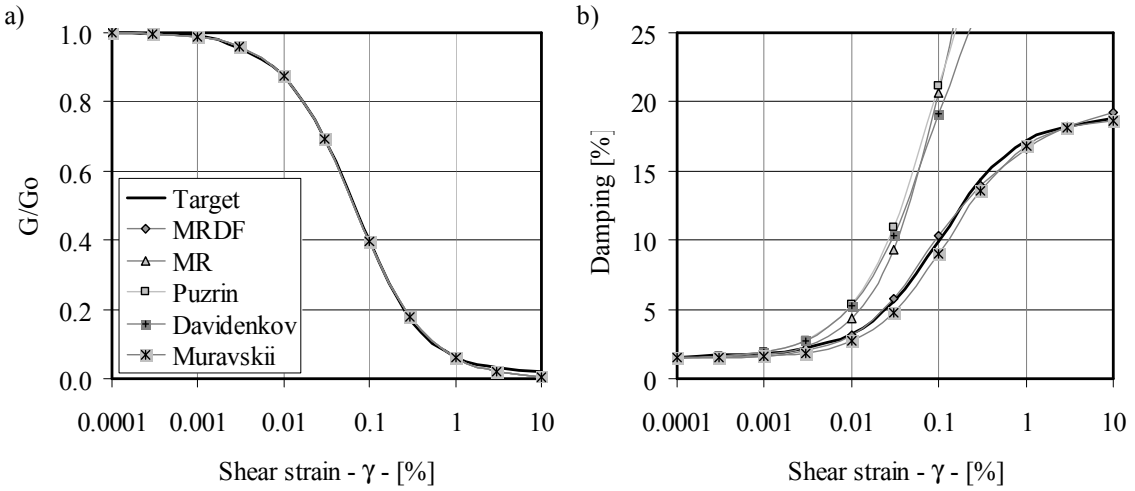

Figure 2-9: Evaluation of model fitting procedures for clays Yamada et al. (Yamada et al., 2008) a) modulus reduction and b) damping curve.

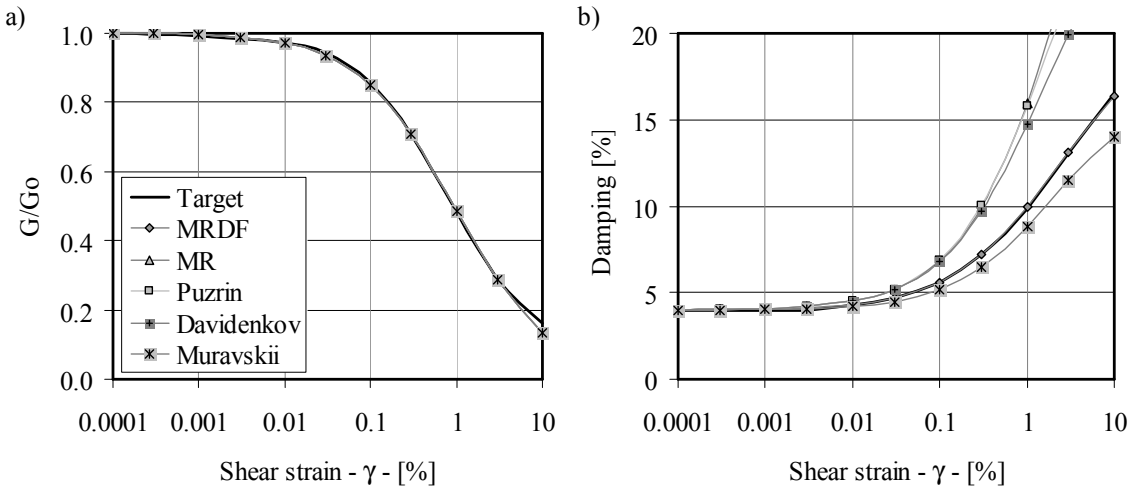

Figure 2-10: Evaluation of model fitting procedures for solid waste 8 – 25% < 20 mm (Zekkos et al., 2006) a) modulus reduction and b) damping curve.

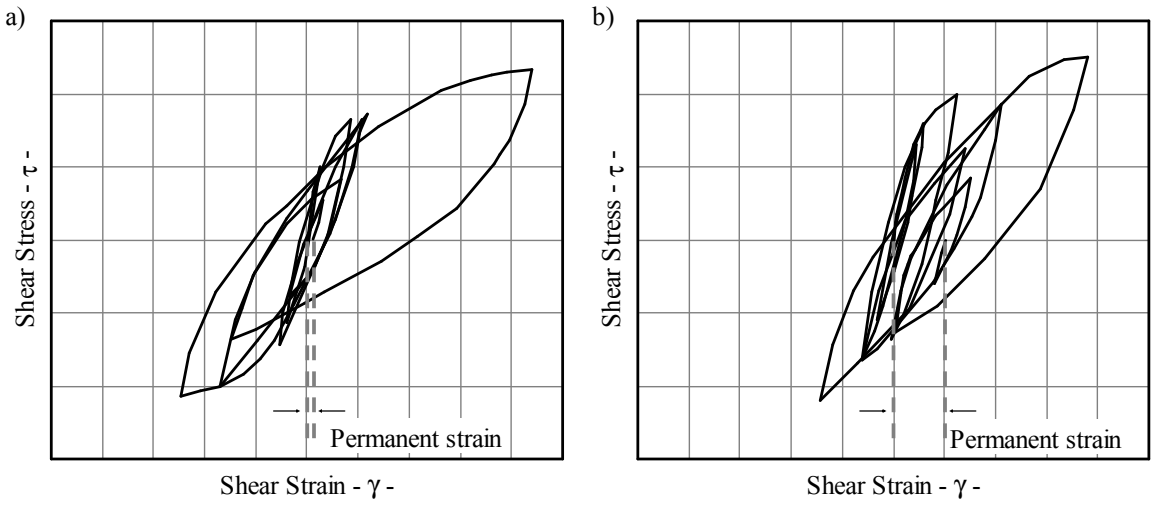

Figure 2-11: Computed stress-strain behavior for: a) γ_m defined as maximum shear strain, b) γ_m defined as maximum reversal shear strain.

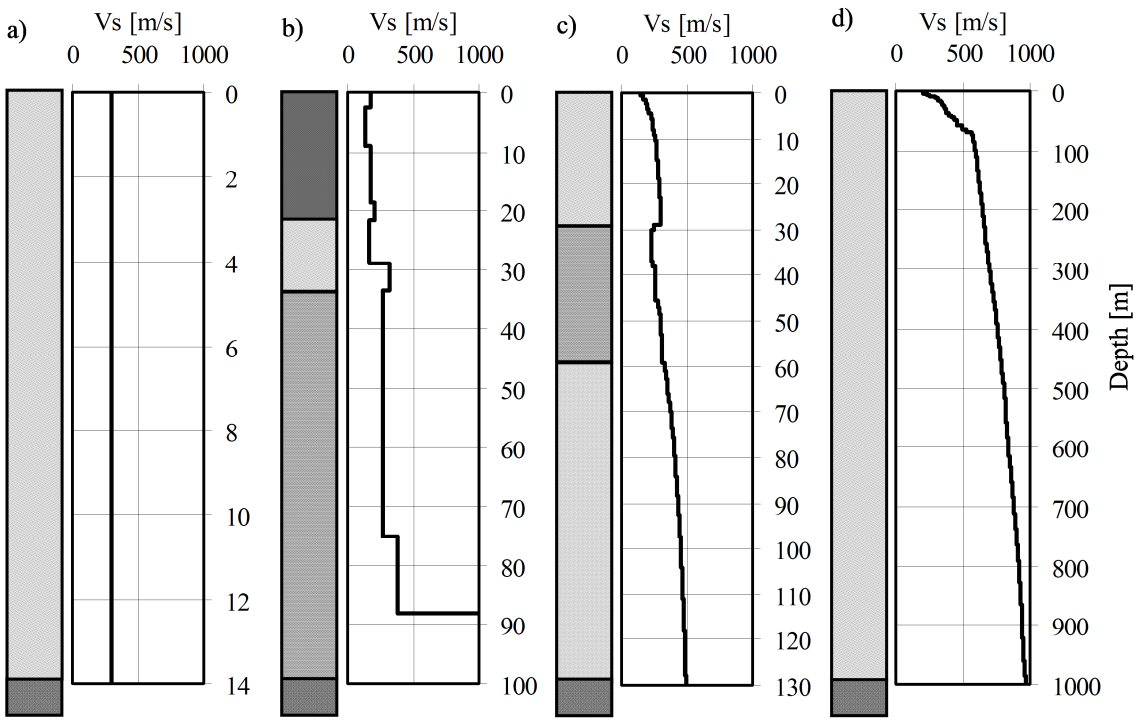

Figure 2-12: Soil columns. a) Simi Valley Knolls School, b) Treasure Island, c) Anchorage, d) Mississippi Embayment.

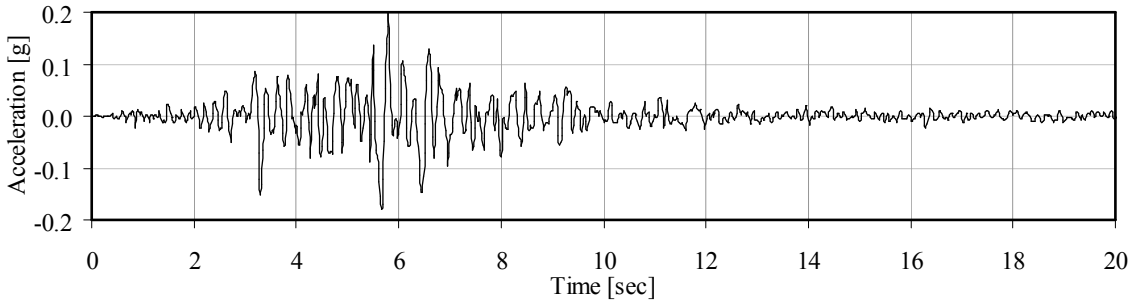

Figure 2-13 San Fernando Record (PEER, 2000).

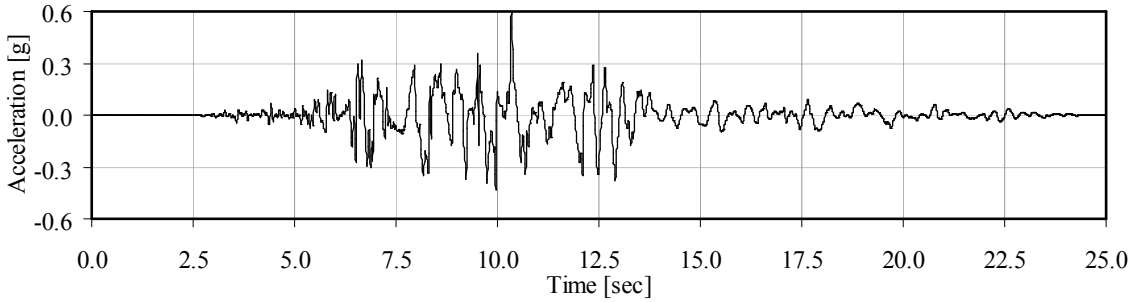

Figure 2-14: Loma Prieta Record (PEER, 2000).

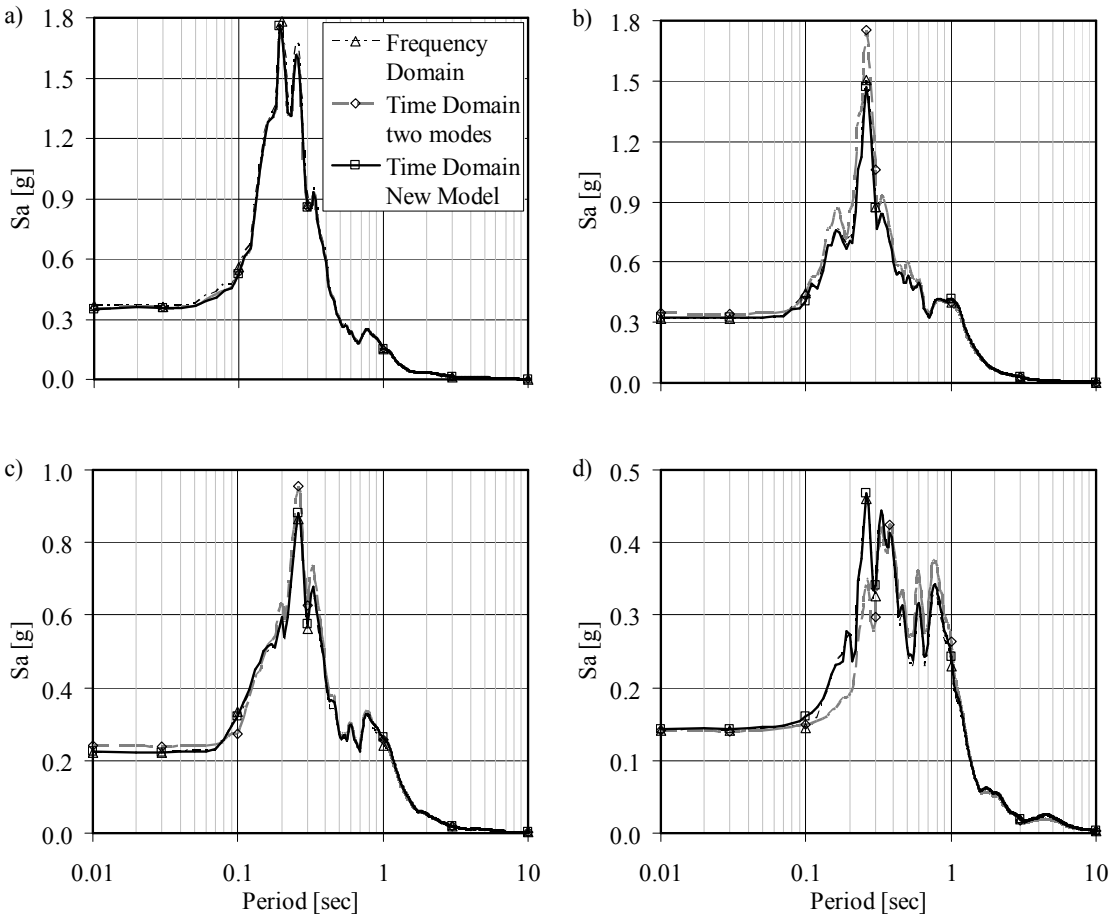

Figure 2-15: Surface response spectra comparison with constant damping ξ= 5% profile and linear site response analysis a) Simi Valley Knolls School, b) Treasure Island, c) Anchorage, d) Mississippi Embayment.

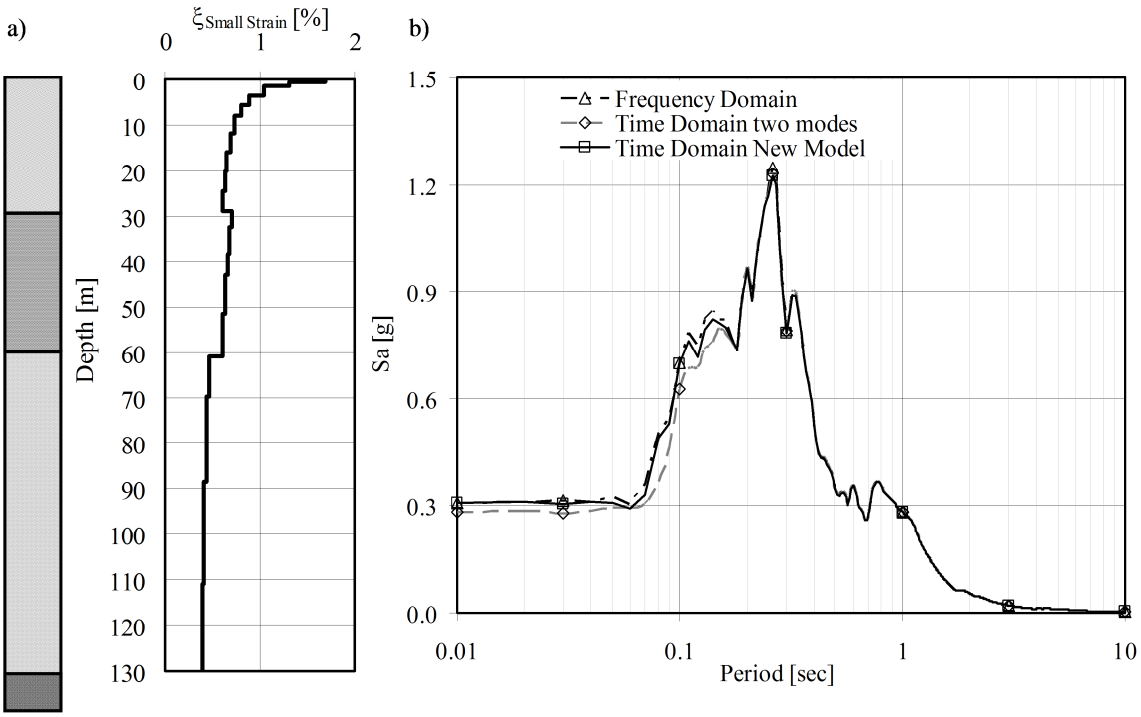

Figure 2-16: Anchorage profile linear site response analysis with variable damping a) small strain damping profile Anchorage soil column. b) surface response spectra comparison.

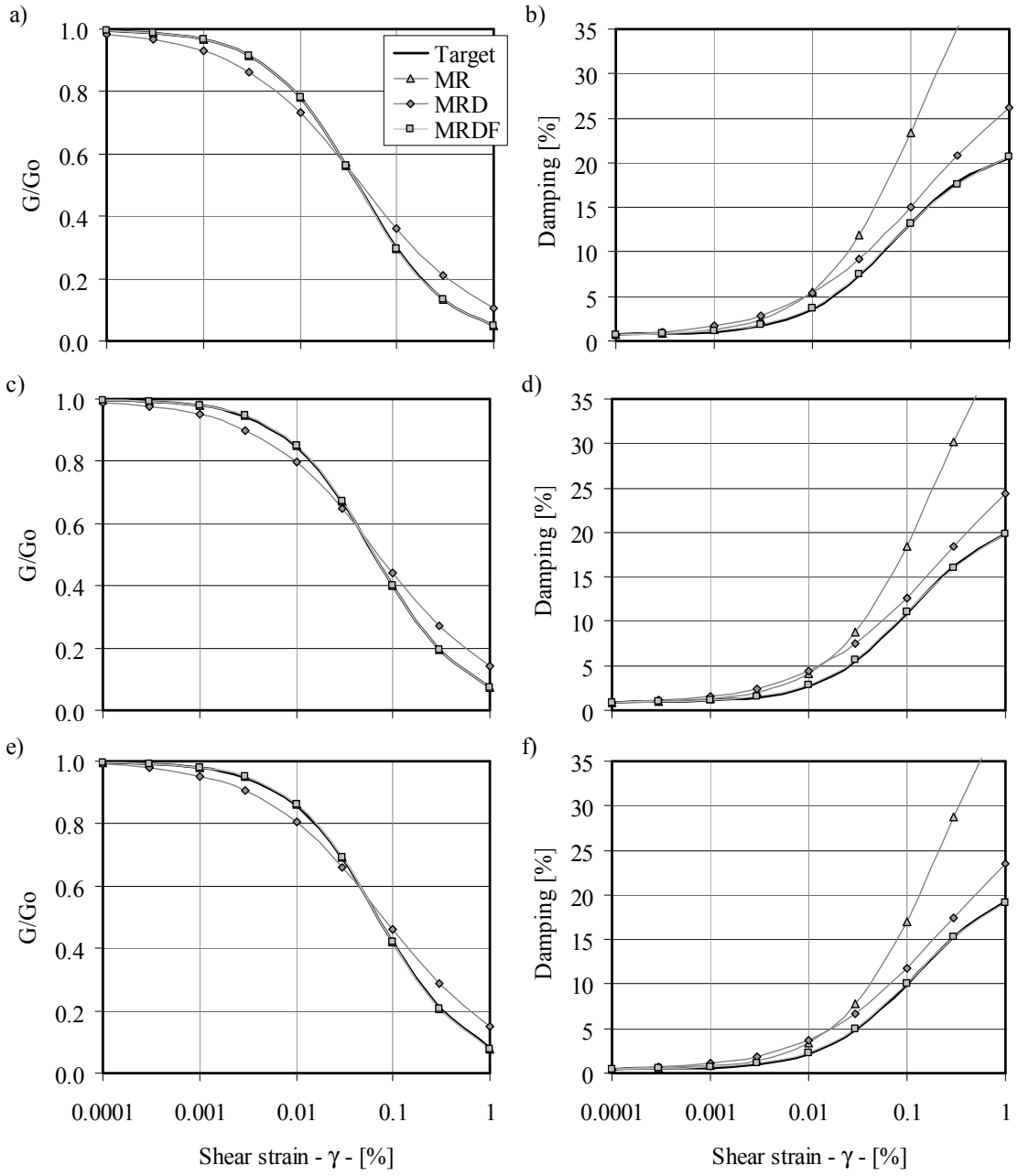

Figure 2-17: Dynamic soil properties of Anchorage profile a) Modulus reduction and damping curves. a) and b) Middle point of Fill layer. c) and d) Middle point of BCF layer. e) and f) Middle point of Glaciofluvial layer.

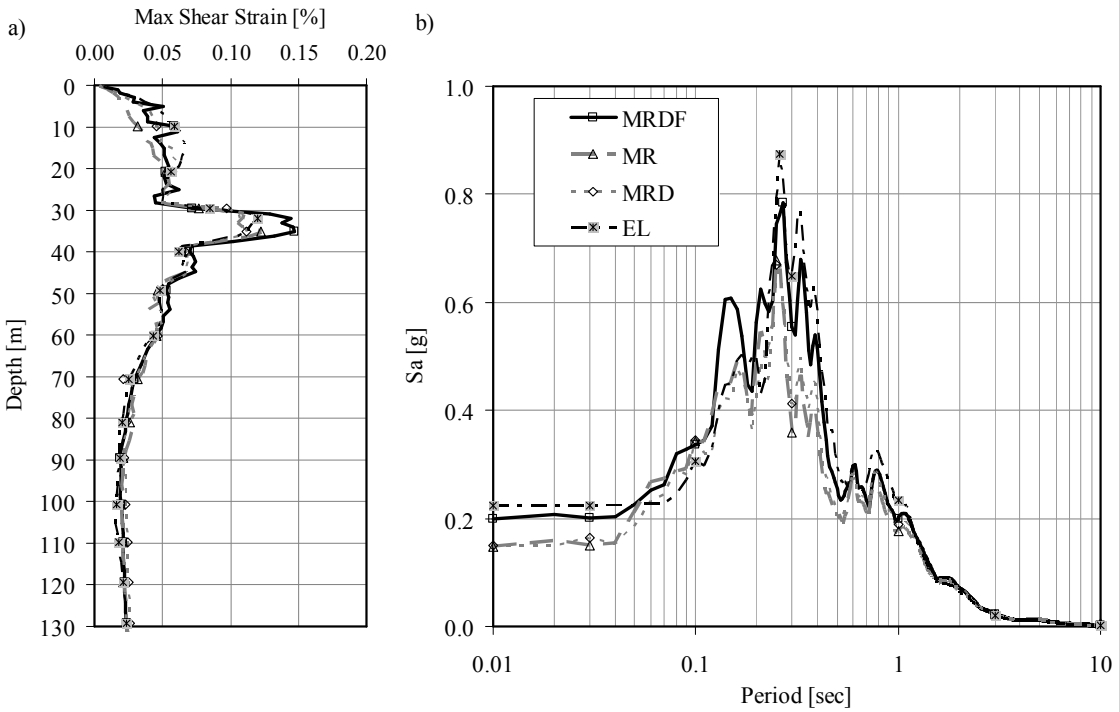

Figure 2-18: Anchorage profile nonlinear site response analysis with two-mode Rayleigh viscous damping a) maximum shear strain profile and b) surface response spectra comparison.

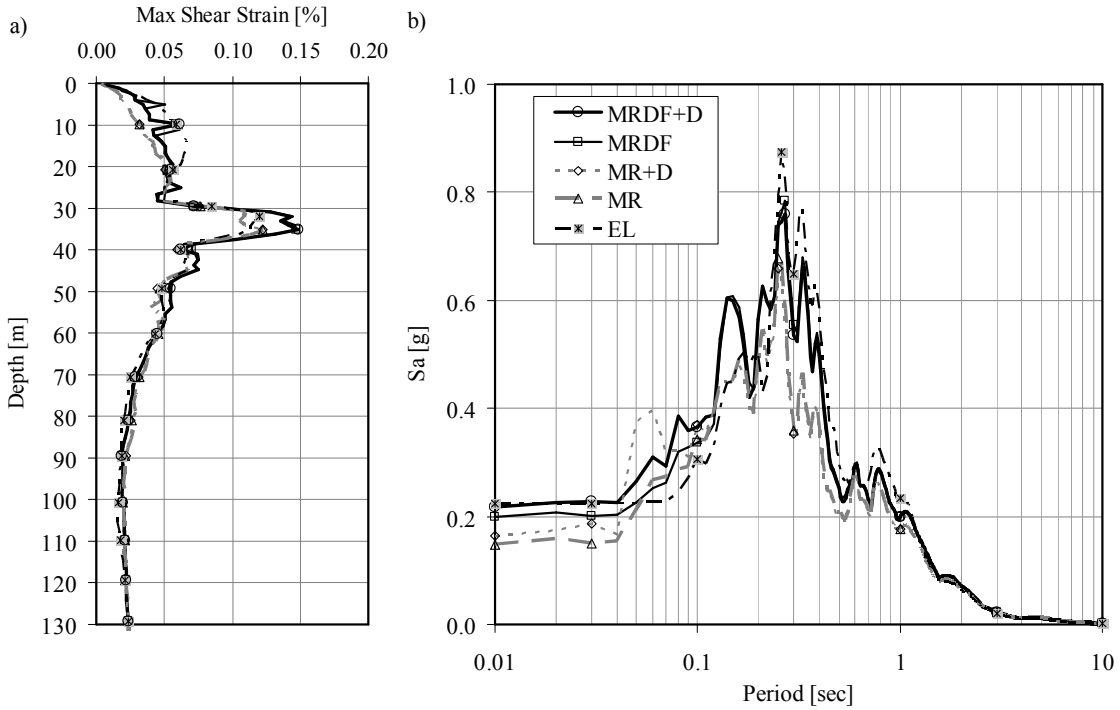

Figure 2-19: Anchorage profile nonlinear site response analysis with frequency independent viscous damping; San Fernando earthquake a) maximum shear strain profile and b) surface response spectra comparisons.

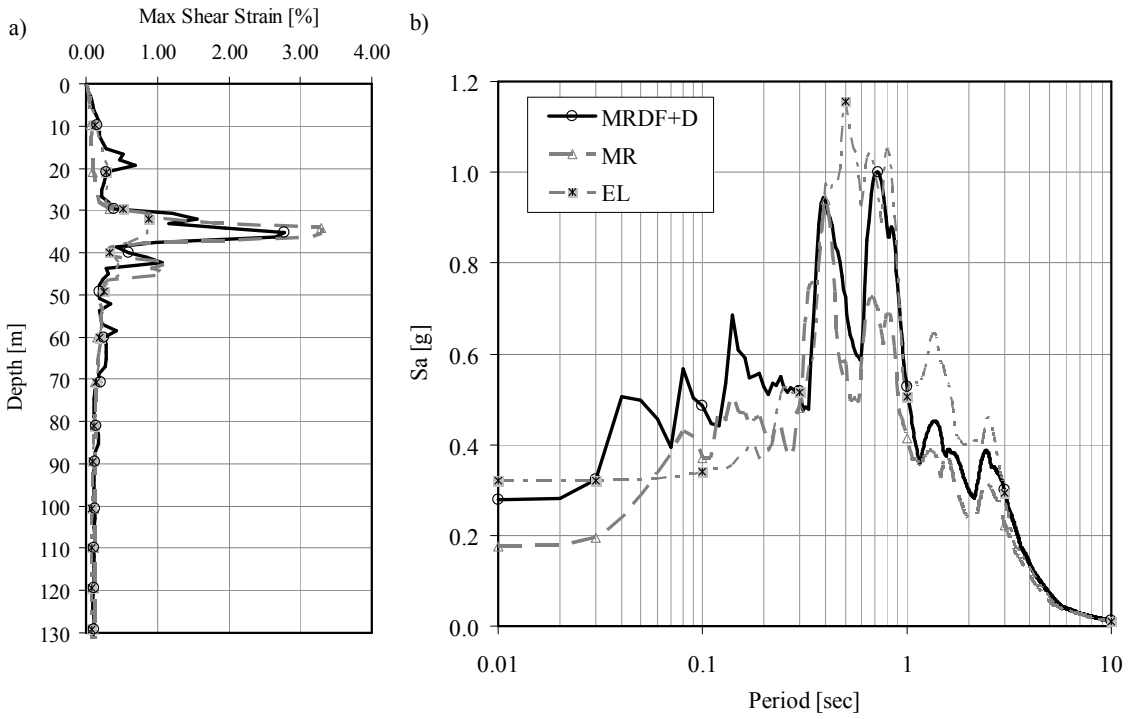

Figure 2-20: Anchorage profile nonlinear site response analysis with frequency independent viscous damping; Loma Prieta earthquake a) maximum shear strain profile and b) surface response spectra comparisons.

CHAPTER 3 - NUMERICAL MODELING OF FREE-FIELD LATERAL SPREADING CENTRIFUGE TESTS

3.1 Introduction

Lateral displacement of gently sloping ground triggered by seismic shaking –referred to as lateral spreading– can seriously damage lifelines, shoreline structures, and shallow and deep foundations. The design of such infrastructure requires not only predicting whether lateral spreads will occur for a given earthquake and soil conditions but also predicting the consequences of such an event. This involves quantifying lateral displacements and the generation of pore water pressures that result from the triggering of liquefaction.

Many studies are available to evaluate triggering of lateral spreads and the resulting displacements, including empirical techniques, laboratory studies, centrifuge studies, and numerical techniques (Table 3-1). Several computational models to simulate lateral spreading have been developed in the last 15 years (Taboada-Urtuzuastegui and Dobry, 1998; Elgamal et al., 2002; Elgamal et al., 2005; Dobry et al., 2010). In these studies a number of parameters have been calibrated to represent the behavior of a soil experiencing lateral spreading. This paper presents the calibration of a soil constitutive model and the development of numerical analyses to replicate the key elements of behavior observed in centrifuge tests in terms of displacement, acceleration, and pore water pressure time histories. The calibration process highlights the importance of small-strain damping and the need for pressure-dependent dilation parameters to replicate accurately the measurements from free-field lateral spreading centrifuge test. The ability of the calibrated numerical model to reproduce the behavior of soils experiencing lateral spreading is evaluated using the same soil profile geometry and the input motion of a different

centrifuge test. The second centrifuge test was performed as a part of the same overall project as described in the next section.

3.2 Centrifuge experiments of free field lateral spreading

Two free-field lateral spreading centrifuge tests were constructed and tested at the Rensselaer Polytechnic Institute (RPI) centrifuge facility in Troy, New York using a laminar box to allow for large unimpeded downslope soil displacements. The laminar box has internal dimensions of 71 cm long x 35.5 cm in plan and a maximum of 26 cm of height (35.5 m x 17.7 m x 13 m in prototype scale when spun at 50 g). The laminar box is inclined 2º to the horizontal using a stiff wedge at the base of the box. The soil slope is simulated by inclining the whole model 2º to replicate the boundary conditions of the centrifuge test. The soil profile consists of loose Nevada sand with a prototype thickness of 10m underlain by 2m of dense, lightly cemented sand (Figure 3-1).

The free-field lateral spreading centrifuge tests were performed as a part of an ongoing Network for Earthquake Engineering Simulation (NEES) research project. Instrumentation in these centrifuge models included pressure transducers and accelerometers to measure pore water pressure (PWP) and acceleration at numerous locations throughout the model, linear voltage differential transformers (LVDT) and lasers installed on the rings outside the laminar box to measure lateral displacement with depth, and subsurface sand grids and surface tracking markers to measure lateral displacement at discrete locations and depths. Figure 3-1 includes the instrument locations used in the two centrifuge experiments discussed here.

The first free-field lateral spreading centrifuge experiment described here (experiment I-02) was used to calibrate the soil-constitutive numerical model. This centrifuge test was

subjected to a sinusoidal input acceleration motion with a prototype frequency of 1 Hz and peak ground acceleration of 0.28 g (Figure 3-2). The second test (experiment I-03) was used to evaluate the ability of the calibrated model to compute the response of a similar model subject to a different input motion. The input motion applied at the base of experiment I-03 had the same frequency (1 Hz) as in experiment I-02 but lower peak ground acceleration (0.24 g) (Figure 3-3). The two motions recorded at the cemented sand – loose sand interface are used as input motion in the numerical analyses presented in this paper, therefore, the cemented sand layer does not need to be included in the numerical model.

3.3 Numerical simulation approach

The numerical simulations presented in this paper were performed using the finite element framework OpenSees (Mazzoni et al., 2006). This numerical framework employs a two-phase fully-coupled finite element formulation (Parra, 1996; Yang and Elgamal, 2002) based on Biot's theory (Biot, 1962). In this framework, the saturated soil is modeled as a two-phase material implementing the u-p formulation (Chan, 1988) for two- and three-dimensional analyses. In the u-p formulation, the displacement of the soil skeleton (u) and pore pressure (p) are the primary unknowns. Although currently available soil finite elements in the OpenSees framework do not implement a Total Langragian formulation to calculate large strains, the application to numerically simulate lateral spreading problems has been successful as presented by Yang (2000), Elgamal et al. (2002), Elgamal et al. (2003) and Elgamal et al. (2005).

3.3.1 Description of the numerical model

Two different numerical models were developed to model the free-field lateral spreading centrifuge tests; the first numerical model has 2680 nodes (each node with 4 degrees of freedom) and 2133 BrickUP elements and models the behavior of the centrifuge test considering it as a

fully 3D problem. The second model assumed that the behavior the centrifuge test can be modeled correctly assuming a shear beam behavior; 40 nodes and 9 BrickUp elements were used in this model using a boundary conditions of equal displacement constrains (x, y and z) for all the nodes located at the same depth. These two models provided almost identical results for simulations of free-field lateral spreading centrifuge tests, therefore, the shear beam model is used in this paper, Figure 3-4, whereby a free field simulation is completed in 1 minute or less compared to more than 4 hours required for the three dimensional model. In all simulations the inclination of the box of 2º in prototype scale is modeled as proposed by Lu et al. (2010). This assumption better represents the stress field and the inertial conditions of the experiment than the alternative proposed by Taboada (1995) in which a 2º inclination in the small scale centrifuge can be modeled as a 4 to 5º ground surface inclination in prototype scale.

3.3.2 Small strain (viscous) damping in dynamic simulations

For most soils, damping at small strain has a finite non-zero value. Figure 3-5a presents the Menq (2003) family of damping curves for sandy soils with the gradation and mechanical properties of Nevada Sand at different confinement pressures. Small-strain damping values at these confinement pressures range from 0.9 to 2.6%. Figure 3-5b presents damping ratios obtained by Kokusho et al. (2005) for sandy soils by inverse analyses of vertical array records obtained during the 1995 Kobe earthquake at soft soil sites near the earthquake fault zone. These results exhibit the same trend as the laboratory data in Figure 3-5a, although the damping values are a few percent higher in the small strain range. Figure 3-5c presents the small-strain damping profile back-calculated by Park and Hashash (2005) for the Mississippi Embayment. The back-calculated profile shows a decrease in small-strain damping with depth, with small-strain

damping values of 3.5% for the upper 100 meters. Given this information, a range of 1% to 4% small-strain damping was evaluated in the calibration performed in this study.

Constitutive laws are nearly linear at small cyclic strains resulting in negligible hysteretic damping at these strain levels, therefore viscous damping has to be added separately to simulate the small-strain damping observed in soils from laboratory and field studies (e.g., Figure 3-5a). The damping predicted by the pressure dependent soil constitutive model implemented in Opensees [Yang (2000)] for small strains have been estimated using a single element test, obtaining a hysteretic damping of less than 0.04% for shear strains ranging between 0.01 to 0.02%, thus the need to introduce viscous damping (Rayleigh damping) in the numerical simulation in order to reproduce the energy dissipation for small strains. This issue was also reported for 1-D site response analyses [Park and Hashash, (2004), Park and Hashash (2005), Kwok et al. (2007), Phillips and Hashash (2009)]. The viscous damping formulation and selection is important even for higher levels of shakings and at large strains as the error introduced by incorrect choice of viscous damping can be large,

Most time-domain wave propagation codes include viscous damping by implementing the original expression proposed by Rayleigh and Lindsay (1945a) in which the damping matrix results from the addition of two matrices: one proportional to the mass matrix and the other proportional to the stiffness matrix as shown in equation (3-1).

$$[C] = a_0[M] + a_1[K] \tag{3-1}$$

where a_0 and a_1 are scalar values selected to obtain given damping values for two control frequencies. Viscous damping calculated using the Rayleigh and Lindsay (1945) solution is frequency-dependent, a result that is inconsistent with most available experimental data which indicate that material damping in soils is frequency-independent at very small strain levels within the seismic frequency band of 0.001 to 10 Hz (Lai and Rix, 1998b).

Hudson et al. (1994) and Park and Hashash (2004b) described the application of the full Rayleigh formulation in 2-D and 1-D site response analysis respectively. For soil profiles with a constant damping ratio, scalar values of a_0 and a_1 can be computed using two significant natural modes i and j using equation (3-2):

$$\begin{bmatrix}\xi_i \\ \xi_j\end{bmatrix} = \frac{1}{2}\begin{bmatrix}\frac{2\pi}{f_i} & \frac{f_i}{2\pi} \\ \frac{2\pi}{f_j} & \frac{f_j}{2\pi}\end{bmatrix}\{a_0 \quad a_1\} \tag{3-2}$$

where ξ_i and ξ_j are the damping ratios for the frequencies f_i and f_j of the system, respectively. For site response analysis the natural frequency of the selected mode is commonly calculated as (Kramer, 1996a):

$$f_n = (2n-1)\frac{V_s}{4H} \tag{3-3}$$

where n is the mode number and f_n is the natural frequency of the corresponding mode, Vs is the average shear wave velocity of the soil profile, and H is the total thickness of the soil column.

It is common practice to choose frequencies that correspond to the first mode of the soil column and a higher mode that corresponds to the predominant frequency of the input motion. Kwok et al. (2007a) recommended a value equal to five times the natural frequency. Park and

Hashash (2004b) also provide recommendations to estimate these two frequencies. Equal values of modal damping ratios are specified at each of the two modes. In contrast, Phillips and Hashash (2009) proposed a frequency-independent solution using rational indices instead of integers to calculate the viscous damping matrix [C]. The construction of a frequency-independent viscous damping matrix has only been fully implemented for 1D site response analyses of level ground. The frequency independent viscous damping solution is computationally expensive for 3D analyses, and has not been implemented in the OpenSees finite element framework and therefore mass matrix and initial stiffness matrix proportional Rayleigh damping is used in the analysis presented in this paper.

3.3.3 Constitutive modeling of soil behavior

The behavior of soils experiencing lateral spreading was modeled using the pressure-dependent soil constitutive model proposed by (Parra, 1996; Yang, 2000; Yang and Elgamal, 2002). The term pressure-dependent for this soil constitutive model refers to the change of the shear strength and stiffness with mean effective stress in contrast to the overburden pressure-dependent small-strain damping described above. For clarity, we refer to the constitutive model as an effective stress constitutive model. This effective stress constitutive model is developed based on the original framework proposed by Prevost (1985) and focuses on simulating the liquefaction-induced shear strain accumulation mechanism (Yang and Elgamal, 2002; Elgamal et al., 2003) and the deviatoric-volumetric strain coupling, i.e., dilatancy, during cyclic loading. The main parameters of the model include standard dynamic soil properties such as small-strain shear modulus and friction angle, as well as parameters to control dilatancy (i.e., phase transformation angle, contraction parameter c_1, and dilation parameters d_1 and d_2) and the parameters controlling liquefaction-induced, perfectly-plastic shear strain accumulation. The

properties used for the effective stress constitutive model are presented in Table 3-2. The numerical models developed for this paper use the values of friction angle, permeability and G_0 determined for Nevada Sand as a part of the experiments developed in the Verification of Liquefaction Analysis by Centrifuge Studies (VELACS) geotechnical investigation program and the value of phase transformation angle suggested by Elgamal et al. (2002) for Nevada sand with relative density (D_r) between 35 to 45% (which are close to the D_r values of 30 to 40% used in the centrifuge experiments). The other soil constitutive parameters such as: dilation parameters, number of yield surfaces, reference confinement pressure and peak shear strain have been estimated following the recommendations presented in Elgamal et al. (2010) for cohesionless soils with relative density between 35 and 45%.

As presented in Yang et al. (2003), dilation parameter c_1 is used in the numerical model to represent the observation whereby the rate of contraction is dependent on the preceding dilation phase (Papadimitrou, 2001). Thus a higher value of dilation parameter c_1 induces a higher contraction rate after a dilation phase. Dilation parameters d_1 and d_2 define the dilation tendency that increases with the accumulation of shear strain, a phenomenon that has been experimentally observed by Kabilamany and Ishihara (1990). Higher values of dilation parameters d_1 and d_2 will induce a more pronounced dilation phase as shear strain is accumulated.

The permeability used in the simulations corresponds to the scaled value for a centrifuge test at 50 g using Nevada sand with water as the pore fluid; in prototype scale the permeability is equal to 50 times the permeability of Nevada Sand measured in laboratory tests.

3.3.4 Model calibration procedure

Two different sets of calibration analyses were performed to improve the simulation of lateral spreading under free-field conditions using the measurements of experiment I-02. The first calibration focused on defining viscous damping in the numerical simulation. The second calibration focused on defining the constitutive parameters required to define the yield function and the hardening and flow rules (contraction parameter c_1 and dilation parameters d_1 and d_2). The second calibration did not include changing the soil friction and phase transformation angle, its density and its maximum shear modulus because these parameters have been estimated using the results of laboratory test or numerical back-calculations for Nevada Sand with the same relative density as the one used in the centrifuge experiments.

3.4 Viscous damping calibration

In the viscous damping calibration exercise, the soil constitutive parameters listed in Table 3-2 were employed. In the first stage of calibration, the viscous damping target value was selected, while in the second stage, we evaluated the effect of varying the control frequencies f_i and f_j.

3.4.1 Variation of the viscous damping target value for constant control frequencies

Figure 3-6 shows a schematic of the soil profile geometry and the frequency dependent damping ratio for target values equal to 1%, 2%, 3% and 4% computed using Equation 3-2. The control frequencies f_i and f_j correspond to the natural frequency of the soil profile [$V_s/4H$ = 2.5 Hz, assuming an average shear wave velocity (V_s) of 100 m/s] and five times the natural frequency (12.5 Hz) respectively as recommended by Kwok et al. (2007a). The selection of frequencies for Rayleigh Damping is model dependent, but motion independent and is based on the work of Kwok et al (2007). If the initial natural frequency of the model changes the selected

frequencies used in the numerical simulations have to be changed as suggested in Kwok et al. (2007).

Figure 3-7 compares the computed boundary lateral displacements (displacements measured at the laminar box rings) and the corresponding centrifuge test measurements. Numerically-simulated permanent surface displacements differed by nearly 40% using 1% and 4% viscous damping values (4.16 m and 3.00 m, respectively). Higher viscous damping values result in greater energy dissipation and smaller lateral displacements. The impact of the viscous damping ratio on lateral displacements decreases with increasing depth. For example, at a depth of -7.5 m the displacement time histories calculated for different viscous damping levels differ only slightly (Figure 3-7e), and the simulated displacements at this depth systematically under-predict the lateral displacement measured in the centrifuge test.

The concordance correlation coefficient (CCC) proposed by Lin (1989) is used to evaluate the agreement between the numerical simulations and the centrifuge test measurements. The CCC characterizes the degree of concordance between computed and target and is scaled to range from -1 to 1, where 1 is perfect agreement between the two datasets, -1 is perfect reverse agreement, and zero is no agreement. The CCC is estimated using the mean (Y_j), variance (S_j^2), and covariance (S_{ij}^2) of the measured and computed time histories as follows:

$$CCC = \frac{2 * S_{12}}{{S_1}^2 + {S_2}^2 + (Y_1 - Y_2)^2} \tag{3-4}$$

where

$${S_j}^2 = \frac{1}{n}\sum_{i=1}^{n}\left(Y_{ij} - Y_j\right)^2 \ , j = 1,2 \tag{3-5}$$

$$S_{12} = \frac{1}{n}\sum_{i=1}^{n}(Y_{i1} - Y_1)(Y_{i2} - Y_2)$$

Table 3-3 presents the CCC values for the lateral displacement time histories at different depths. Based on these results the numerical model with 3% viscous damping provides the best overall match for the lateral boundary displacements measured in experiment I-02.

Figure 3-8 compares measured acceleration time histories to those computed using various damping ratios. Near-surface downslope acceleration amplitudes (shown as positive amplitudes) decrease in both the centrifuge experiments and numerical simulations as a result of liquefaction. The acceleration time histories (Figure 3-8) exhibit the same trend as the lateral displacement, with simulations using lower viscous damping target values predicting higher peak accelerations.

Comparing acceleration records using only the peak values can be cumbersome and potentially misleading. The use of energy-based parameters, such as Arias Intensity, provides an alternative comparative measure. The Arias intensity was calculated for each acceleration time history (numerical simulation result and centrifuge measurement) using equation (3-6).

$$Arias\ Intensity = \frac{\pi}{2g}\int_0^{Td} a(t)^2 dt \tag{3-6}$$

where g is the acceleration of gravity, T_d is the duration of the motion and $a(t)$ is the acceleration time history.

Figure 3-9 compares the measured and simulated Arias intensities at various instrument depths. As viscous damping increases, the energy (i.e., Arias intensity) transmitted through the

soil profile decreases. All the simulations show a decrease of the Arias intensity for locations closer to the surface, consistent with the centrifuge and simulation acceleration time histories. Table 3-4 presents the CCC for the Arias intensity at the three different depths. Based on Arias intensity, the numerical models using 3% viscous damping provide the best overall match with the centrifuge measurements, matching closely the Arias intensity time series for the middle of the soil profile (Figure 3-9h) and under-predicting the Arias intensity for depths of 2.5m and 7.5m.

Figure 3-10 compares measured and simulated pore water pressure time histories. The large downward spikes correspond to soil dilation during each cycle. In the simulations, the size of the downward spikes decreases as the viscous damping increases. Numerical models with 2 and 3% damping ratios reproduce better the size of the downward spikes compared with the centrifuge test measurements at the three different depths. Considering all centrifuge test measurements, 3% viscous damping provides the closest response to that measured in experiment I-02.

3.4.2 Variation of the control frequencies for constant viscous damping value

A second set of simulations were conducted to evaluate control frequency selection on the computed response using the best-fit target viscous damping equal to 3%. Frequency f_i was set equal to the natural frequency of the soil column (2.5 Hz), and f_j was set equal to three, five or eight times the natural frequency of the soil column (7.5 Hz, 12.5 Hz and 20.0 Hz respectively). Figure 3-11 is a schematic of the soil profile geometry and the frequency dependent damping ratios for the different combinations of f_i and f_j.

Figure 3-12 compares the lateral displacements measured in centrifuge experiment I-02 and the simulations. Only slight differences are observed for the three different combinations of

control frequencies. Similarly, only slight differences were observed for acceleration and pore water pressure time histories (not shown). Arias intensity (Figure 3-13) is higher for the case with f_j = 20 Hz, which is due to the lower viscous damping at the high frequencies.

This set of analyses show that although changing the control frequencies generates slight changes in the overall response of the soil profile, the selection of the control frequencies is not as significant as the selection of the viscous damping target value. In the following analyses, the control frequencies f_i and f_j were set equal to the natural frequency of the soil profile and five times the natural frequency, respectively, as recommended by Kwok et al. (2007a).

3.5 Soil constitutive model parameter with viscous damping calibration

The simulations described above showed that constant dilation parameters reasonably matched the measured soil response at certain depths; however, at other depths the model under- or over-predicted the response. Simultaneously matching the behavior observed in centrifuge experiment I-02 requires the introduction of overburden pressure-dependent dilation parameters. Several functional forms were evaluated to improve the numerical model. The functional form that provided the best results in terms of fitting the centrifuge lateral displacement measurements is presented in equation (3-7).

$$Contraction\ or\ Dilation\ Parameter = p_1 \pm p_2 \left[1 - \frac{1}{1 + \left(\frac{\sigma'_{vo}}{\sigma_{ref}} \right)^{10}} \right] \tag{3-7}$$

where p_1 and p_2 are dimensionless parameters selected to obtain the best agreement between the simulation results and the centrifuge measurements, σ'_{v0} is the initial effective vertical stress, and σ_{ref} is the reference stress (80 kPa in this case). This functional form results in

an almost constant value equal to p_1 for initial effective vertical stress lower than 70% of the reference stress and a constant value equal to $p_1 \pm p_2$ (positive sign for the contraction parameter c_1 and negative sign for the dilation parameters d_1 and d_2) for initial vertical stresses higher than 150% of the reference stress. In this part of the calibration exercise we allow the dilation parameters to vary with an assumed value of viscous damping, where, increasing viscous damping corresponds to an increase in contraction parameter c_1 and a decrease of dilation parameters d_1 and d_2. Figure 3-14 presents the calibration results for the dilation parameters. The calculated values of p_1 and p_2 for calculating the dilation parameters are presented in Table 3-5.

Figure 3-15 through Figure 3-18 compare the simulated and measured boundary displacements, acceleration time history, Arias intensity and pore water pressure, respectively, where the calibrated models consider different viscous damping levels and overburden pressure-dependent dilation parameters. The calibration process results in almost the exact same displacements for the calibrated constitutive models using the four different levels of viscous damping. Although numerical simulations using the different calibrated soil constitutive models were able to reproduce the boundary displacements measured in the centrifuge test at different levels (Figure 3-15 and Table 3-6), important differences in terms of acceleration, Arias intensity and pore water pressure response were observed for the different levels of viscous damping.

Simulations with low viscous damping levels resulted in high downslope acceleration spikes that were not recorded in the centrifuge test. Models calibrated to higher levels of viscous damping resulted in lower downslope acceleration spikes which are consistent with the centrifuge acceleration records. The differences between the simulated and measured time histories were greater for numerical models with low levels of viscous damping and at locations closer to the surface. Figure 3-16 illustrates that the numerical models with 3% and 4% viscous

damping were able to better reproduce the acceleration records at the three instrument depths. The Arias intensity calculated using the acceleration records (Figure 3-17) for the simulations using the calibrated numerical models result in higher Arias intensities for the upper part of the profile (level -2.50 m), almost the same values for the middle (level -5.00 m) and lower values for the bottom of the soil column (level -7.50 m) compared with the results of the numerical model with constant dilation parameters and the same input motion (Figure 3-9).

Table 3-7 presents the CCC values calculated for the Arias intensity time histories. Based on these results it can be observed that using the calibrated model for viscous damping equal to 3% results in a better match with the centrifuge measurements than the other calibrated soil constitutive models. The horizontal displacement and Arias intensity time histories predicted using this model reproduce more accurately the centrifuge test measurements than the model using constant dilation parameters and 3% viscous damping.

Pore water pressure records (Figure 3-18) for numerical models with lower values of viscous damping result in larger downward pore water pressure spikes than centrifuge test records. Higher downward pore water pressure spikes correspond to a more dilative soil response which can be explained by the use of higher values for the dilation parameters and lower values for the contraction parameter when lower viscous values are used. The numerical model using the calibrated soil constitutive model with 3% viscous damping best reproduces the downward pore water pressure spikes at different depths.

As described above, the CCC values for comparisons of simulated and measured displacement and Arias intensity, as well as the downward pore water pressure spike sizes illustrate that the model calibrated for 3% viscous damping provides the best overall fit to the

centrifuge results. Although a 3% viscous damping value is greater than the maximum limit computed by the family of curves proposed by Menq (2003) for a soil with mechanical and gradation properties similar to Nevada Sand (Figure 3-5a), the value is consistent with the viscous damping back-calculated by Kokusho et al. (2005) and Park and Hashash (2005) (Figure 3-5b and Figure 3-5c respectively), for sandy soils at depths less than 10 m.

3.5.1 Computed response of centrifuge lateral spreading test with a different input motion

A numerical simulation of experiment I-03 was conducted using the model calibrated with experiment I-02. The input motion for experiment I-03 had a lower acceleration than I-02. Figure 3-19 and Figure 3-20 compare the simulated and measured lateral displacement, acceleration, Arias intensity, and pore water pressure time histories.

The CCC statistic was calculated to determine the prediction quality for lateral displacements at different depths; these CCC values are present in Table 3-8. High CCC values were obtained for displacements predicted at the surface, and depths of 1.25 m, 2.50 m and 5.70 m. The CCC values for a depth of 7.50 m were considerably lower, as the numerical simulation systematically under-predicted the displacement at a depth of 7.50 m. Nevertheless, we consider the computed response to have satisfactorily captured the salient aspects of the soil response during lateral spreading.

Computed upslope and downslope peak accelerations values are in good agreement with measurements for the three different depths presented in Figure 3-20. The Arias intensity showed good agreement at the upper and lower locations (Figure 3-20d and Figure 3-20f). However, the calibrated model under-predicted Arias intensity in the middle of the soil deposit (Figure 3-20e). Table 3-9 presents the CCC values calculated for the Arias intensities at the three different

depths. These CCC values demonstrate that the model is able to predict reasonable well the energy content of the accelerations time histories for the three different depths.

Although the overall prediction of the numerical simulation closely replicated the centrifuge measurements, important differences were observed for the pore water pressure time histories at a depth of 2.5 m (Figure 3-20g). This difference was observed even under static conditions prior to shaking. This "offset" likely resulted from the placement depth of the pressure transducer in the centrifuge experiment being slightly different than reported, settlement of the pressure transducers within the loose sand stratum during spin up, or from a lower phreatic level. The phreatic level may change slightly during spin up in the centrifuge tests as the rubber membrane (used to prevent water leakage) conforms more closely to the corners of the laminar container. This conformance results in a slight curvature of the water surface due to the relatively small radius of the centrifuge (2.8m). Unfortunately, the exact water level in the centrifuge test cannot be accurately measured in-flight. Regardless of the source of the "offset" between the measured and simulated pore water pressures, the downward pore water pressure spikes predicted by the simulation were in phase throughout shaking and have nearly the same minimum values as the measured pore water pressure records at each depth.

3.6 Tables and Figures

Table 3-1: Brief list of recent lateral spreading studies.

Empirical techniques	(Youd and Perkins, 1987); (Hamada and O'Rourke, 1992); (Bartlett and Youd, 1992); (Rauch and Martin, 2000); (Youd et al., 2002); (Zhang et al., 2004); (Olson and Johnson, 2008)
Laboratory studies	(Seed et al., 1985); (Kuwano and Ishihara, 1988); (Shamoto et al., 1998); (Cetin et al., 2004)
Centrifuge studies	(Taboada-Urtuzuastegui and Dobry, 1998);(Sharp et al., 2003); (Kutter et al., 2004)
Numerical techniques	(Keane and Prevost, 1990) ; (Chiru-Danzer et al., 2001); (Baziar and Ghorbani, 2005) ; (Elgamal et al., 2005)

Table 3-2: Effective stress constitutive model parameters for Nevada Sand (Dr = 35-45%).

Variable	Value	Units
Mass density	1980	kg/m^3
Ref. shear modulus	33000	kPa
Ref. mean confinement	80	kPa
Confinement dependence coeff.	0.5	---
Friction angle	31.4	°
Peak shear strain	10	%
Number of Yield surfaces	20	---
Phase transformation angle	26.5	°
Contraction parameter, c_1	0.11	---
Dilation parameter 1, d_1	0.30	---
Dilation parameter 2, d_2	1	---
Liquefaction parameter (γ_y)	0.01	---
Permeability coefficient	0.0033	m/s

Table 3-3: Concordance correlation coefficient (CCC) for lateral displacements time histories at different depths. Numerical simulations using constant dilation parameters vs. experiment I-02.

Depth (m)	$\xi_{small\ strain} = 1\%$	$\xi_{small\ strain} = 2\%$	$\xi_{small\ strain} = 3\%$	$\xi_{small\ strain} = 4\%$
0.00	0.96	0.97	0.97	0.93
1.25	0.94	0.96	0.98	0.96
4.30	0.97	0.96	0.96	0.93
5.70	0.96	0.96	0.96	0.94
7.50	0.66	0.56	0.67	0.63

Table 3-4: Concordance correlation coefficient (CCC) for Arias intensity time histories at different depths. Numerical simulations using constant dilation parameters vs. experiment I-02.

Depth (m)	$\xi_{small\ strain} = 1\%$	$\xi_{small\ strain} = 2\%$	$\xi_{small\ strain} = 3\%$	$\xi_{small\ strain} = 4\%$
2.50	0.77	0.88	0.90	0.83
5.00	0.75	0.87	0.99	0.99
7.50	0.98	1.00	0.97	0.96

Table 3-5: Calculated p_1 and p_2 values for different small strain damping values

	$\xi_{Small\ strain} = 1\%$		$\xi_{Small\ strain} = 2\%$		$\xi_{Small\ strain} = 3\%$		$\xi_{Small\ strain} = 4\%$	
Parameter	p_1	p_2	p_1	p_2	p_1	p_2	p_1	p_2
c_1	0.070	0.070	0.080	0.070	0.090	0.070	0.110	0.045
d_1	0.400	0.110	0.395	0.110	0.380	0.110	0.350	0.075
d_2	2.000	1.300	1.900	1.200	1.700	0.980	1.300	0.500

Table 3-6: Concordance correlation coefficient (CCC) for lateral displacements time histories at different depths. Numerical simulations using calibrated dilation parameters vs. experiment I-02.

Depth (m)	$\xi_{small\ strain} = 1\%$	$\xi_{small\ strain} = 2\%$	$\xi_{small\ strain} = 3\%$	$\xi_{small\ strain} = 4\%$
0.00	0.98	0.98	0.97	0.96
1.25	0.98	0.98	0.98	0.98
4.30	0.95	0.97	0.97	0.98
5.70	0.95	0.96	0.96	0.95
7.50	0.80	0.82	0.90	0.95

Table 3-7: Concordance correlation coefficient (CCC) for Arias intensity time histories at different depths. Numerical simulations using calibrated dilation parameters vs. experiment I-02.

Depth (m)	$\xi_{small\ strain} = 1\%$	$\xi_{small\ strain} = 2\%$	$\xi_{small\ strain} = 3\%$	$\xi_{small\ strain} = 4\%$
2.50	0.51	0.72	0.94	0.78
5.00	0.76	0.85	0.99	0.96
7.50	0.98	0.99	0.97	0.90

Table 3-8: Concordance correlation coefficient (CCC) for the displacement time histories at different depths. Numerical simulations using calibrated dilation parameters vs. experiment I-03.

Depth (m)	CCC
Surface	0.99
1.25	0.98
2.50	0.98
5.70	0.98
7.50	0.79

Table 3-9: Concordance correlation coefficient (CCC) for the Arias intensity time histories at different depths. Numerical simulations using calibrated dilation parameters vs. experiment I-03.

Depth (m)	CCC
2.50	0.96
5.00	0.95
7.50	0.99

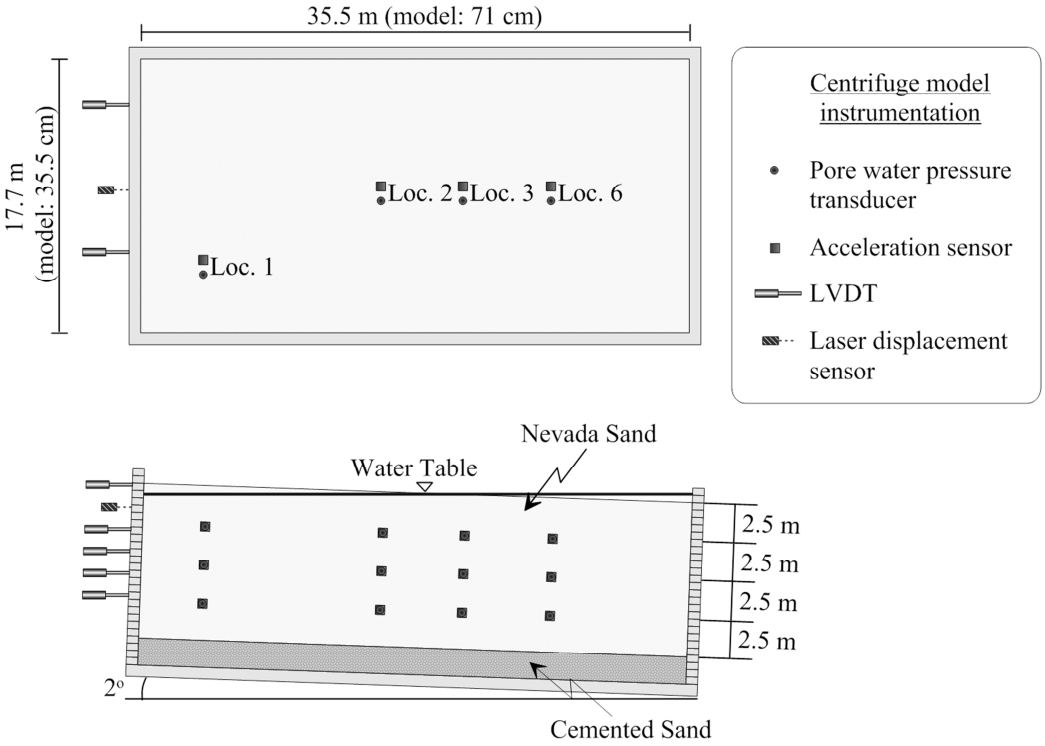

Figure 3-1: Schematic centrifuge tests configuration and instrument location. Dimensions in prototype scale.

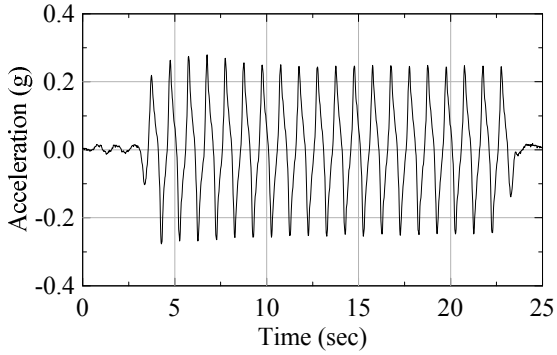

Figure 3-2: Input acceleration time history applied at the base of experiment I-02.

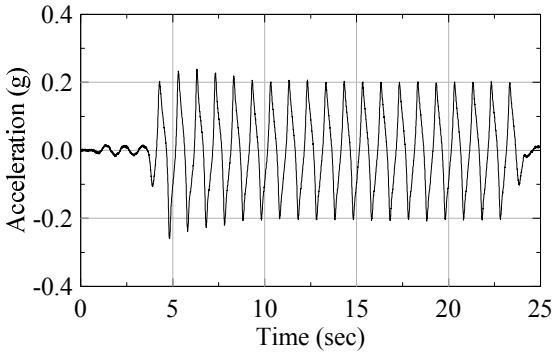

Figure 3-3: Input acceleration time history applied at the base of experiment I-03.

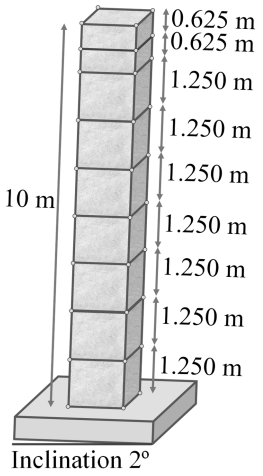

Figure 3-4: Simplified one dimensional shear beam numerical model.

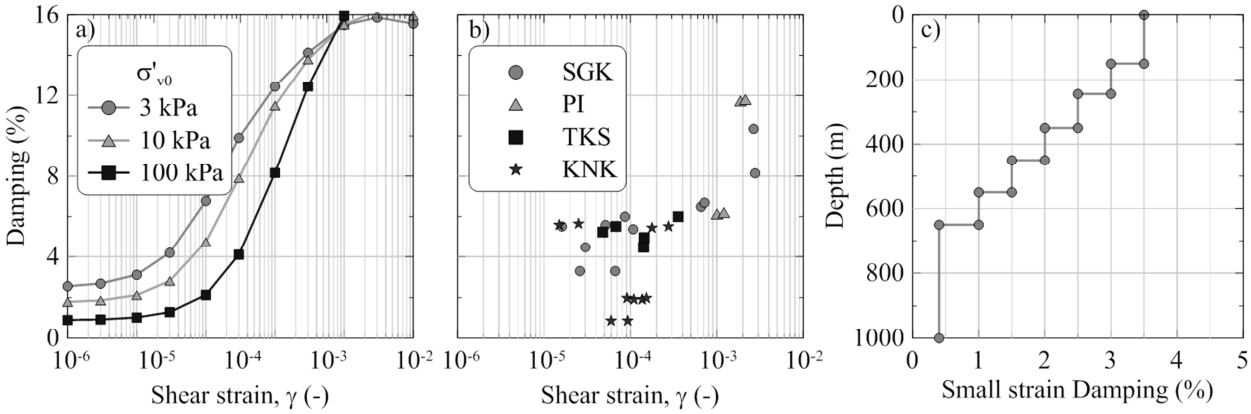

Figure 3-5: Damping values for sands, a) damping curves calculated for sands (Menq, 2003), b) back calculated damping curve for sands at four different sites (Kokusho et al., 2005) and c) back-calculated viscous damping profile for Mississippi Embayment (Park and Hashash, 2005).

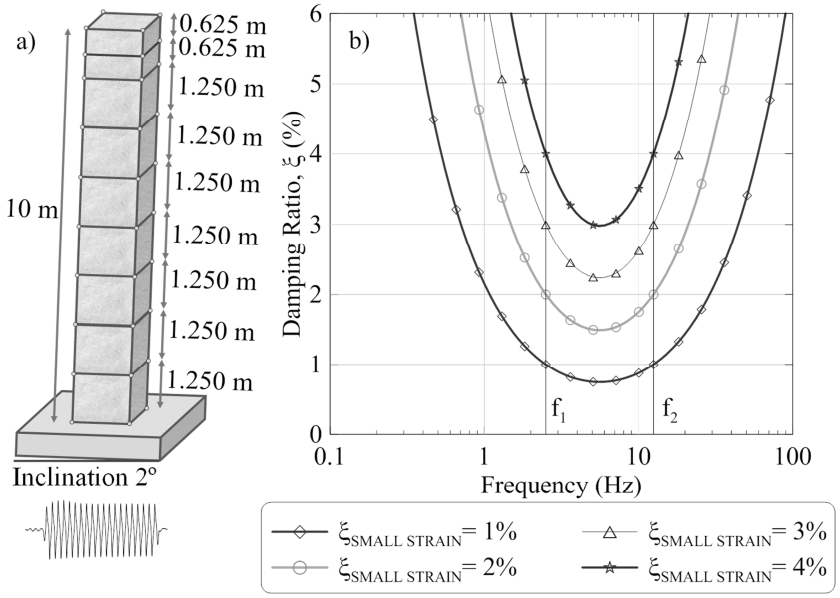

Figure 3-6: Wave propagation on saturated 2 degree sloping sand deposit a) Soil Profile geometry b) Damping variation.

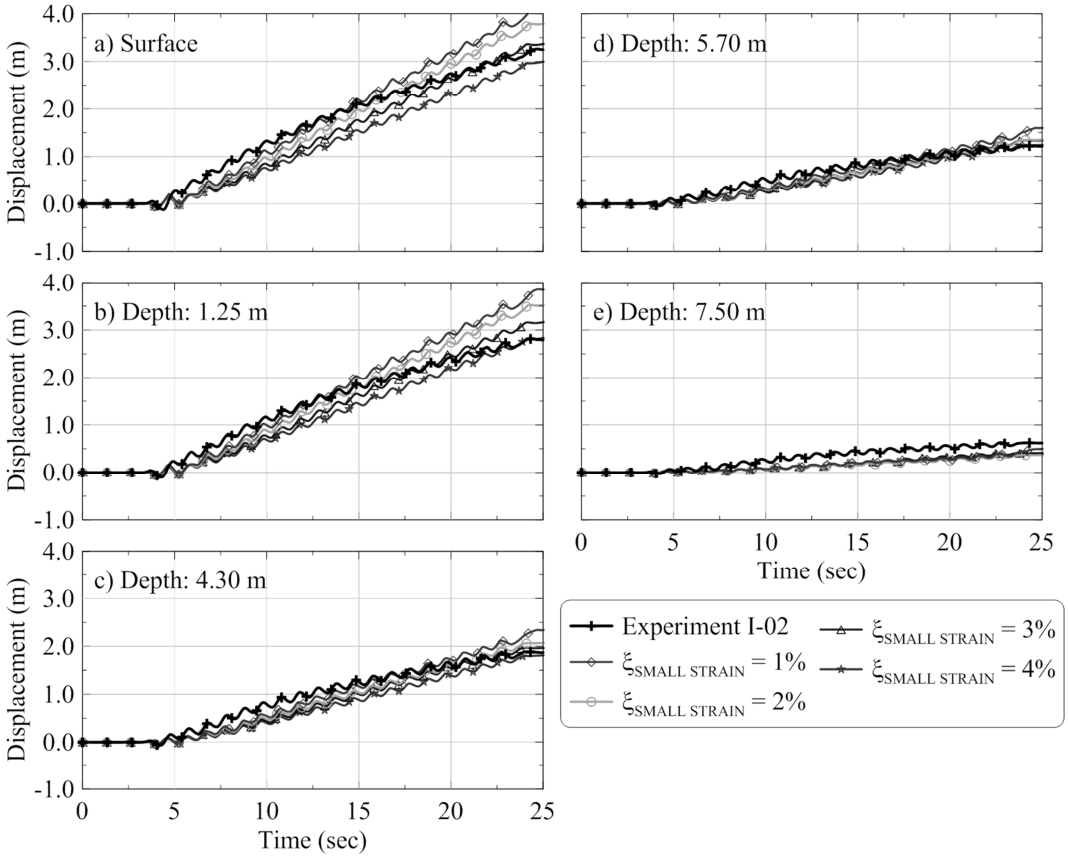

Figure 3-7: Comparison of boundary displacements for numerical simulations and centrifuge experiment I-02 using different viscous damping values.

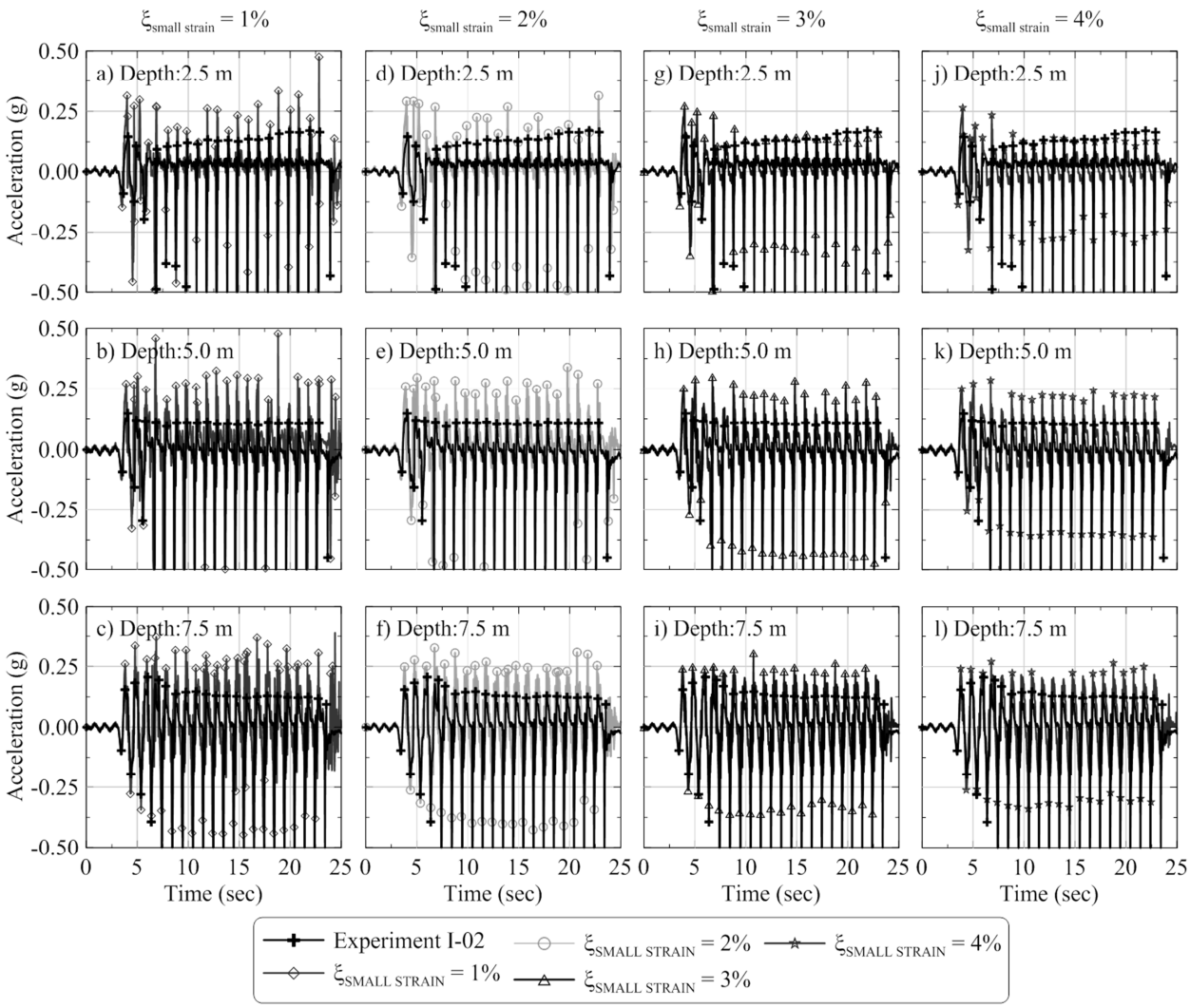

Figure 3-8: Comparison of acceleration time history for numerical simulations and centrifuge experiment I-02 using different viscous damping. Positive accelerations are downslope and negative accelerations are upslope.

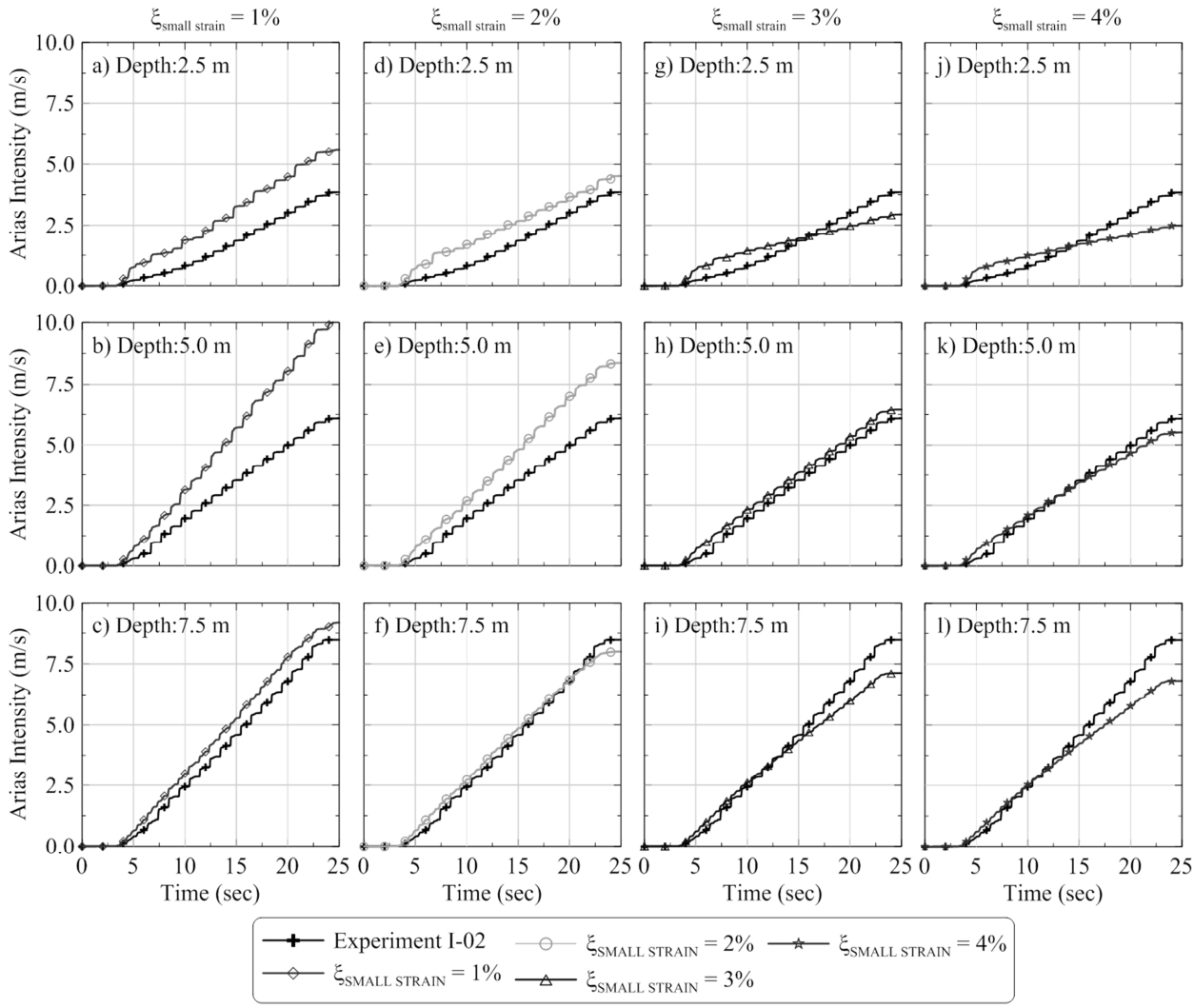

Figure 3-9: Comparison of Arias Intensity time history for numerical simulations and centrifuge experiment I-02 using different viscous damping.

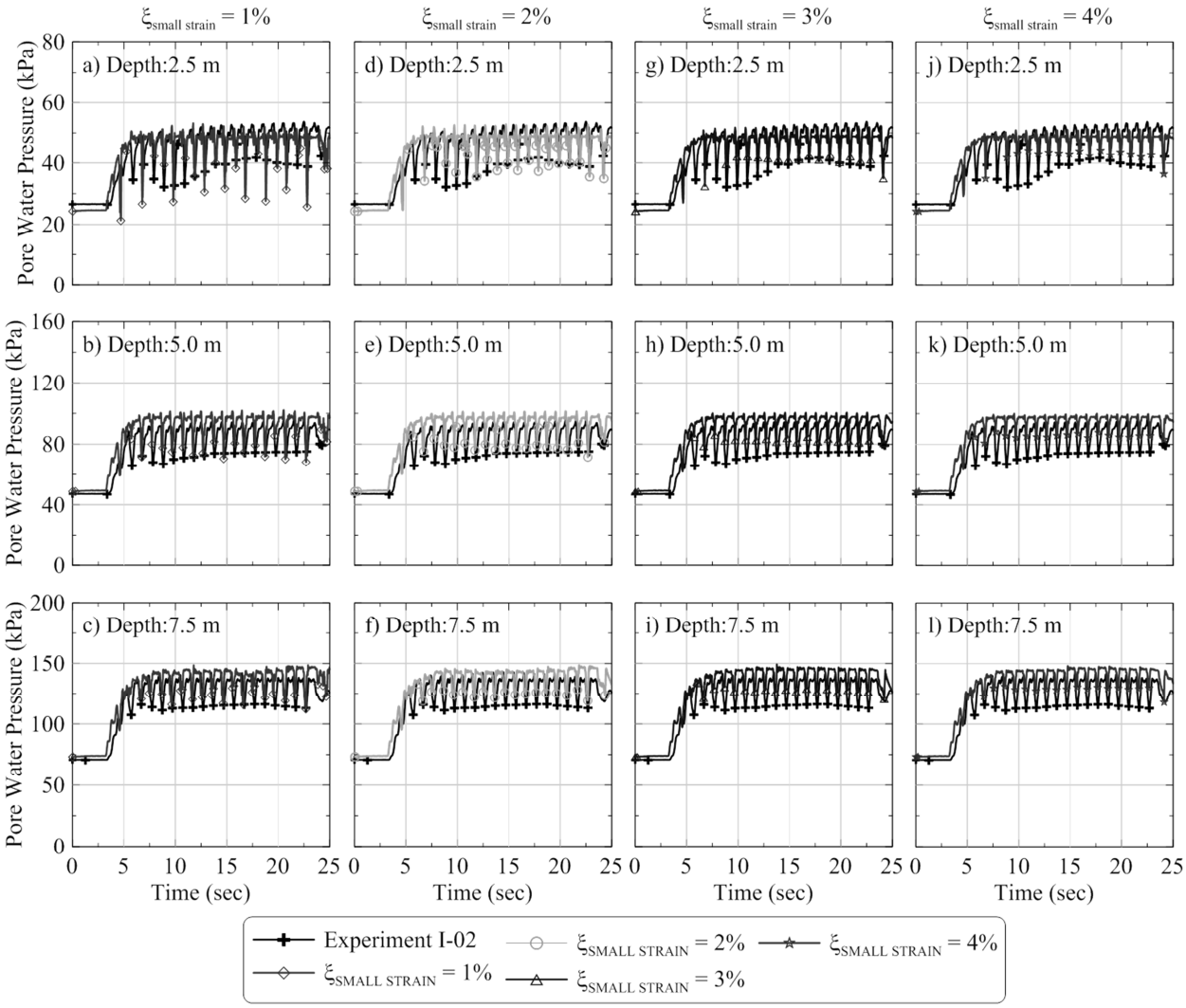

Figure 3-10: Comparison of pore water pressure time history for numerical simulations and centrifuge experiment I-02 using different viscous damping.

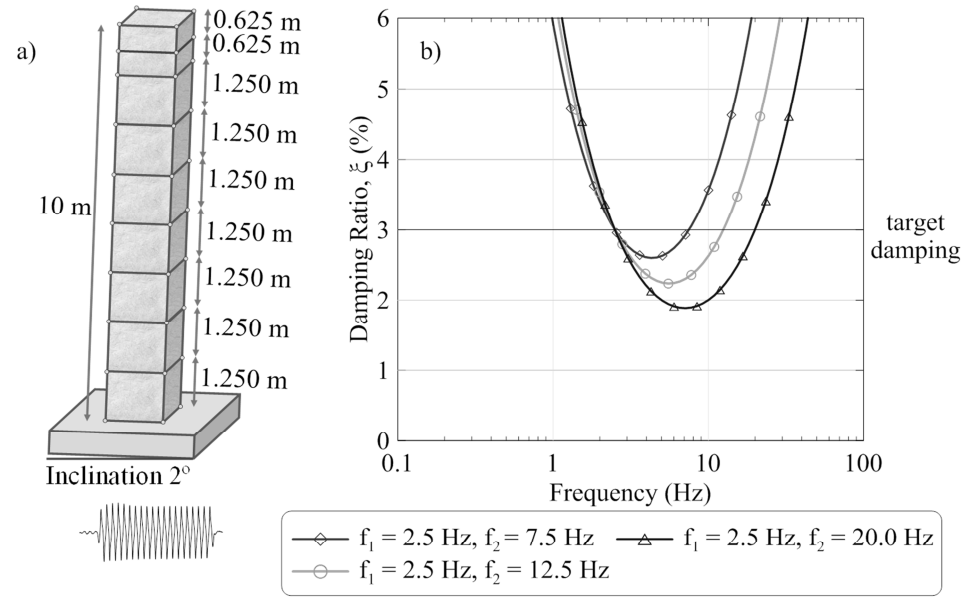

Figure 3-11: Wave propagation on saturated 2 degree sloping sand deposit a) Soil Profile geometry b) Damping variation.

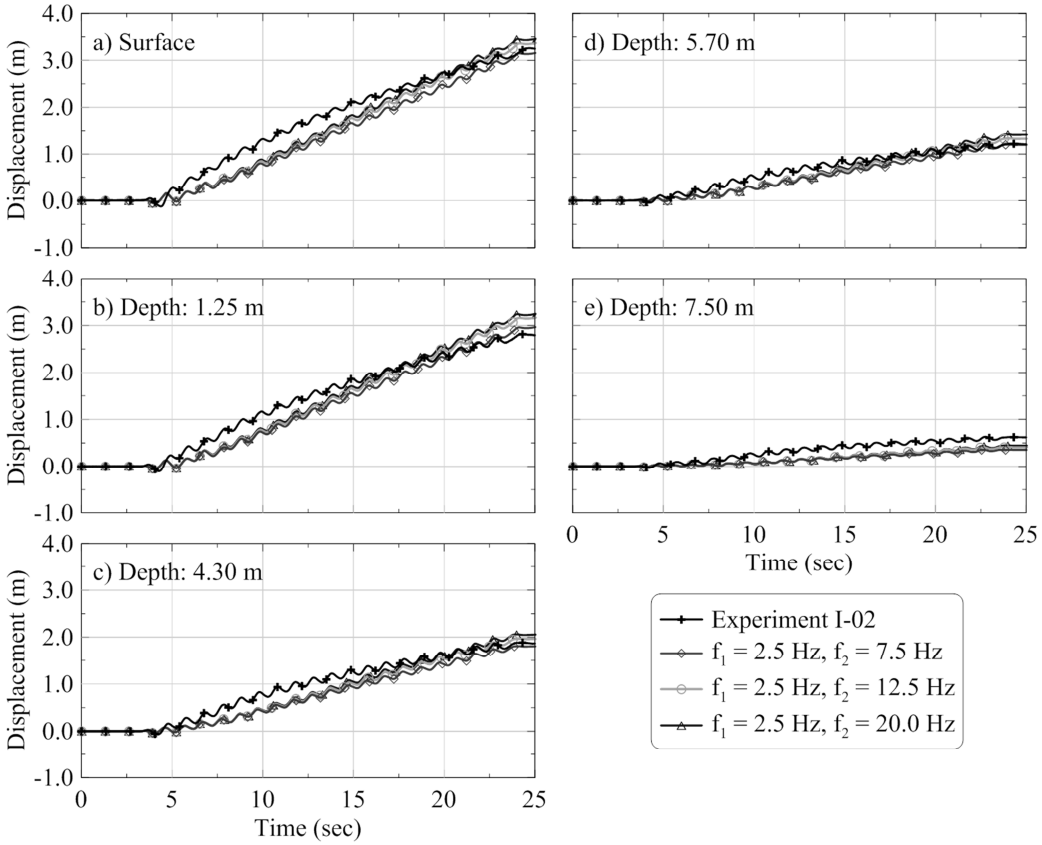

Figure 3-12: Comparison of boundary displacements for numerical simulations and centrifuge experiment I-02 using different control frequencies.

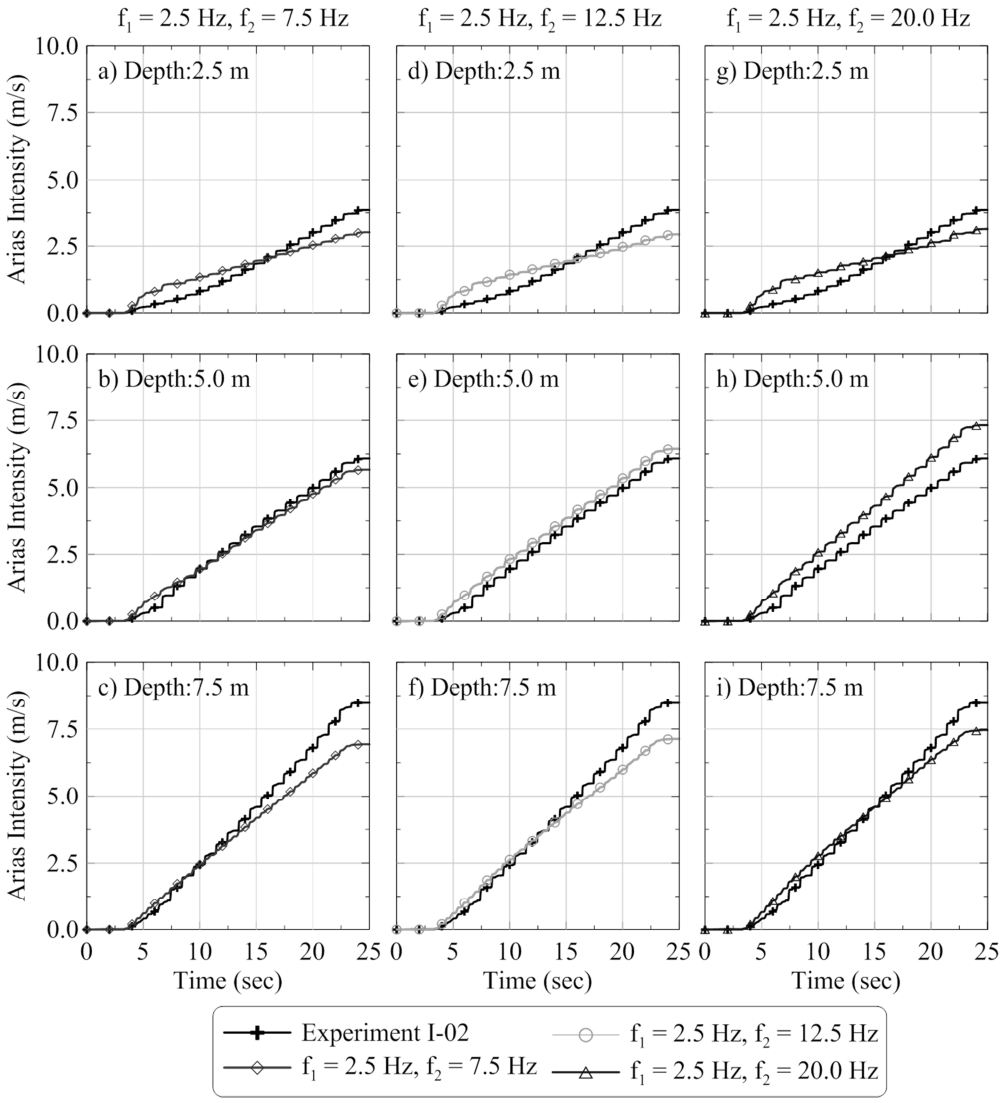

Figure 3-13: Comparison of Arias intensity time history for numerical simulations and centrifuge experiment I-02 using different control frequencies.

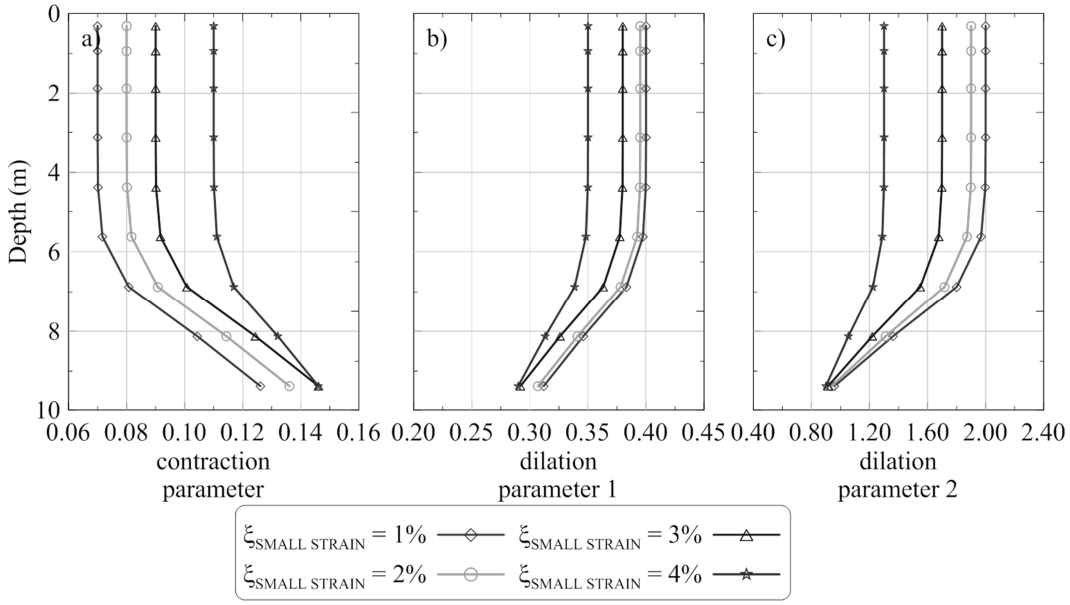

Figure 3-14: Proposed depth-dependent dilation parameters corresponding to various small-strain damping values developed for Yang (2000) effective-stress constitutive model.

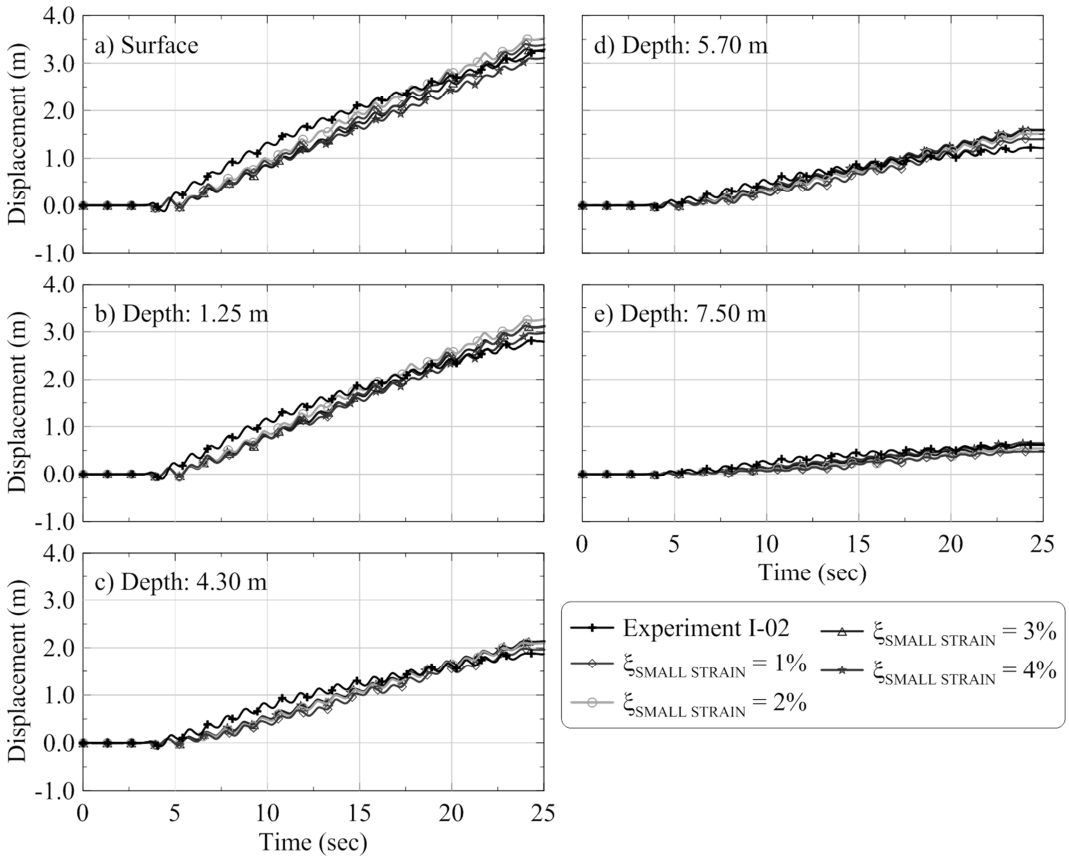

Figure 3-15: Comparison of boundary displacements for numerical simulations for calibrated models using different viscous damping values and centrifuge experiment I-02.

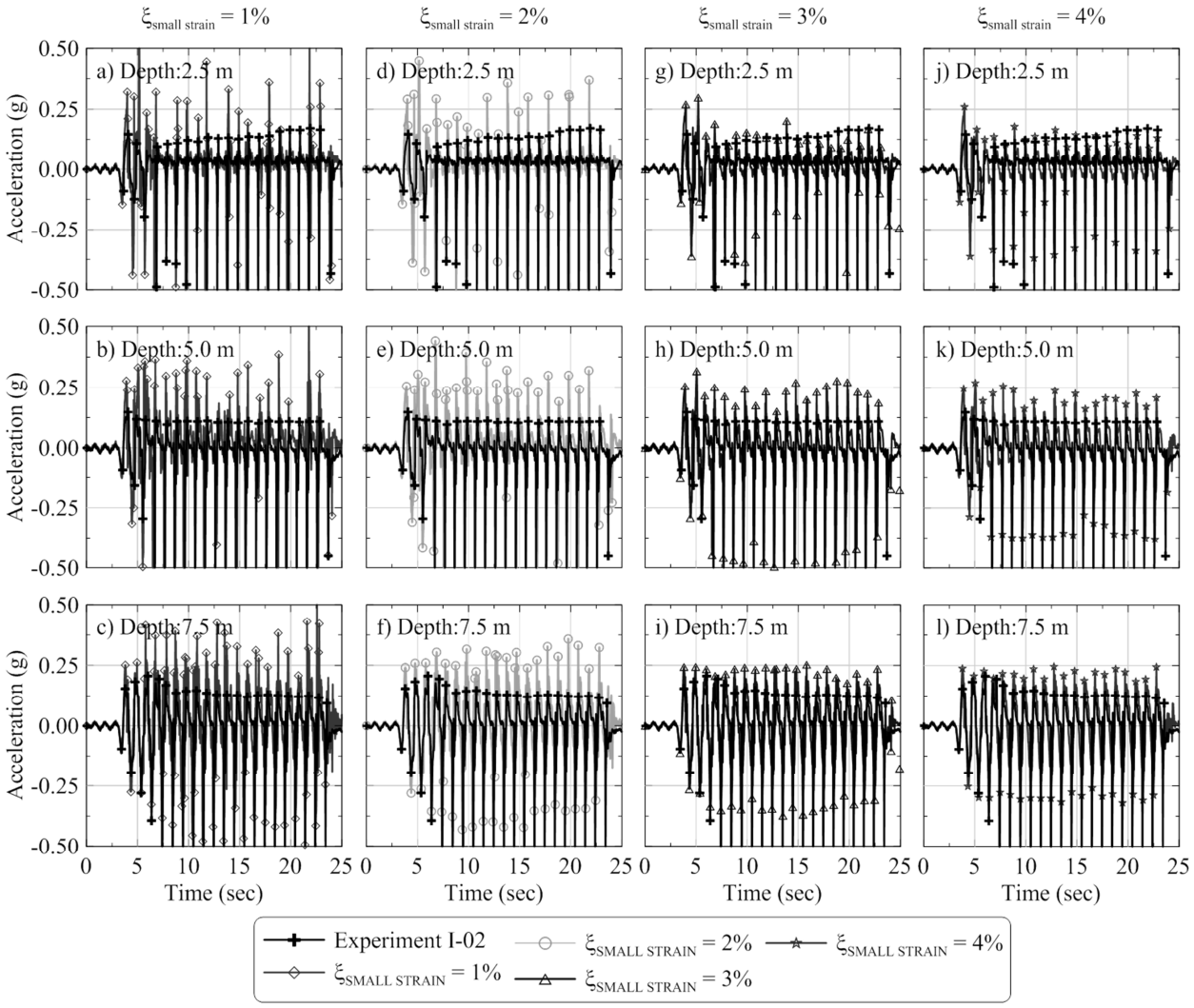

Figure 3-16: Comparison of acceleration time history for numerical simulations for calibrated models using different viscous damping values and centrifuge experiment I-02.

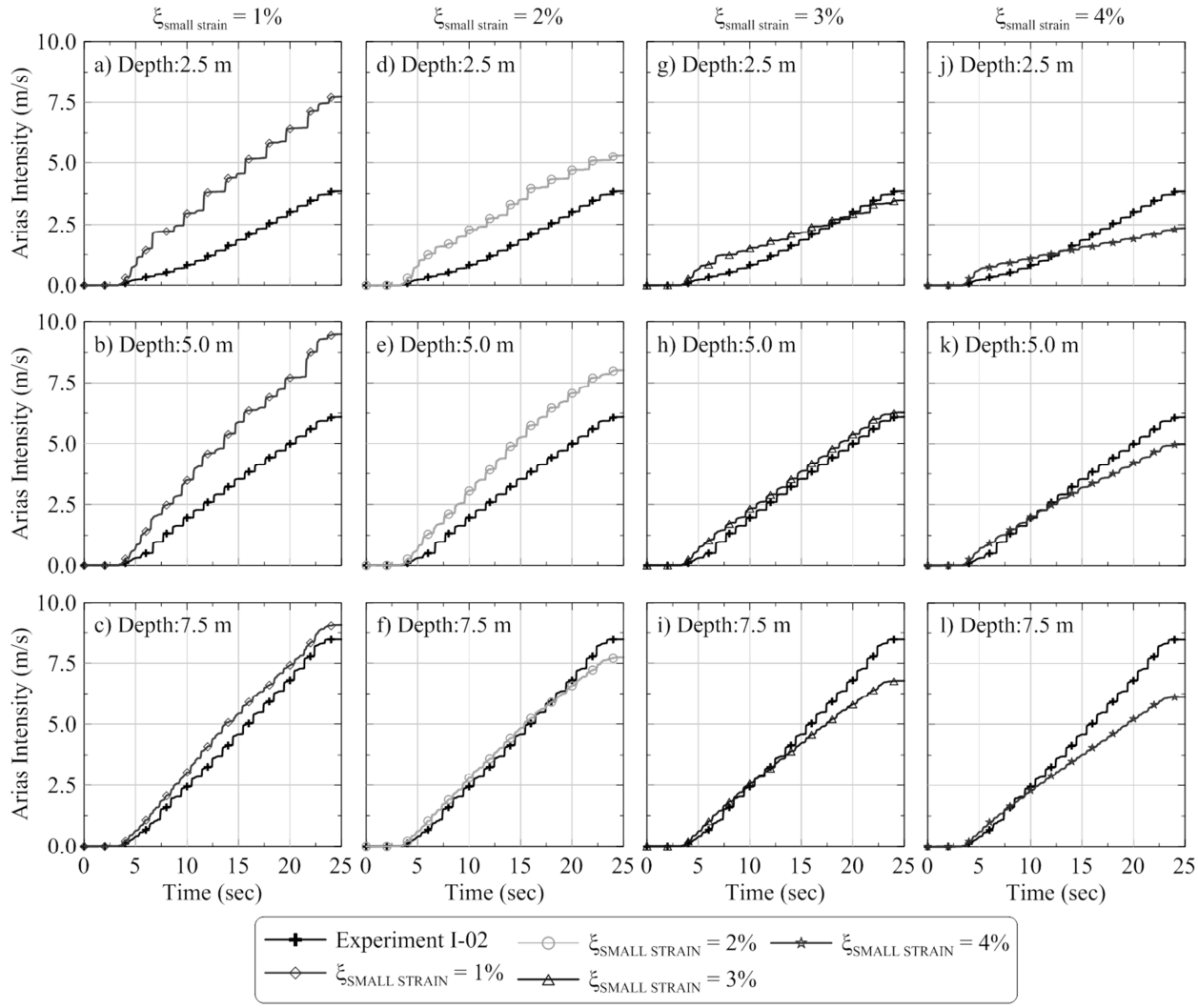

Figure 3-17: Comparison of Arias intensity time history for numerical simulations for calibrated models using different viscous damping values and centrifuge experiment I-02.

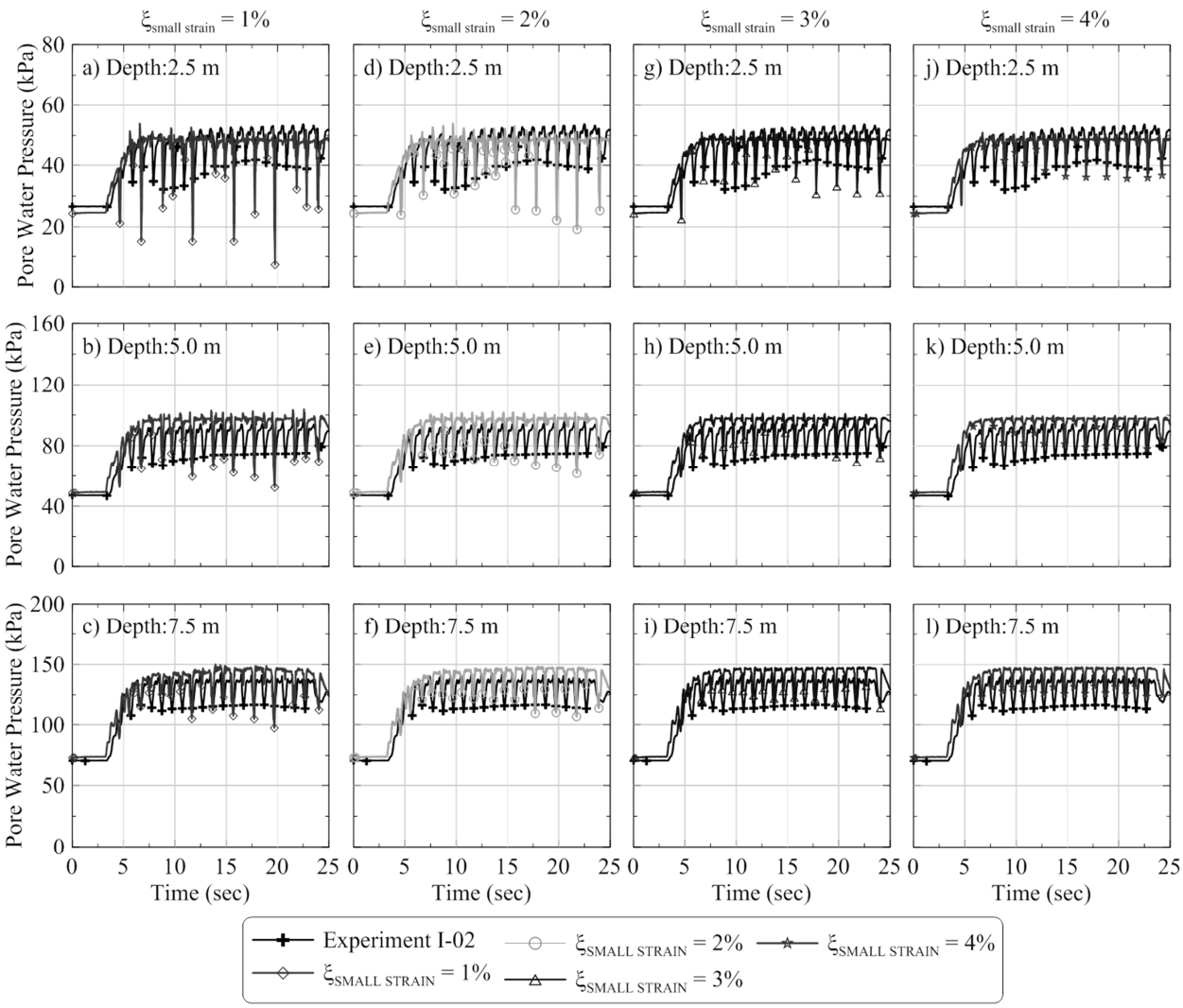

Figure 3-18: Comparison of pore water pressure time history for numerical simulations for calibrated models using different viscous damping values and centrifuge experiment I-02.

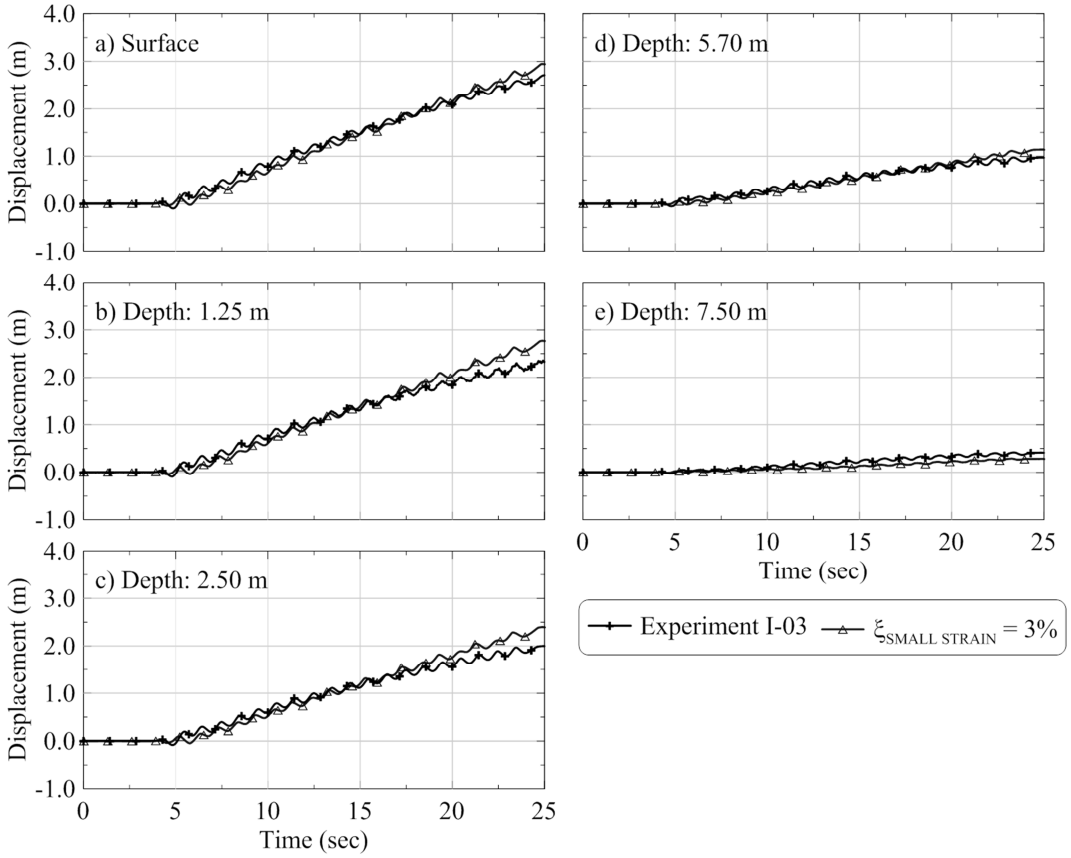

Figure 3-19: Comparison of boundary displacements for numerical simulations for calibrated models using 3% viscous damping values and centrifuge experiment I-03.

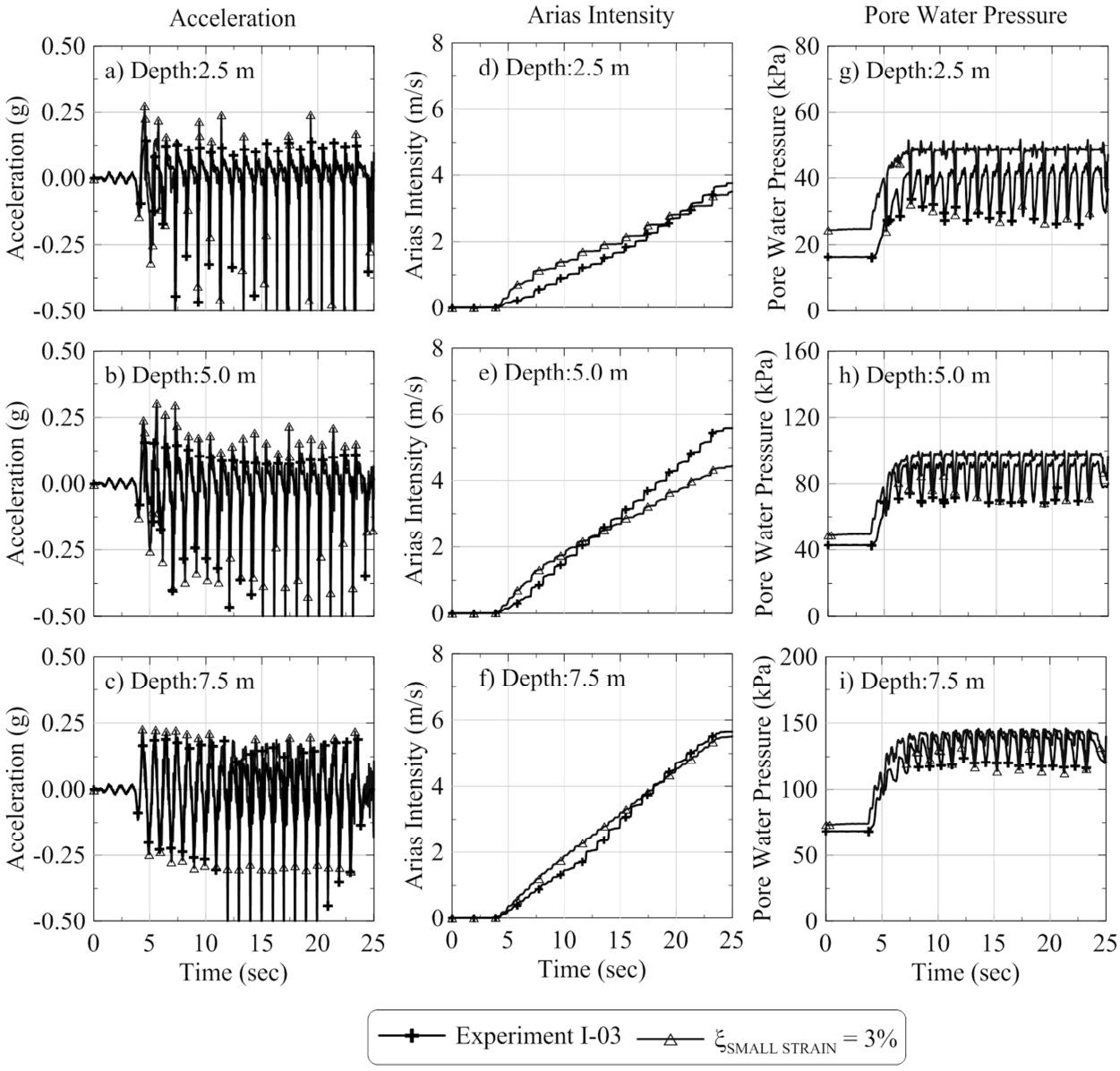

Figure 3-20: Comparison of acceleration, Arias intensity and pore water pressure time histories for numerical simulations for calibrated models using 3% viscous damping values and centrifuge experiment I-03.

CHAPTER 4 - NUMERICAL MODELING OF LIQUEFACTION-INDUCED LATERAL SPREADING LOADS AGAINST LARGE DIMENSION, RIGID FOUNDATIONS

4.1 Introduction

Population growth, especially in urban regions, has led to the need for larger bridges with increasing spans and traffic volumes. These bridges impose greater foundation loads, including static and seismic lateral forces, which in turn requires the use of large, rigid foundations such as large diameter drilled shaft groups; large, closely spaced driven pile groups; or large-dimension dredged caissons.

Figure 4-1a show a schematic of typical bridge foundation layout adjacent to a river bank. During seismic shaking, the river banks (which typically include layers of relatively recently-deposited sands) can liquefy and spread laterally. The displacements associated with lateral spreads can induce additional horizontal loads on the bridge foundation which in many lead to overturning failures and extensive structural damage to the foundation elements (Figure 4-1b). Although it is possible to estimate if lateral spreads will occur for a given earthquake and soil conditions, the design of pile foundations requires an evaluation lateral spreading-induced earth pressures. During the past century, several case histories of damage to pile foundations caused by liquefaction-induced lateral spreading have corroborated the importance accounting for lateral spreading-induced forces. Tables and Figures

Table 4-1 presents relevant case histories of bridge foundations heavily damage by lateral spreads.

Studies of soil-foundation interaction involving lateral spreads are typically limited to single flexible piles or small pile groups. Table 4-2 lists some key soil-foundation interaction studies involving lateral spreads.

Two different approaches to the design of flexible piles in liquefiable soils are currently used for design (Puri and Prakash, 2008). The first approach, force or limit equilibrium analysis, computes the lateral soil pressure distribution along the pile foundation (Figure 4-2a) which is then used to compute pile displacements and bending moments. The second method, displacement p-y analysis, represents the interaction of the pile and the liquefying soil by means

of a series of non-linear springs (Figure 4-2b), based on either the soft clay model (Matlock, 1970) or a sand model [generally API (1987)] with a p-multiplier to reduce the resistance of the liquefied soil, which typically vary from about 0.03 to 0.3. The ultimate soil resistance typically is limited by the drained passive pressure, although investigators disagree over what ultimate value should be used, with values varying from about 3 to 12 times the shear strength mobilized during failure (Boulanger et al., 2003).

A number of studies (Kawakami, 1996; Ohtomo, 1996; Liu et al., 1998; Mageau and Stauffer, 1998; Soydemir et al., 1998; Chang et al., 2001) have examined the effect of seismic loading (with or without lateral spreads) on large, rigid foundations. The studies suggested highly variable lateral spreading loads, thus limiting their application in engineering practice.

This paper presents the calculation of the lateral pressures exerted by lateral spreads on large, rigid foundations by means of numerical simulations. The numerical models were calibrated and evaluated using global displacements, accelerations, and pore water pressures recorded in four centrifuge tests using harmonic excitation. The calibration process highlights the importance of the soil-foundation interface. The calibrated numerical models were then used to simulate lateral spreading-induced pressures with broadband seismic input motions and more realistic soil permeability. Soil pressures extracted from these numerical analyses were used to determine pressure profiles and bending moments along the caisson and were compared with available analysis methods.

4.2 Centrifuge experiments of free field lateral spreading

Four lateral spreading centrifuge tests were constructed and performed at Rensselaer Polytechnic Institute (RPI) centrifuge facility in Troy, New York using a laminar box to allow for large unimpeded downslope soil displacements. The laminar box has internal dimensions of 71.0 cm long, 35.5 cm in plan and a maximum of 26.0 cm of height (35.5 m x 17.7 m x 13 m in prototype scale when spun at 50 g). The laminar box was inclined 2º to the horizontal using a stiff wedge at the base of the box. The rigid foundation element (simulating a large rigid caisson) used in these tests has exterior dimensions 10.0 cm long, 7.4 cm wide and 30.4 cm high (5.00 m x 3.7 m x 15.2 m in prototype scale spun at 50 g) and was constructed of thick-wall aluminum. The large rigid caisson was fixed to the base of the laminar box with bolts to provide a displacement and bending moment fixed connection. Tactile pressure pads were wrapped around

the caisson to measure lateral pressures, and covered with Teflon sheets to minimize the soil-caisson interface friction. The tactile pressure pad calibration and measurements is the subject of a forthcoming paper.

Instrumentation in these centrifuge models included pressure transducers and accelerometers to measure pore water pressure (PWP) and acceleration at numerous locations throughout the model, linear voltage differential transformers (LVDT) and lasers installed on the rings outside the laminar box to measure lateral displacement with depth, and subsurface sand grids and surface tracking markers to measure lateral displacement at discrete locations and depths. Figure 4-3 includes the instrument locations used in the two centrifuge experiments discussed here.

One of the lateral spreading centrifuge experiments with a large rigid caisson (experiment IA-3) was used to calibrate the soil-caisson interface. This centrifuge test was subjected to a sinusoidal input acceleration motion with a prototype frequency of 1 Hz and peak ground acceleration of 0.24 g (Figure 4-4a). Three other tests (experiments IA-2, IA-4 and IA-5) were used to evaluate the ability of the calibrated model to compute the response of a similar model subject to a different input motion. The input motions for experiments IA-2, IA-4 and IA-5 had the same frequency (1 Hz) as experiment IA-3 but lower peak ground acceleration (0.21g, 0.20 g and 0.22g) (Figure 4-4b, c and d, respectively). The soil profile for all four tests consisted of loose Nevada sand with a prototype thickness of 10m underlain by 2m of dense, lightly cemented sand (Figure 4-3).

4.3 Numerical simulation approach

The numerical simulations presented in this paper were performed using the finite element framework OpenSees (Mazzoni et al., 2006). This numerical framework employs a two-phase fully-coupled finite element formulation (Parra, 1996; Yang and Elgamal, 2002) based on Biot's theory (Biot, 1962). In this framework, the saturated soil is modeled as a two-phase material implementing the u-p formulation (Chan, 1988) for two- and three-dimensional analyses. In the u-p formulation, the displacement of the soil skeleton (u) and pore water pressure (p) are the primary unknowns. Although currently available soil finite elements in the OpenSees framework do not implement a Total Langragian formulation to calculate large strains,

the application to numerically simulate lateral spreading problems has been successful (Yang 2000, Elgamal et al. 2002, 2003, and Elgamal et al. (2005). The simulated soil profile was inclined at 2º in prototype scale is modeled as proposed by Lu et al. (2010). This assumption better represents the stress field and the inertial conditions of the experiment than the alternative proposed by Taboada (1995), who suggested that a 2º inclination at model scale should be modeled as a 4 to 5º ground surface inclination in prototype scale.

4.3.1 Constitutive modeling of soil behavior

The behavior of soils experiencing lateral spreading was modeled using the pressure-dependent soil constitutive model proposed by (Parra, 1996; Yang, 2000; Yang and Elgamal, 2002). The term pressure-dependent for this soil constitutive model refers to the change of the shear strength and stiffness with effective mean stress. For clarity, we refer to the constitutive model as an effective stress constitutive model. This effective stress constitutive model was developed based on the original framework proposed by Prevost (1985) and focused on simulating the liquefaction-induced shear strain accumulation mechanism (Yang and Elgamal, 2002; Elgamal et al., 2003) and the deviatoric-volumetric strain coupling, i.e., dilatancy, during cyclic loading. The main parameters of the model include standard dynamic soil properties such as small-strain shear modulus and friction angle, as well as parameters to control dilatancy (i.e., phase transformation angle, contraction parameter c_1, and dilation parameters d_1 and d_2) and the parameters controlling liquefaction-induced, perfectly-plastic shear strain accumulation. The numerical models developed for this paper use the values of friction angle, permeability and G_0 determined for Nevada Sand as part of the experiments developed in the Verification of Liquefaction Analysis by Centrifuge Studies (VELACS) geotechnical investigation program and the value of phase transformation angle suggested by Elgamal et al. (2002) for Nevada sand with relative density (Dr) between 35 to 45% (which are close to the Dr values of 30 to 35% used in the centrifuge experiments). Calibration of the dilation parameters and the viscous damping used in this study was presented by Phillips et al. (2012). The permeability used in the simulations (Table 4-3) corresponds to the scaled value for a centrifuge test at 50 g using Nevada sand with water as the pore fluid; in prototype scale the permeability is 50 times the permeability of Nevada Sand measured in laboratory tests . A numerical model developed in OpenSees using the aforementioned soil constitutive model was able to reproduce the behavior observed in free-field centrifuge tests for the same Nevada sand soil profile as experiments IA-2, IA-3, IA-4 and IA-5

(Phillips et al., 2012). The three-dimensional (3D) numerical model has 2680 nodes (each node with 4 degrees of freedom) and 2133 BrickUP elements (Figure 4-5).

4.3.2 Soil-caisson interface

The development of numerical models to represent the behavior observed in laboratory (small-scale and full-scale) and in-situ tests requires replicating the boundary conditions at the soil-caisson contact. Different alternatives have been utilized in the past, such as: (1) equal degree of freedom between caisson and soil nodes to model a very rough soil-caisson interface (Zhang et al., 2000); (2) a 3D contact formulation that transmits tension to the soil matrix and shear stresses to the caisson (Lam et al., 2009); and (3) a soil-caisson connection using a series of non-linear limited compression connectors for 2D analyses (Brandeberg and Boulanger, 2004) with a reduction factor that depends on the excess pore water pressure ratio, $r_u = \Delta u/\sigma'_{vo}$ (where Δu is the excess pore water pressure and σ'_{v0} is the initial effective vertical stress). These types of interface alternatives are either not suitable to represent a soil-caisson interface with a low friction angle (alternative 1), not available for public use in the current version of OpenSees (alternative 2) or only implemented for 2D numerical simulations (alternative 3). Therefore, we explored other possible connection schemes to model the soil-caisson interface. The following interface alternatives were implemented and tested to model the soil-caisson interface in the 3D finite element models developed in OpenSees.

1. Tension-compression interface that is capable of transmitting tensile and compressive normal forces. The force of this connector is not limited (Figure 4-5c). The slope of the force-displacement curve for the tension-compression interface was taken as the slope of the p-y curve for the API (1987) sand model.
2. Compression-only interface that transmits only compressive forces between the caisson and the soil elements (Figure 4-5d). The compressive force transmitted at the interface is not limited. The slope of the force-displacement curve for the compression-only interface was taken as the slope of the p-y curve for the API (1987)sand model.

3. Compression-limited interface that transmits only limited compressive forces (Figure 4-5e). The slope of the force-displacement curve for the compression-limited interface was taken as the slope of the p-y curve for the API (1987) sand model. The limiting force was assumed to be pressure-dependent, similar to the liquefied strength ratio concept (Olson and Stark 2002), with an initial estimate of the maximum pressure based on the Boulanger et al. (2003) recommendation of $N_P Sb$, where N_p is the lateral-bearing factor, S is the mobilized shear resistance of the liquefied soil, and b the caisson width. However this limiting pressure resulted in an underestimation of the centrifuge displacements. Therefore the limiting pressure at different depths was then modified iteratively to better replicate the boundary displacement measurements of centrifuge experiment IA-3. Figure 4-6 compares the limiting pressure proposed by Ashford et al. (2011) with the limiting pressure distribution back-calculated from the centrifuge test displacements. The use of a constant limiting pressure proposed by Ashford et al. (2011) significantly overestimated the displacements measured in the centrifuge test.

4.4 Evaluation of soil-caisson interface modeling schemes

Numerical models using the three alternatives to represent the soil-caisson interface were developed and compared with the experiment IA-3 measurements. Figure 4-7 compares the simulated and boundary lateral displacements. The numerical simulations using the tension-compression interface systematically underestimated the boundary displacements measured in experiment IA-3, regardless of the assumed interface stiffness. When the compression-only interface was used, the displacement increased compared to the tension-compression interface; however, the computed displacements were lower than the measured values. The numerical model using a compression-limited interface yielded boundary displacements that reasonably match centrifuge experiment IA-3. This result was expected because the limiting force with depth for this interface was calibrated to replicate the measured displacements.

Figure 4-8 compares the results of the numerical simulation and the centrifuge experiment IA-3 in terms of accelerations for a time window corresponding to 10 to 15 seconds. The differences of the computed acceleration time histories using different connection schemes to simulate the soil-caisson interface are only significant for locations close to the caisson – locations 3 and 6– where abrupt changes in the acceleration record are observed for the models implementing tension-compression or compression-only connectors. The numerical model using the compression-limited interface provides the best match to the measured behavior. The acceleration time histories computed by the numerical simulations are in phase with the centrifuge records at the different locations (in plan and depth). Larger upslope acceleration spikes are present in the centrifuge test records than in the numerical simulation results, consistent with the results of the numerical simulation of a free-field lateral spreading centrifuge test (Phillips et al., 2012) used to calibrate the soil constitutive model used in this study.

Comparing acceleration records using only the peak values can be cumbersome and potentially misleading. The use of energy-based parameters, such as Arias Intensity, provides an alternative comparative measure. The Arias intensity was calculated for each acceleration time history (numerical simulation result and centrifuge measurement) as follows.

$$Arias\ Intensity = \frac{\pi}{2g}\int_0^{Td} a(t)^2 dt \qquad (4\text{-}1)$$

where g is the acceleration of gravity, T_d is the duration of the motion and $a(t)$ is the acceleration time history.

Figure 4-9 compares the results of using the three different interface schemes in terms of Arias intensity. The numerical model with the compression-limited interface best matched the measured Arias intensities at the free field locations (Figure 4-9a to Figure 4-9c) compared with the other two other implemented interfaces. For points located close to the upslope caisson face (Location 3; Figure 4-9d to Figure 4-9f), the compression-limited interface slightly underestimated the measured Arias intensities; while the other two interface types replicated almost exactly the measured Arias intensity time histories. The tension-compression interface overestimated the Arias intensity for points located close to the downslope caisson face

(Location 6) at depths 2.5 m and 5.0 m (Figure 4-9j and Figure 4-9k), while the compression-only and compression-limited interfaces provided almost the same Arias intensity.

Figure 4-10 compares simulated and measured pore water pressures. The simulated porewater pressures more closely resembled the measured values in the free-field conditions (Location 1; Figure 4-10a to Figure 4-10c) than at locations proximate to the caisson. The differences between the simulation results with different connection schemes to represent the soil-caisson interface are important at locations close to the upslope and downslope sides of the caisson, locations 3 and 6 respectively. Pore water pressure time histories calculated at the upslope side (Figure 4-10d to Figure 4-10f) of the caisson using the tension-compression connection scheme are out of phase with the centrifuge measurements. At this same location the numerical model using the compression-only connection computes larger downward pore water pressure spikes than the centrifuge recording, particularly for a depth of 2.5 m (Figure 4-10d). The numerical model using the compression-limited connection reasonably matches the magnitude of the downward pore water pressure spikes measured in the centrifuge test. For the downslope caisson face, the model using the tension-compression connection computes a downward pore water pressure spike at the depth 2.5 m that is much larger than measured in the centrifuge test (Figure 4-10j).

Four indexes were used to qualitatively compare the results of the numerical models with different soil-caisson interfaces and the centrifuge test measurements: the final global displacement at the end of shaking, the final Arias intensity at the end of shaking, and two pore water pressure indices. The first porewater pressure index (PWP 1) was calculated by subtracting the initial PWP from the minimum excess PWP for all time steps after 5 seconds (when liquefaction occurred). The second index (PWP 2) is calculated by subtracting the initial PWP from the maximum excess PWP.

The concordance correlation coefficient (CCC) proposed by Lin (1989) was used to evaluate the agreement between the numerical simulations and the centrifuge indexes.

Table 4-4 presents the CCC values for the four indices. The numerical model with a soil-caisson compression limited interface provided the highest CCC values and best replicated the displacements, accelerations, and pore water pressures measured in experiment IA-3.

For each numerical simulation, the soil pressure distribution was calculated at the upslope and downslope faces of the caisson using the stresses and PWP extracted for the Gaussian points and nodes close to the faces of the caisson. Figure 4-11 presents the upslope and downslope pressure distributions at the time when the maximum bending moment at the base of the caisson is reached. The results were compared with closed-form solutions for drained Rankine passive and active conditions (assuming $\phi' = 31.4^{o}$ as suggested by Elgamal et al. (2002), undrained Rankine passive and active conditions (assuming a liquefied shear strength proportional to the initial effective vertical stress, $s_u(liq) = 0.09 \times \sigma'_{v0}$, as suggested by Olson and Johnson (2008) for soils with Dr values similar to centrifuge experiments), and an $r_u=1$ condition (which corresponds to the total vertical stress). Comparisons using closed-form solutions for the undrained Rankine passive condition also were developed using a yield shear strength ratio (Olson and Stark 2003) and a residual undrained strength (Seed and Harder, 1990), but these solutions did not provide additional insights to the analyses and therefore were not included in the figures.

The results showed very high pressures in the upslope caisson face for the tension-compression and the compression-only interface schemes; values even higher than the drained Rankine passive pressures for the upper half of the soil profile. The compression-limited interface yielded pressures that were higher than the undrained Rankine passive distribution but lower than the passive drained condition.

For the lower half of the model the three types of interfaces yielded similar pressures on the upslope caisson face. The differences between the tension-compression and the compression-only interfaces for the upper half of the soil profile are a result of the unreasonable forces developed in the interface elements. Lower pressures were computed for the upslope caisson face when the compression-limited interface scheme was used because this interface can only transfer compressive forces until a certain limit is reached. For the downslope caisson face, the compression-only and compression-limited interface schemes yielded similar results. Using a tension-compression interface introduced tension in the soil reducing the effective stress and inducing unrealistically large downward PWP spike in the soil close to the surface (Figure 4-10d).

Based on these comparisons, the compression-limited interface was used for the simulations described in the following sections.

4.5 Simulations of centrifuge tests with caisson element and different input motions

Numerical simulations of experiments I-A2, I-A4 and I-A5 were conducted using the numerical model with the compression-limited interface to simulate the soil-caisson interface. The input motions for these centrifuge experiments had a lower acceleration than I-A3. Lateral displacement, acceleration and pore water pressure time histories were extracted from the four numerical simulations from locations corresponding to the centrifuge instrument locations. The four indices described previously (permanent displacement at the end of shaking, Arias intensity at the end of shaking, and the two PWP indices) were used to compare the simulations to the measurements.

Figure 4-12a compares the computed and measured lateral displacements at the end of shaking. Although the numerical simulations consistently yielded lower lateral displacements (in particular for experiment I-A4) than the centrifuge test measurements (with the exception of the experiment I-A3) the differences are considered minor, and a high CCC value (CCC = 0.89) was obtained for this index. Figure 4-12b compares the simulated and measured Arias intensities. Larger Arias intensities were calculated for the acceleration time histories recorded in experiment I-A3 compared with the other three centrifuge test. These large Arias intensity values resulted from more pronounced upslope acceleration spikes, and the size of these spikes was not fully captured, resulting in lower Arias intensity values. Although a lower CCC value is obtained for Arias intensity (CCC = 0.72), the match was considered satisfactory.

Figure 4-13 compares the simulated and measured PWP indices. The results show that the model reasonably captured the downward PWP peaks (CCC=0.92) as well as the maximum excess PWP (CCC=0.96). A high CCC for the maximum PWP was expected because the excess PWP reaches a maximum when the soil liquefies (r_u=1); however, the model also captured the downward PWP spikes which differ at each instrument location. Reproducing the PWP is fundamental to estimating the effective vertical stresses and the soil shear strength at a given time. Overall it can be stated that the developed numerical models are able to reproduce

reasonably well the boundary displacement, acceleration and PWP time histories recorded in the four different centrifuge tests.

4.5.1 Pressure distribution for centrifuge tests simulations

Earth pressure distributions at the time when the maximum bending moment at the base of the 10-m deep caisson is reached are calculated for centrifuge experiments IA-2, IA-4 and IA-5 following the same procedure described for experiment IA-3. Figure 4-14 presents the PWP distribution at the upslope and downslope faces of the caisson at the time frame corresponding to the maximum bending moment at the base of the caisson (t = 19.73 sec). The simulated PWP profiles are compared with the centrifuge test measurements at locations 3 and 6 (upslope and downslope respectively) as well as the hydrostatic and $r_u = 1$ distributions. Figure 4-15 presents the earth pressure distribution at the time of the maximum bending moment at the base of the caisson for the upslope and downslope faces of the caisson for the numerical simulation of the four centrifuge experiments. The total pressures on the upslope face of the caisson vary between the drained and undrained passive conditions; suggesting that the numerically-modeled soil is not in an undrained condition during shaking and lateral spreading. This result is consistent with the negative r_u values (PWP lower that the hydrostatic values) observed for the upper 2 m of the soil profile. Porewater pressure ratios for upslope face of the caisson range from 0.5 to 0.7 during the transient downward spikes for depths below 2m.

The total pressures on the downslope face of the caisson match the undrained active pressure distribution, which is reasonable considering that lateral spreading is moving the soil away from the caisson. However, in contrast to the upslope face, this result suggests that the soil adjacent to the downslope face is undrained during shaking and lateral spreading.

4.5.2 Evaluation of earth pressures using strain wedge method

The strain wedge method (Ashour et al., 1998) provides a link between the stress-strain-strength behavior of the soil in the passive wedge and the earth pressure distribution (load) for a vertical column. The SWM is based on the mobilized passive wedge in front of the caisson (Figure 4-16) which is characterized by a base angle, βm; the passive wedge depth, h; and the spread of the wedge via the fan angle, $\phi_{equivalent}$ (an equivalent friction angle). The horizontal stress change at the passive wedge face, $\Delta\sigma_h$, and side shear, τ, act as shown in Figure 4-16.

As mentioned before, the SWM requires estimating $\phi_{equivalent}$ to determine the size of the passive wedge for computation. Based on surface tracking measurements and high speed videos of the centrifuge testing it was possible to determine the size of the passive wedge and back-calculate an average $\phi_{equivalent}$ = 17º. A similar exercise was performed using the computed displacements in the numerical simulations. The numerical simulations yielded an average $\phi_{equivalent}$ = 15°. However, to maintain consistency with the centrifuge measurements, we employed $\phi_{equivalent}$ = 17° in our SWM calculations. We calculated SWM lateral pressures for both undrained and drained conditions. The undrained analyses were conducted using an undrained shear strength ratio, s_u/σ'_{vo} = 0.09 following the recommendations of Olson and Johnson (2008) for sands with Dr ~ 30 - 35%. The undrained analyses were conducted for a constant r_u = 0.6.

Figure 4-17 compares the earth pressure profiles for the numerical simulations of the four centrifuge tests with the pressure distributions computed using the SWM. The partially drained and undrained SWM earth pressure profiles provide approximate upper and lower bounds for the simulated pressures, respectively.

4.5.3 Evaluation of earth pressures using equivalent triangular pressure distribution

The Japanese Road Association (JRA, 2002) proposed a simplified triangular lateral pressure profile to represent the net pressure against a pile during lateral spreading (Figure 4-18). The net pressure (p) is calculated as:

$$p = K\gamma_t z \tag{4-2}$$

where γ_t is total unit weight, z is depth, and K is the net pressure coefficient equal to 0.3.

He et al. (2009) used this method and back-calculated an average triangular net pressure coefficient ranging from 1.00 to 1.23 for a series of large-scale experiments of lateral spreading pressures against piles of 2m and 5m length. The net pressure coefficient reported by He et al. (2009) is more than three times higher than the design recommendation of the Japanese Road Association (JRA, 2002); however, based on an analysis of the Showa bridge failure (involving a 10-m long pile), He et al. (2009) recommended a reduction factor of 0.5 for their net pressure coefficient, i.e., K = 1.1 * 0.5 = 0.55.

Table 4-5 presents the equivalent triangular net pressure coefficients determined using the maximum moment at the base of the caisson obtained for each of the four numerical simulations of centrifuge tests (assuming a triangular net pressure distribution). The back-calculated triangular net pressure coefficients exhibited little variability (0.33 to 0.38), with an average value (K = 0.36) slightly larger than the JRA (2002) recommendation and about 1/3 of the value measured by He et al. (2009).

The numerical models of centrifuge test provide results that replicate the centrifuge measurements and reasonable pressure profiles against the caisson. Practical application of the aforementioned results requires considering more realistic input motions (broadband) and the use of the real permeability of the soil instead of the centrifuge scaled value (50 times greater). The following section presents the results of a parametric study using realistic permeability and input motions.

4.6 Numerical simulation with broadband input motions and representative soil permeability

To investigate the role of ground motion characteristics on the simulated lateral pressures, we performed simulations for the same soil profile using ten broadband motions. Table 4-6 presents the characteristics of the ten selected broadband input motions, and Figure 4-19 presents the acceleration response spectra. In addition, for these simulations, we restored the permeability of the soil to that of a fine sand ($k = 6.6 \times 10^{-3}$ cm/s). Total horizontal and PWP time histories and maximum moments at the base of the caisson were calculated for each simulation. The thickness of the liquefied layer was also calculated for each numerical simulation (Table 4-6).

Figure 4-20 presents the pressure distributions at the upslope and downslope face of the caisson calculated for the ten numerical simulations using broadband motions. The pressures on the downslope face of the caisson closely resemble the undrained active pressure distribution. Figure 4-20 also presents the result of curve fitting the maximum pressure values using a square root relationship with the confinement pressure for the upslope face of the caisson. For numerical simulations in which liquefaction occurs over the entire 10 m profile, larger total horizontal pressures were observed for upslope face for the top half of the soil profile. As illustrated in Figure 4-21, the simulations for motions 9 and 10 using fine sand permeability also yielded

larger total horizontal pressures for the top half of the soil profile compared to the pressures obtained in the centrifuge test simulations. Gonzalez et al (2009) observed a similar result – higher soil pressures at surficial layers– and attributed this result to the soil permeability. Gonzalez et al (2009) stated that the increase of the soil permeability during centrifuge testing allows the dissipation of the negative excess of PWP near the surface, thereby limiting soil dilation, and in turn, reducing the pressures imposed by the lateral spreading soil.

A simulation using broadband motion 10 and the centrifuge-scaled permeability was performed to determine if the reduction of the lateral spreading pressures against the caisson was a result of the change of permeability or a result of using a broadband input motion. This analysis yielded pressures for the first 5m of the profile on the upslope face of the caisson similar to the simulation conducted using the centrifuge test input motions with scaled permeability, potentially supporting the idea that permeability plays an important role on lateral spreading earth pressures.

4.6.1 Evaluation using strain wedge method

The calculated pressure distributions on the upslope face of the caisson were compared with the results of the SWM. Figure 4-22 compares the numerical simulations using broadband motions 5 and 9 (Figure 4-22a and Figure 4-22b respectively) with the pressures computed using the SWM. The SWM pressures were computed for a passive wedge depth equal to the depth of liquefaction, an equivalent friction angle of 17º, and an approximate PWP distribution from the numerical simulations.

The results in Figure 4-22a illustrate that the SWM reasonably envelopes the pressure distribution simulated for broadband motion 5 over the liquefied layer thickness. For broadband motion 9, the SWM also provides a reasonable approximation, although the SWM pressures are generally larger than the simulated pressures in the upper 7.5 m, and generally are smaller than the simulated pressures below 7.5 m.

4.6.2 Evaluation using equivalent triangular pressure distribution

Triangular net pressure coefficients were back-calculated for each numerical simulation using the maximum bending moment calculated at the base of the 10-m long caisson. These values are presented in Table 4-6, which also included the liquefied layer thickness, and Figure

4-23 presents these results graphically. As expected, the numerical simulations show an almost linear relationship between the Arias intensity and liquefied layer thickness (Figure 4-23a). The results also indicate an increase of the equivalent triangular pressure coefficient K calculated using the bending moment at the base of the 10-m long caisson with the increase of the thickness of the liquefied soil layer (Figure 4-23b).

The triangular net pressure coefficient calculated for cases in which the entire 10 m sand layer liquefied ranges from 0.56 and 0.60; significantly larger than the value determined for the centrifuge test simulations (K ~ 0.36) and almost identical to the reduced value recommended by He et al. (2009) for the Showa bridge case history. This increase on the triangular net pressure coefficient is explained by the increase of the pressures on the upslope of face of the caisson particularly for the upper half of the soil profile as presented in Figure 4-21.

Peak bending moments were computed along the length of the caisson, and these bending moments were used to estimate corresponding triangular net pressure coefficients. Figure 4-24 presents the triangular net pressure coefficient values back-calculated for the 10 different broadband input motions for different vertical locations (within the maximum depth of liquefaction). Figure 4-24 also includes: (1) the envelope of the triangular net pressure coefficients calculated for the ten numerical simulations; (2) the triangular net pressure coefficient distribution with depth assuming the curve fitting pressure distribution presented in Figure 4-20 on the upslope face of the caisson and the undrained active pressure distribution on the downslope of the caisson; and (3) the triangular net pressure coefficient profile for the case of the pressure distribution calculated using the SWM on the upslope face and undrained active pressure distribution in the downslope face. The back-calculated relationships for the triangular net pressure coefficient show an inverse relationship with the depth. This result implies that the secant slope for the net pressure distribution is larger for locations close to the surface and decreases with depth.

Compared to the He et al. (2009) recommendation, the first two back-calculated relationships provide higher triangular net pressure coefficients near the surface, similar values at 2m, and lower values (between 50% and 75% of the He et al. 2009 recommendation) below 2m.. Again, compared to He et al. (2009), the SWM (with an undrained active pressure condition on the downslope face) yielded larger triangular pressure coefficients in the upper 8 m and close to

75% of the He et al. (2009) value below 8 m. Although the triangular net pressure coefficients determined by the back-calculated relationships seem relatively small at the bottom of the profile when compared with the recommendation of He et al. (2009) it should be noted that are very close to the He et al. (2009) reduced value for the Showa bridge case history for a 10 m long pile.

Both the back-calculated relationships and the triangular net pressure coefficients calculated directly from the numerical simulations using broadband motions yielded values higher than the JRA (2002) recommendation.

4.6.3 Net pressures

Figure 4-25 presents the net pressures (the difference between the upslope and downslope pressure profiles) computed for numerical simulations using broadband input motions 7 to 10. An approximate envelope of the simulated net pressures suggests that the earth pressure at the surface is approximately zero and increases proportional to the square root of depth. Figure 4-25 includes the recommended net pressure profiles from Ubilla et al. (2011), He et al. 2011 and JRA (2002). The simulated net pressures are roughly bounded by the JRA (2002) and He et al. (2009) recommendations. The constant net pressure of 30 kPa recommended by Ubilla et al. (2011) is inconsistent with the simulations.

4.7 Tables and Figures

Table 4-1: Most relevant case histories of bridge foundation heavily damaged by lateral spreads.

Bridge	Earthquake	Country	Reference
Salinas River Bridge	San Francisco, 1906	USA	Youd and Hoose (1978)
Banyu Bridge	Kanto, 1923	Japan	Hamada and O'Rourke (1992)
Showa Bridge	Niigata, 1964	Japan	Hamada and O'Rourke (1992)
Resurrection River	Alaska, 1964	USA	Ross et al,. (1973)
Liao River Bridge	Haicheng, 1975	China	Shengcong and Tatsuoka (1984)
Shen Li Bridge	Tangshan, 1976	China	Shengcong and Tatsuoka (1984)
Magsaysay Bridge	Luzon, 1990	Philippines	Hamada and O'Rourke (1992)
Rio Banano Bridge	Costa Rica, 1991	Costa Rica	Beavers (1991)
Nishinomiya-Ko	Hyogoken-Nambu, 1995	Japan	Japanese Geotechnical Society (1996)
Llacolén bridge	Maule, 2010	Chile	GEER (2010)

Table 4-2: Brief list of recent studies of lateral spreading effects on pile foundations.

Semi-empirical & theoretical approaches	Chen & Poulos (1997); Wang & Reese (1998); PoLam et al. (1998); Goh & O'Rourke (1999); Pan et al. (2002); Ashour and Norris (2003)
Centrifuge studies	Wilson et al. (2000); Dobry et al. (2003); Abdoun et al. (2003); Boulanger et al. (2003); Brandenberg et al. (2005)
Shaking table/physical tests	Tokida et al. (1993); Ohtomo (1996); Kawakami (1996); Cubrinovski et al. (2006); Dungca et al. (2006); Harada et al. (2006)
Field cases & tests	Berrill et al. (1997); Brown & Camp (2002); Ashford et al., (2001); Ashford et al. (2004); Rollins et al. (2005); Weaver et al. (2005)

Table 4-3: Effective stress Yang (2000) constitutive model parameters for Nevada Sand (Dr = 35-45%).

Variable	Value	Units
Mass density	1980	kg/m^3
Ref. shear modulus	33000	kPa
Ref. mean confinement	80	kPa
Confinement dependence coeff.	0.5	---
Friction angle	31.4	°
Peak shear strain	10	%
Number of Yield surfaces	20	---
Phase transformation angle	26.5	°
Contraction parameter, c_1	Overburden pressure dependent (Phillips et al., 2012)	---
Dilation parameter 1, d_1	Overburden pressure dependent (Phillips et al., 2012)	---
Dilation parameter 2, d_2	Overburden pressure dependent (Phillips et al., 2012)	---
Liquefaction parameter (γ_y)	0.01	---
Permeability coefficient	0.0033	m/s

Table 4-4: CCC values calculated for the numerical simulations using different soil-caisson interfaces.

Interface Type	Displacement	Arias Intensity	PWP 1	PWP 2
Compression-Tension Interface	0.70	0.27	0.91	0.95
Compression only interface	0.81	0.54	0.87	0.95
Compression limited interface	0.85	0.74	0.92	0.96

Table 4-5: Back-calculated equivalent triangular distribution (K) at the base of the caisson (depth= 10 m).

Centrifuge test numerical simulation	Arias Intensity (m/s)	a_{max} (g)	K
Experiment I-A2	3.51	0.21	0.38
Experiment I-A3	5.25	0.24	0.38
Experiment I-A4	3.03	0.20	0.33
Experiment I-A5	3.42	0.22	0.36

Table 4-6: Broadband input motion characteristics and results of numerical analyses for broadband motions.

	Arias Intensity (m/s)	Significant Duration* (sec)	a_{max} (g)	Thickness of liquefied soil layer (m)	K (triangular distribution)	Surface Displacement at maximum moment (m)
Motion 1	0.04	32.90	0.054	2.50	0.09	0.004
Motion 2	0.08	34.10	0.070	3.75	0.20	0.209
Motion 3	0.17	6.53	0.277	3.75	0.14	0.112
Motion 4	0.43	9.11	0.280	5.00	0.27	0.354
Motion 5	0.49	10.60	0.279	6.25	0.36	0.446
Motion 6	0.78	10.60	0.351	7.50	0.48	0.651
Motion 7	0.92	16.60	0.331	10.00	0.60	0.709
Motion 8	0.97	10.60	0.392	8.75	0.55	0.706
Motion 9	1.08	16.60	0.358	10.00	0.56	0.802
Motion 10	1.80	15.40	0.410	10.00	0.58	1.140

* Time interval between the points at which 5% and 95% of the Arias intensity

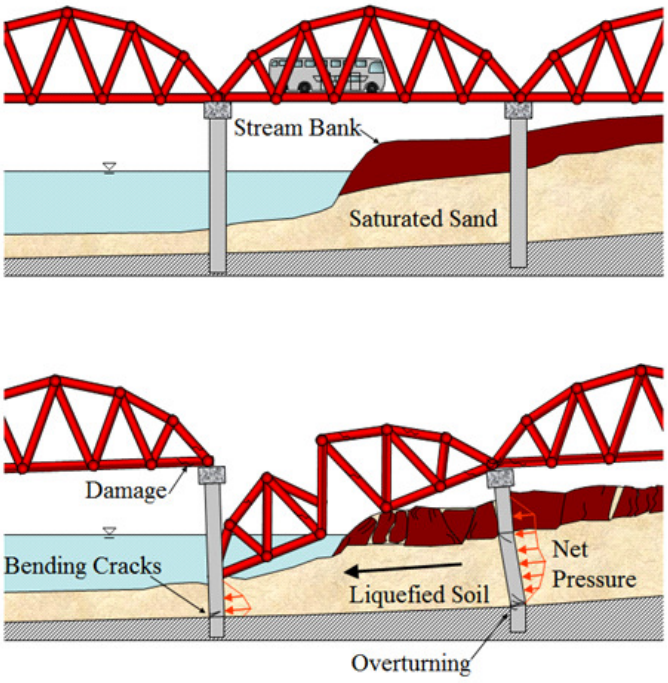

Figure 4-1: Schematic lateral spreading effects on bridge foundations. a) before the occurrence of lateral spreading. b) after the occurrence of lateral spreading.

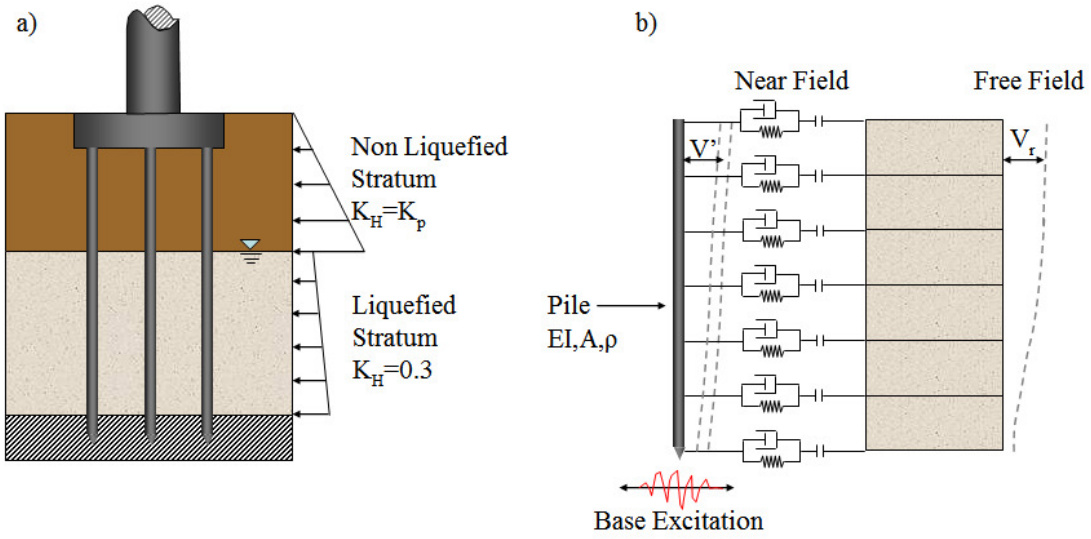

Figure 4-2: Schematic illustrating methods used to estimate the loads imposed by lateral spreads on flexible piles a) Force or limit equilibrium analysis method proposed by the Japanese Road Association (JRA 2002), b) displacement-based p-y analysis method.

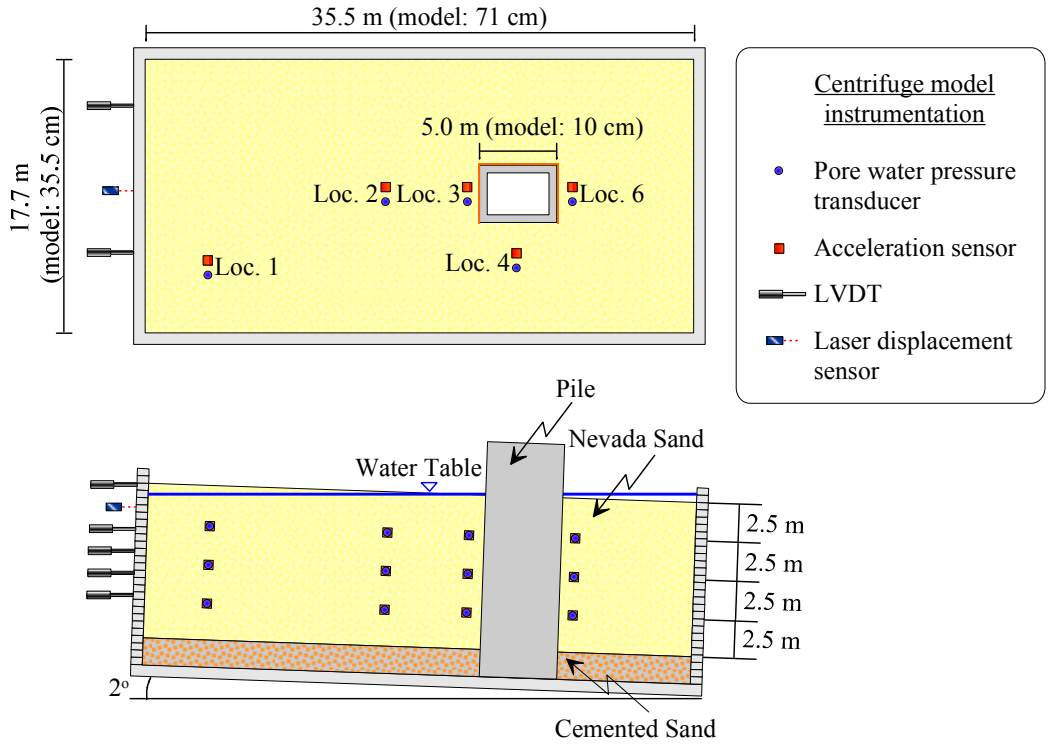

Figure 4-3: Schematic of centrifuge test configurations and instrument locations. Dimensions in prototype scale.

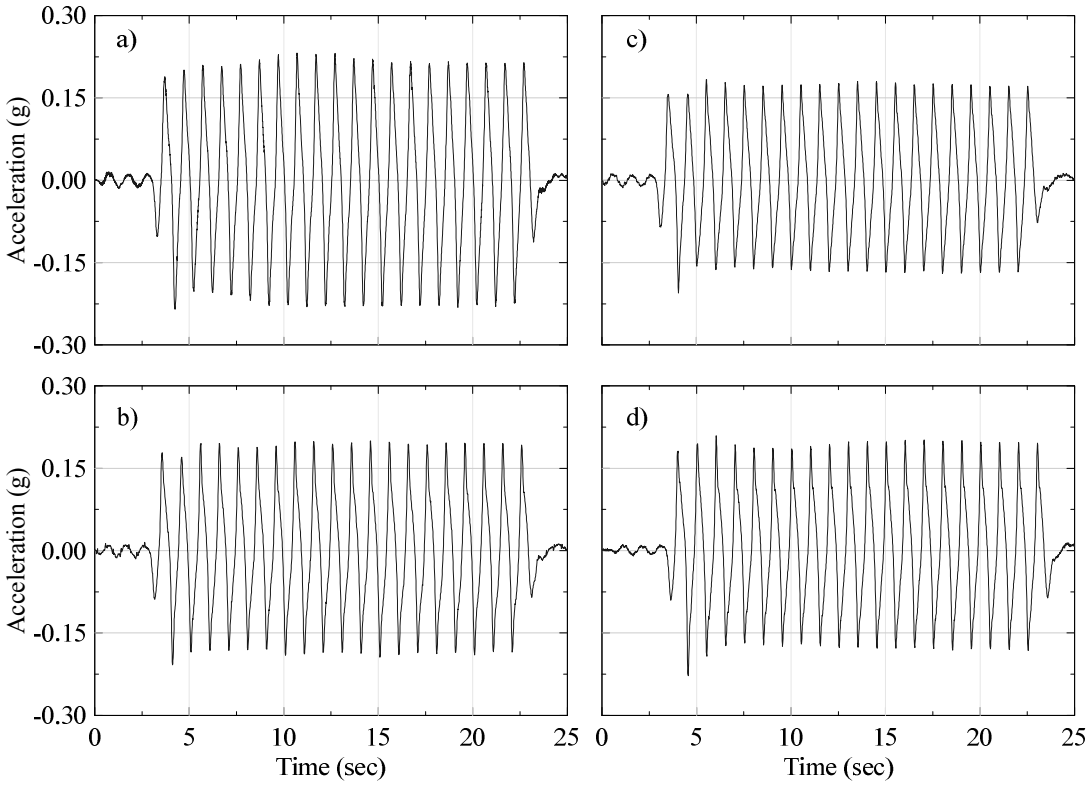

Figure 4-4: Input acceleration time histories applied at the model container base. (a) experiment IA-3; (b) experiment IA-2; (c) experiment IA-4; and (d) experiment IA-5.

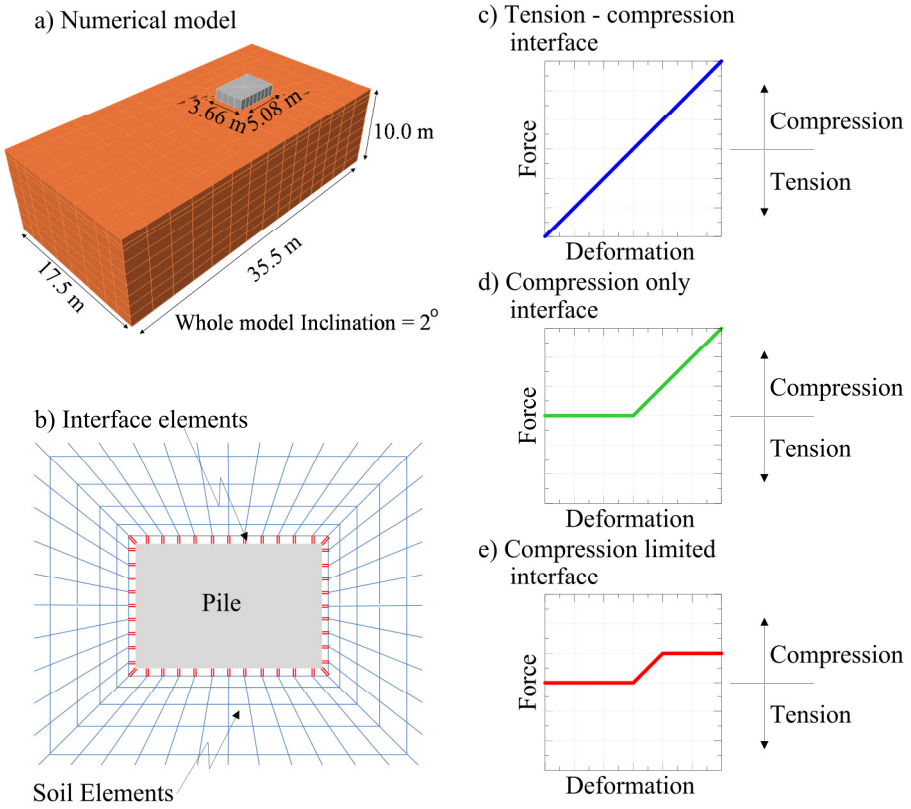

Figure 4-5: Schematic illustrations of: (a) 3D numerical model; (b) close-up of soil and interface elements proximate to the pile; (c) tension-compression interface; (d) compression-only interface; and (e) compression-limited interface.

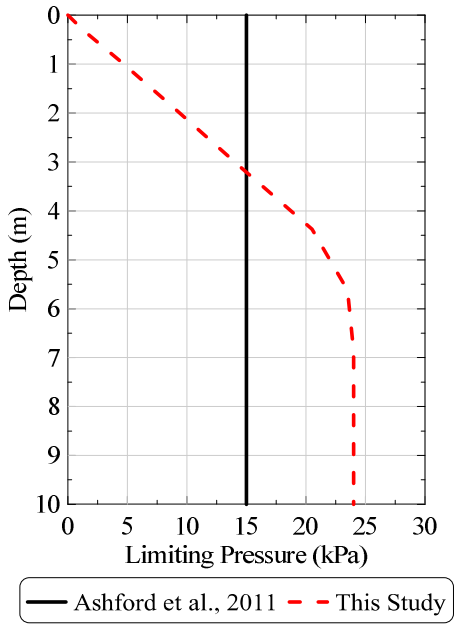

Figure 4-6: Comparison of limiting pressures used for soil-foundation interface elements.

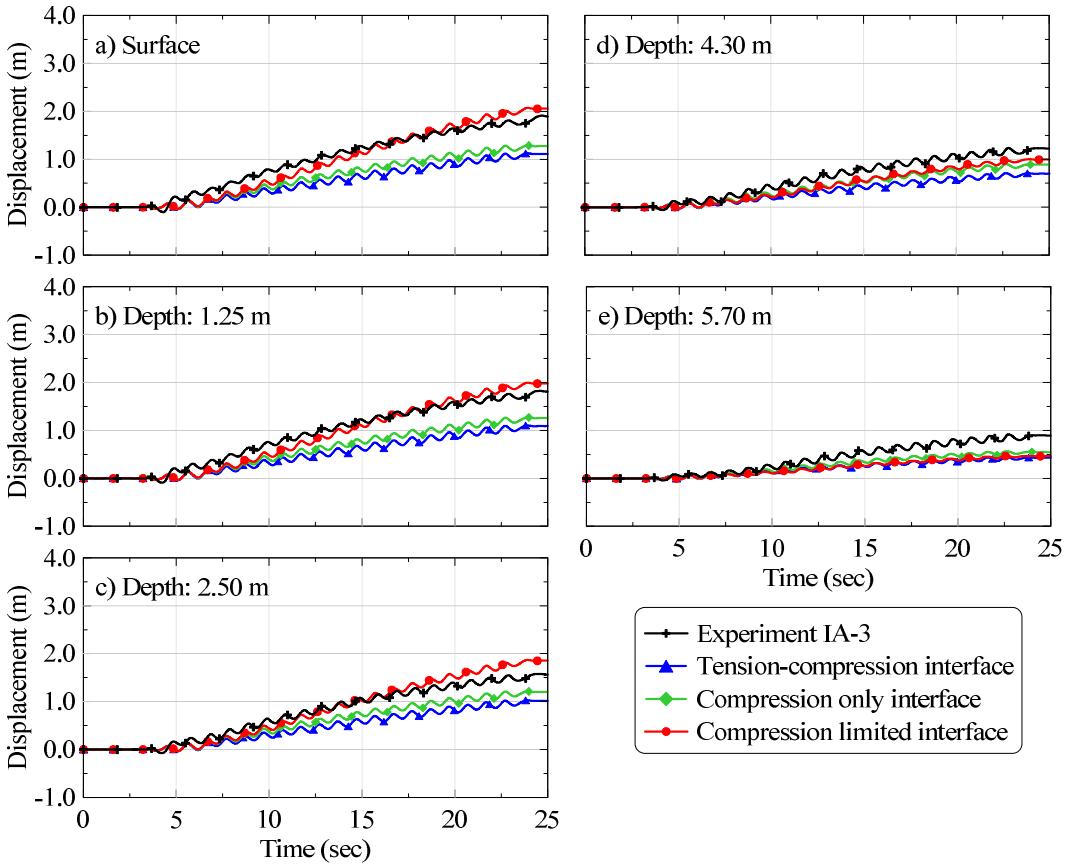

Figure 4-7: Comparison of global lateral displacements computed for numerical simulations using different soil-caisson interfaces with displacements measured during Experiment IA-3.

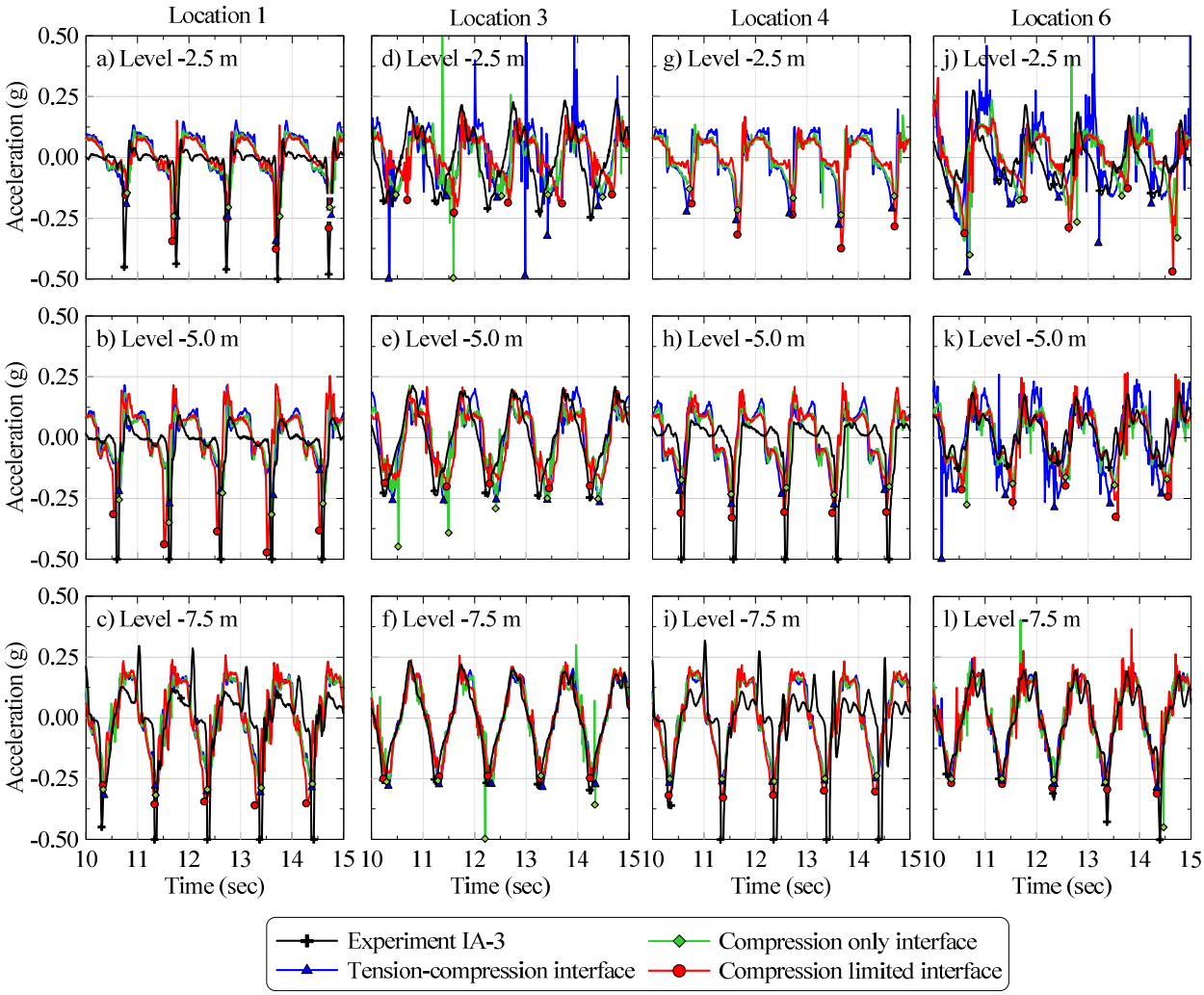

Figure 4-8: Acceleration time history comparison (10 to 15 sec time window) for numerical simulations using different soil-caisson interfaces and Experiment IA-3.

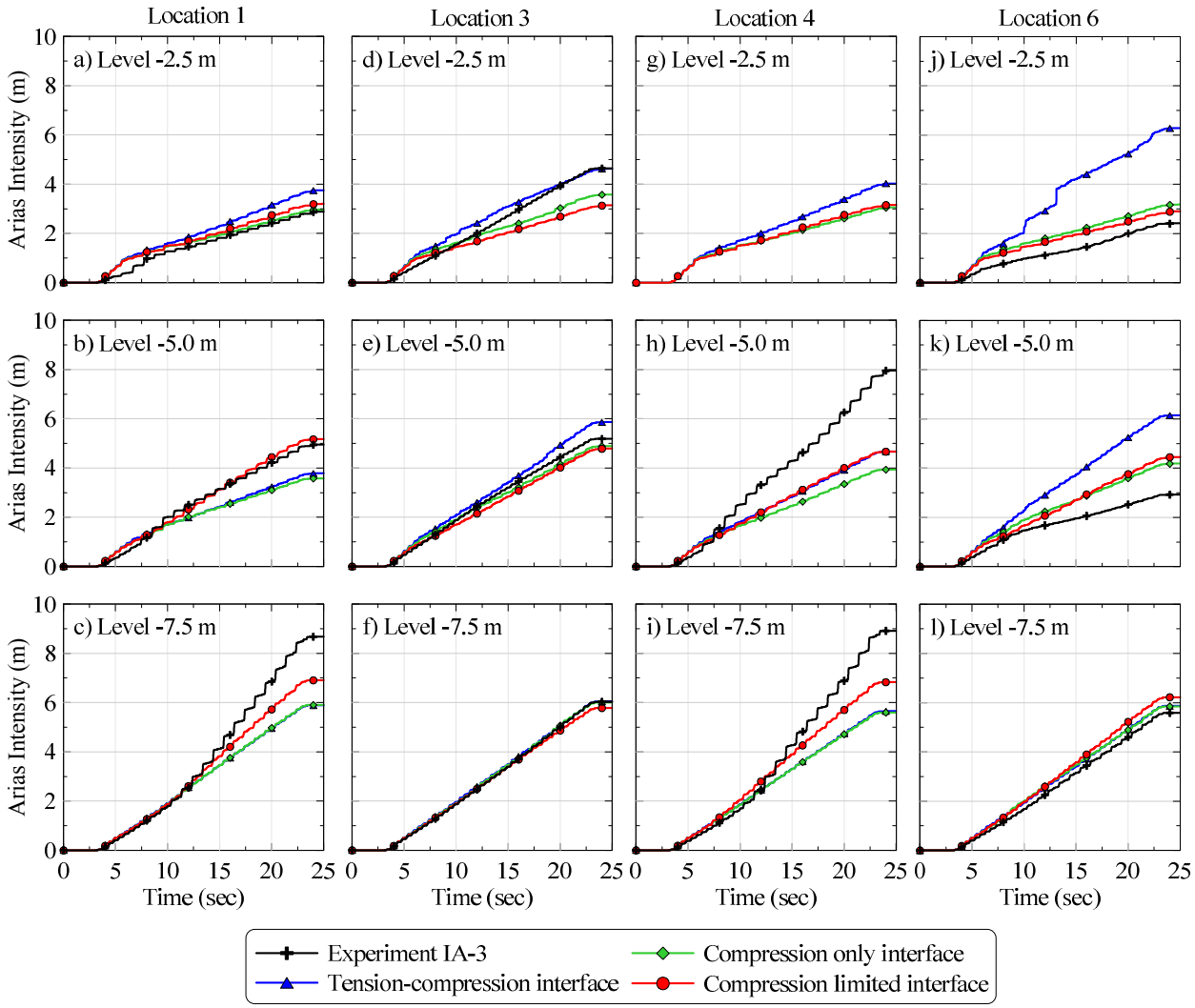

Figure 4-9: Arias intensity comparison for numerical simulations using different soil-caisson interfaces and Experiment I-A3.

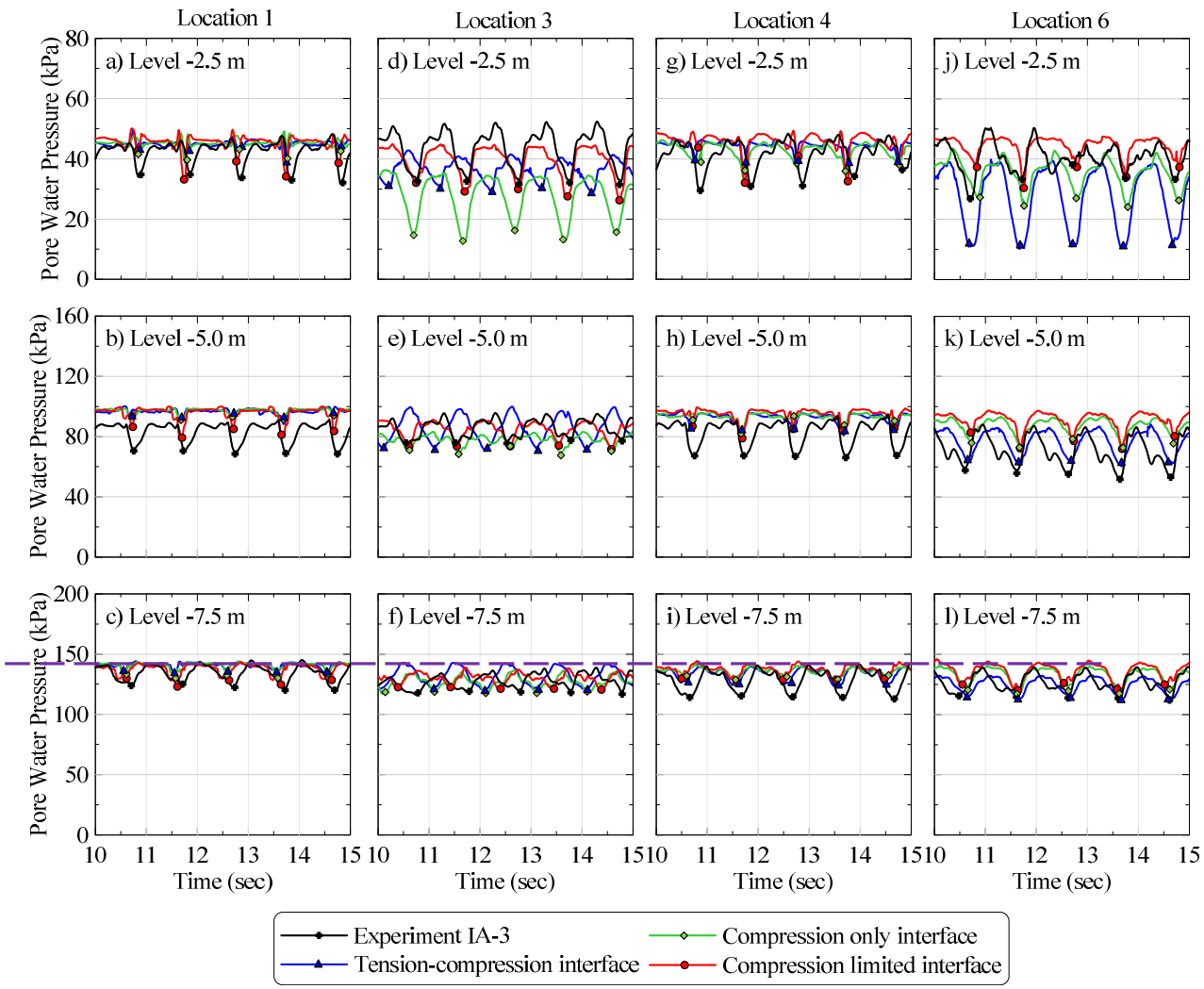

Figure 4-10: Pore water pressure time history comparison (10 to 15 sec time window) for numerical simulations using different soil-caisson interface connectors and Experiment IA-3.

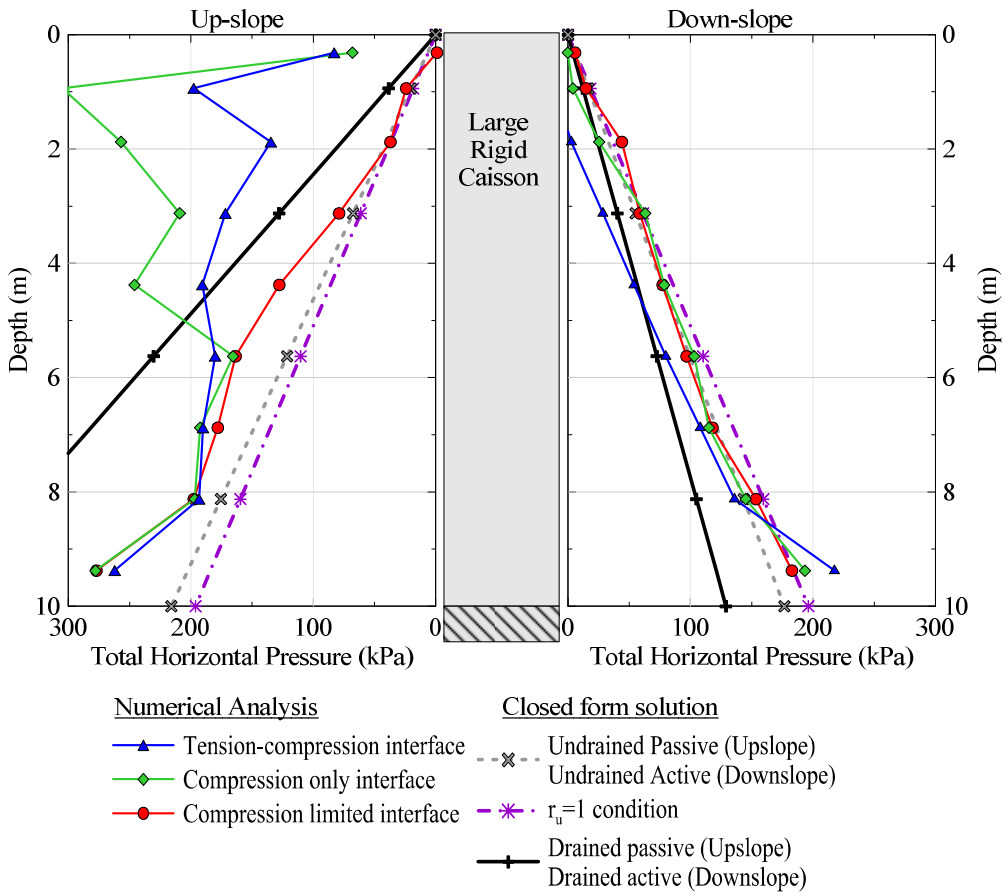

Figure 4-11: Pressure distribution for numerical simulations at max moment, different soil-caisson interface connectors input motion experiment I-A3.

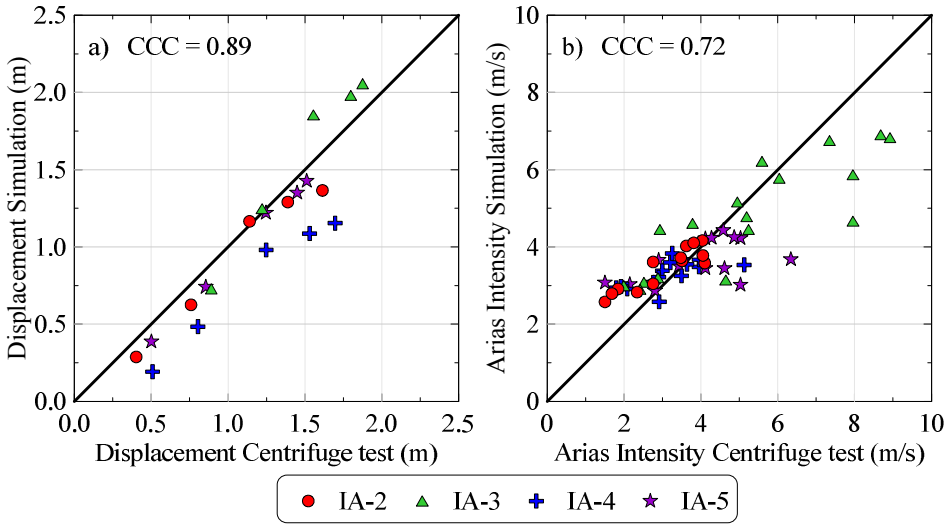

Figure 4-12: Comparison of simulated (using compression-limited interface) and measured values of (a) global displacement at the end of shaking; (b) Arias intensity.

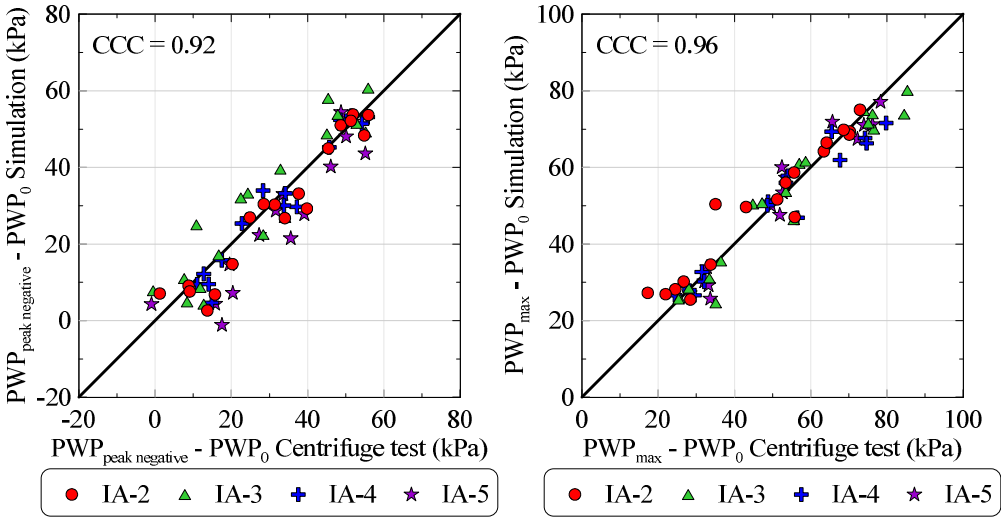

Figure 4-13: Comparison of simulated (using compression-limited interface) and measured PWP indices.

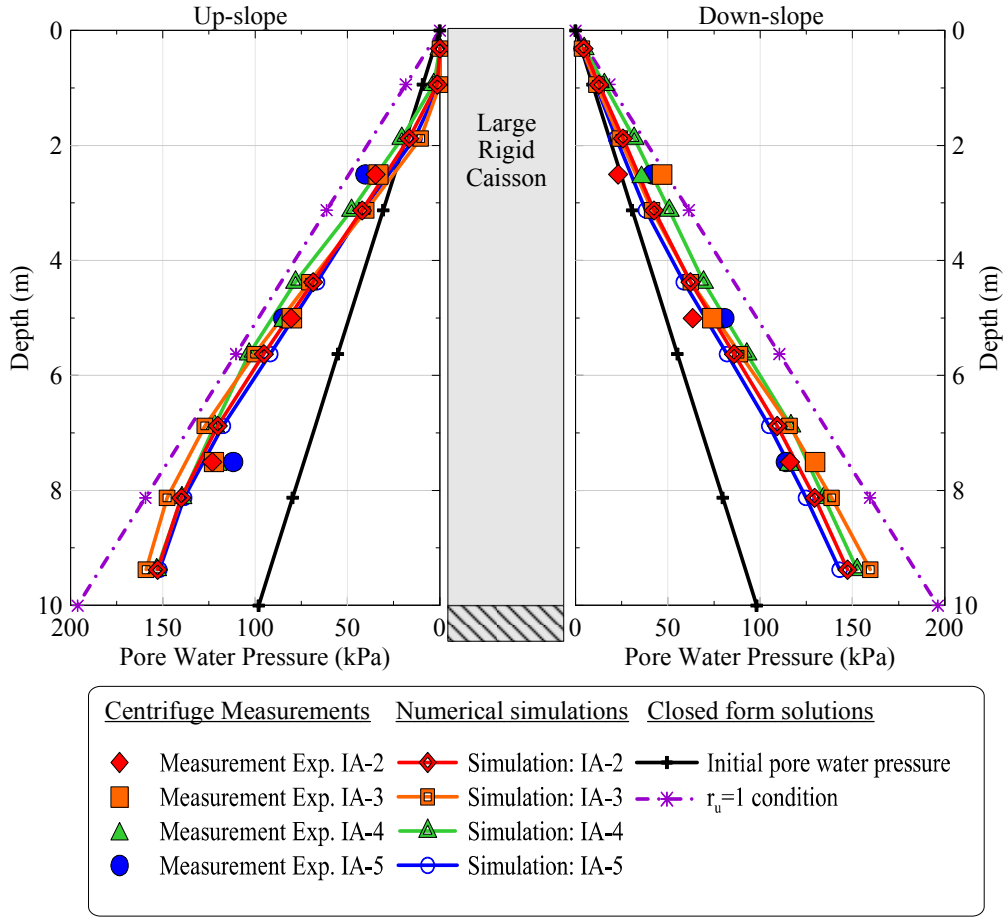

Figure 4-14: Pore water pressure distribution, centrifuge test simulations with compression-limited interface at time frame corresponding to the maximum bending moment (t = 19.73 sec).

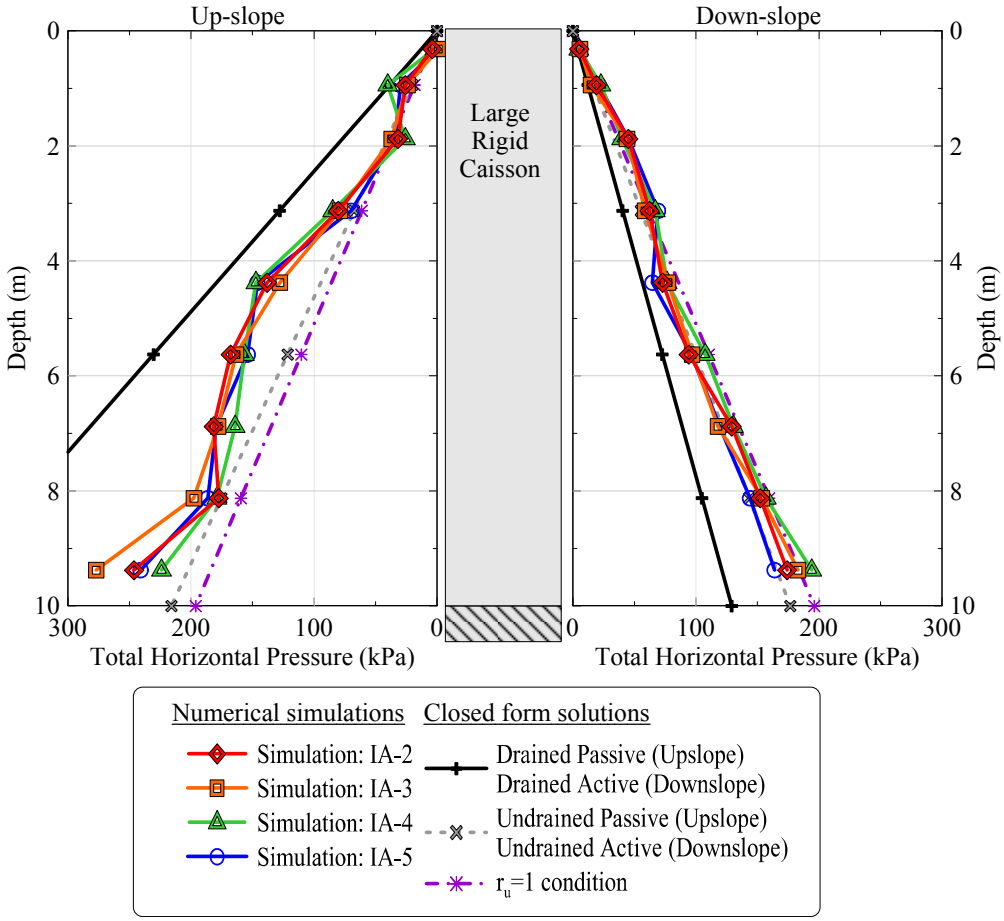

Figure 4-15: Total horizontal pressure distributions at time frame corresponding to maximum moment for the centrifuge test simulations with compression-limited interface elements.

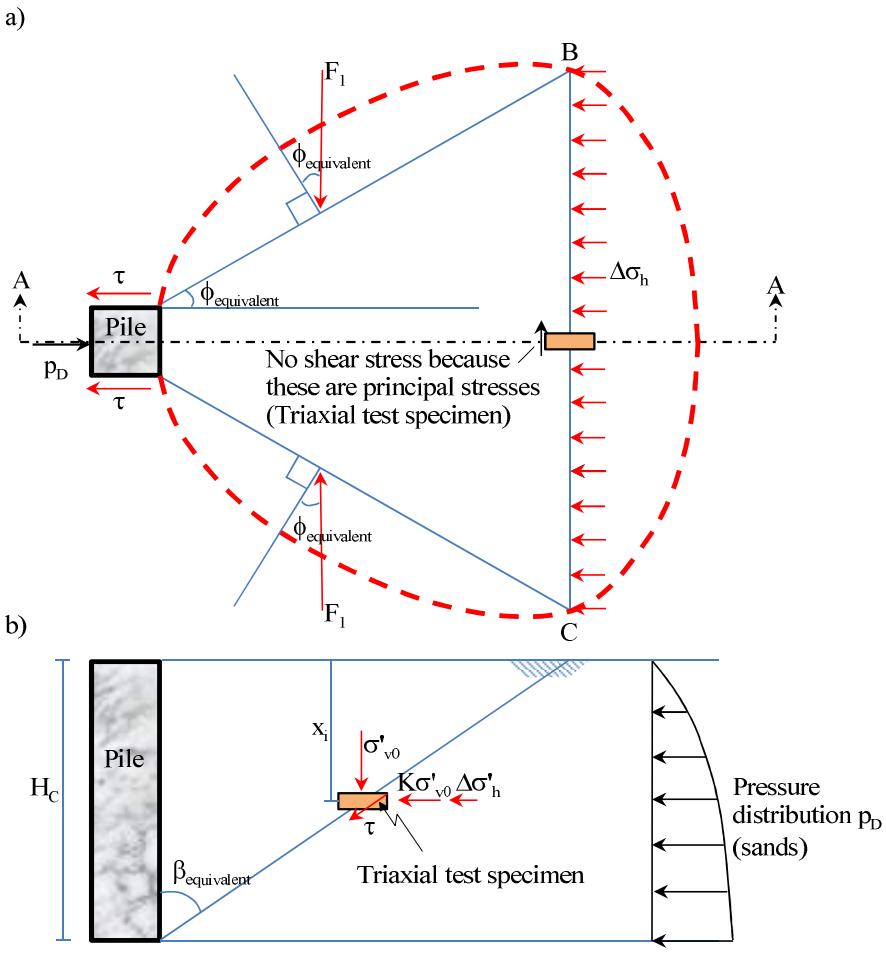

Figure 4-16: Schematic illustration of the strain wedge method [after Ashour (1998)].

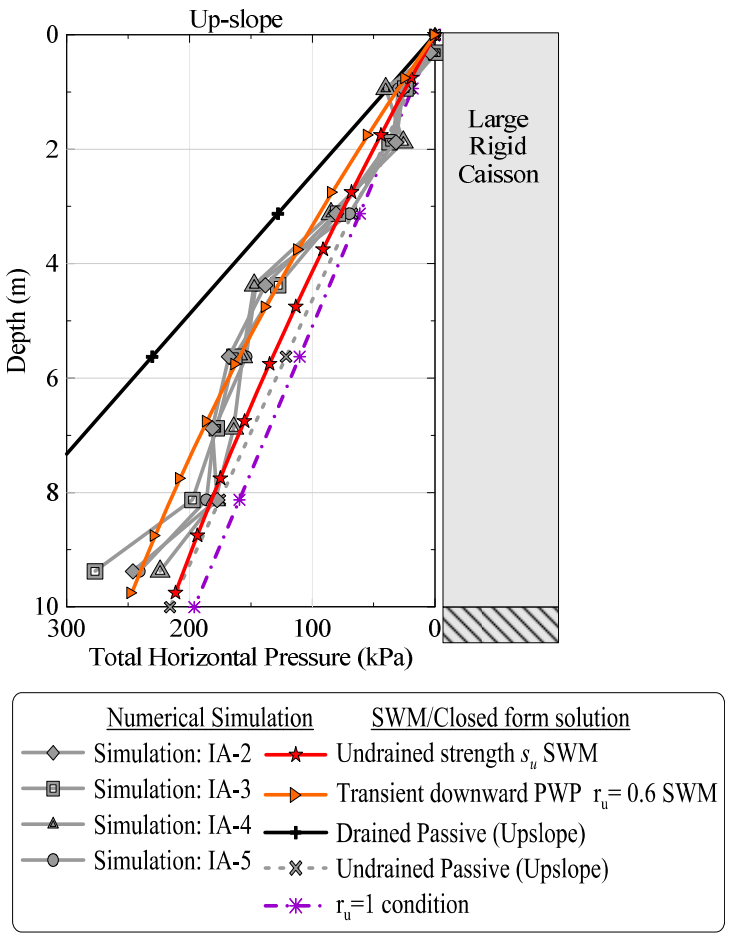

Figure 4-17: Comparison of simulated pressure distributions on the upslope face of the caisson with the pressure distributions calculated using the strain wedge method (SWM) for a passive wedge depth of 10m.

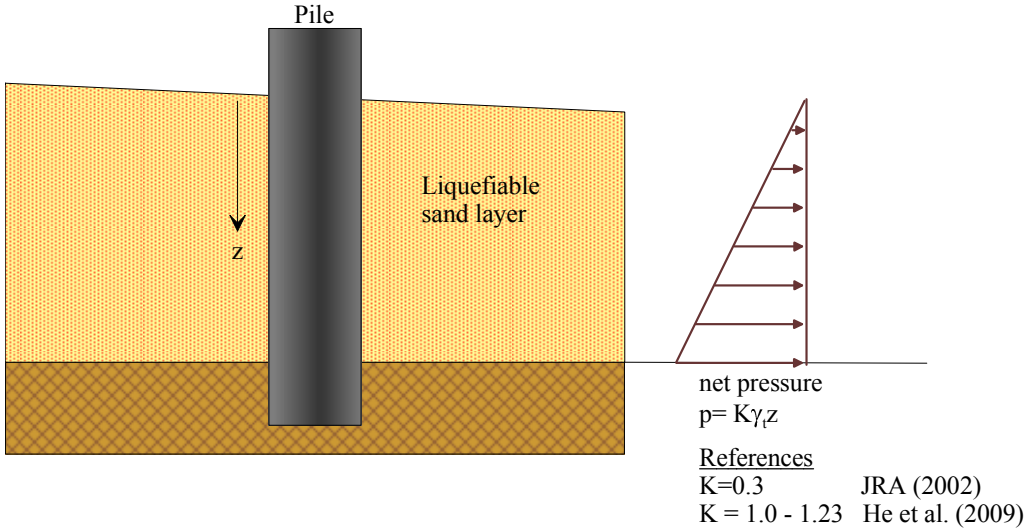

Figure 4-18: Schematic of the net pressure equivalent triangular distribution.

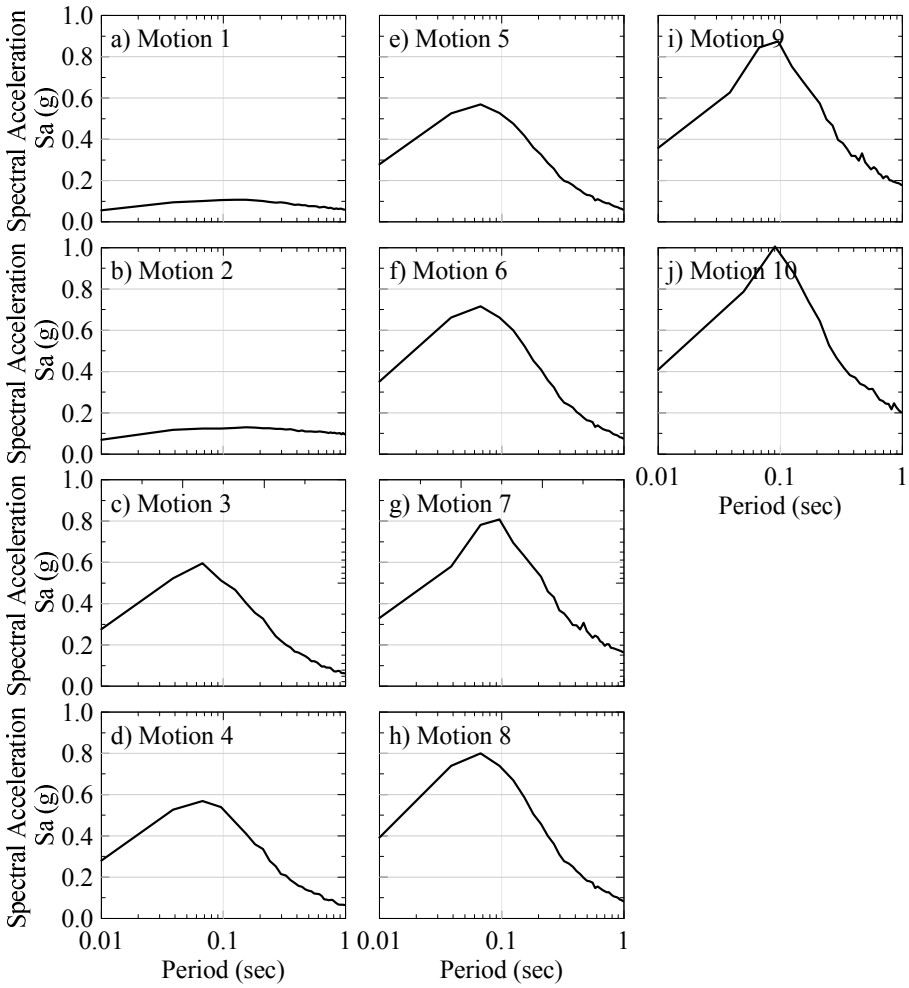

Figure 4-19: Response spectra for the ten input broadband motions selected for this study.

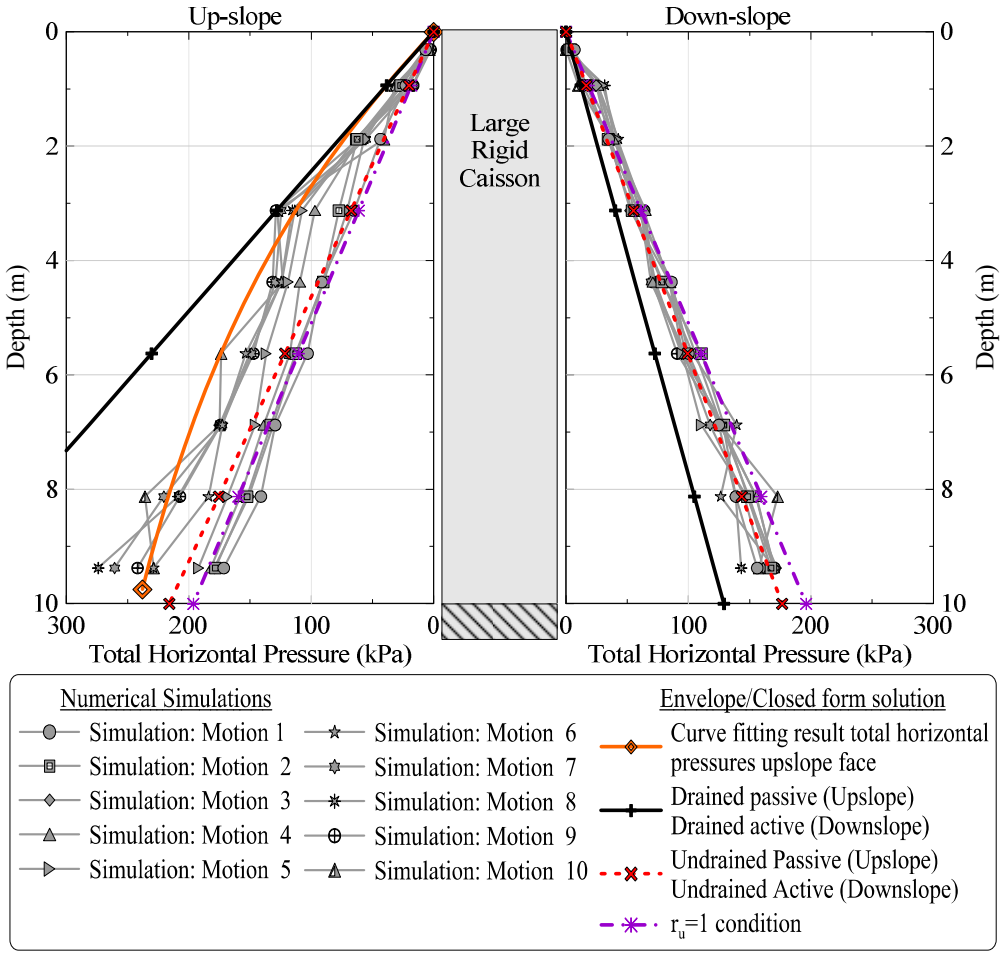

Figure 4-20: Comparison pressure distributions at max moment, numerical simulations using broadband motions.

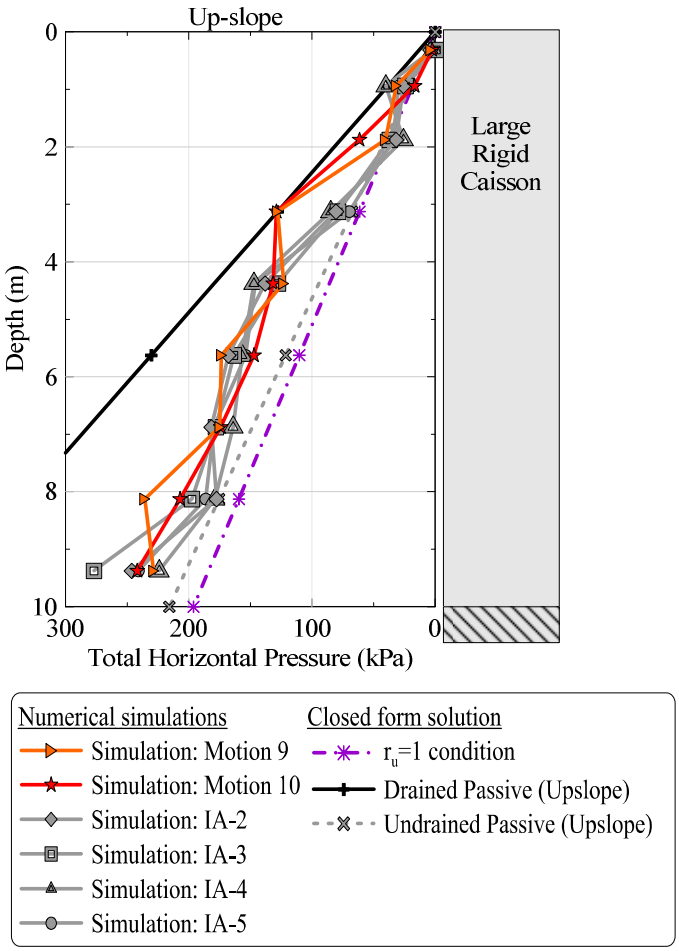

Figure 4-21: Comparison pressure distributions on the upslope face of the caisson at max moment, broadband and centrifuge numerical simulations.

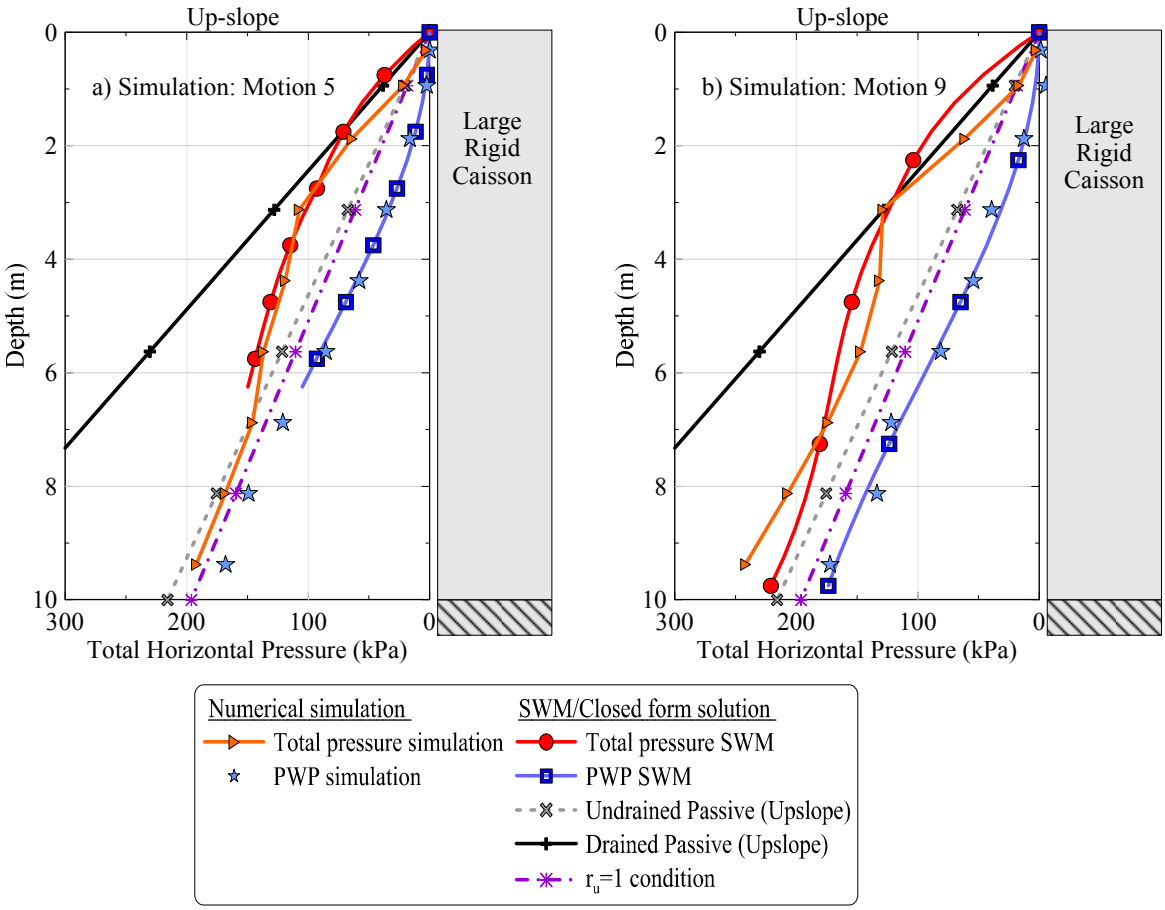

Figure 4-22: Comparison of total horizontal pressures at time frame where maximum moment occurred from simulations and SWM.

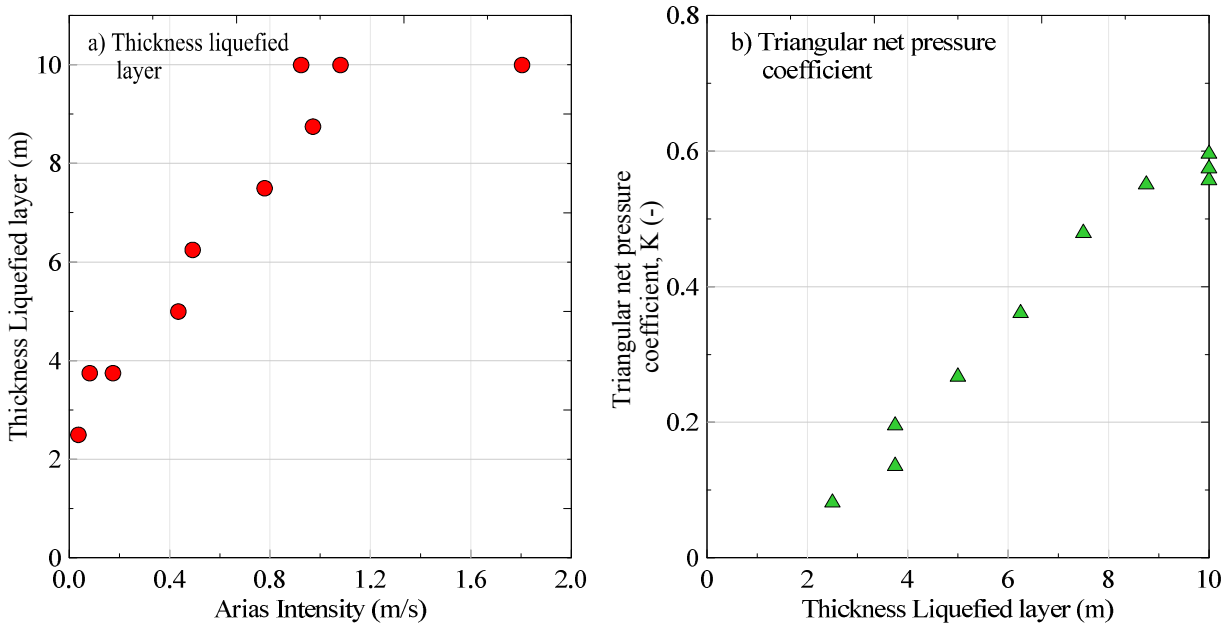

Figure 4-23: Broadband motion numerical simulation results. (a) liquefied layer thickness; and (b) back-calculated net triangular pressure coefficient.

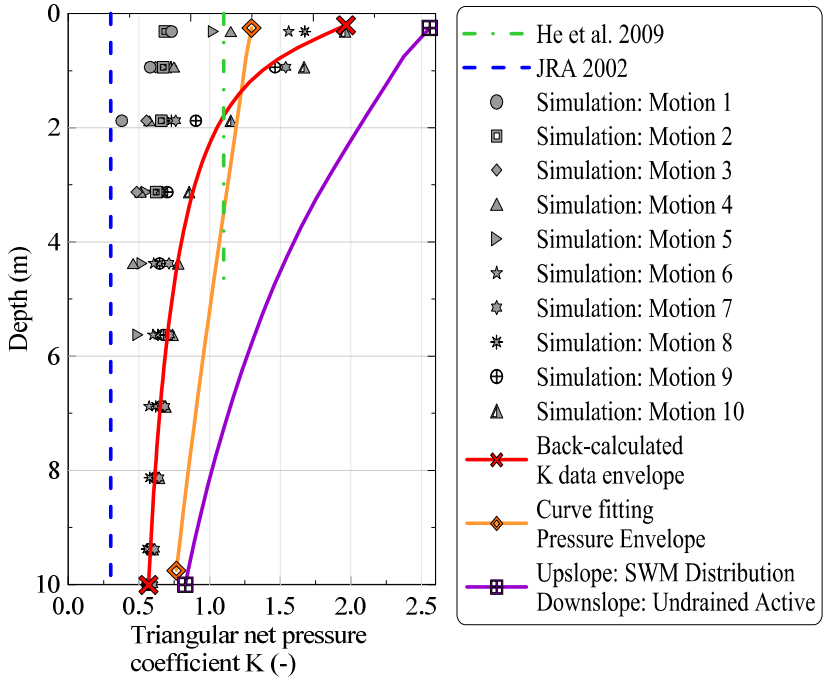

Figure 4-24: Triangular net pressure coefficient (K) as a function of depth for numerical simulations using broadband motions and sand soil permeability.

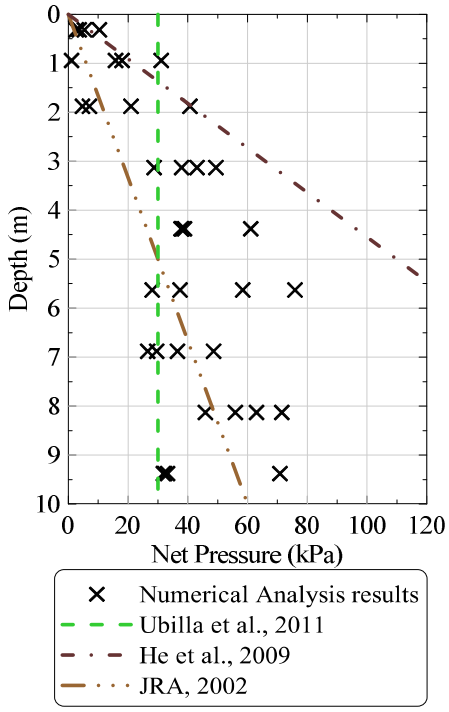

Figure 4-25: Net pressure comparison.

CHAPTER 5 – CONCLUSIONS

In Chapter 2, two new methodologies to model energy dissipation in one dimensional site response analysis were proposed. A series of time domain elastic site response analyses (with and without constant damping) show that the proposed frequency independent viscous damping provides results that more closely match the exact solution obtained for frequency domain analyses. The proposed methodology is an alternative to the commonly used Rayleigh damping formulation and circumvents the need to identify the two modes needed in Rayleigh damping.

A simplified constitutive model to simultaneously match modulus reduction and damping soil curves for nonlinear site response analysis is introduced. The proposed model uses the widely used modified hyperbolic model to represent the modulus reduction backbone curve. A damping reduction factor that modifies the Masing rule is introduced such that hysteretic damping better matches measured strain dependent damping. The model was tested for 50 different soil curves and a good match for modulus reduction and damping curves is obtained.

The proposed models overcome some longstanding limitations in nonlinear time-domain analysis regarding small and large strain damping. All the analyses presented in Chapter 2 correspond to total stress analysis. The implementation of the new models to effective stress analyses is beyond the scope of this thesis and is currently under investigation.

In Chapter 3 a soil constitutive model including viscous damping was calibrated using the displacement, acceleration, and pore water pressure time histories recorded in a free-field lateral spreading centrifuge test conducted as a part of a larger NEES experiment. The calibration highlights the need to including viscous damping to model soil small strain damping and the use of overburden pressure-dependent dilation parameters. The numerical model that provides the best overall match to the different recorded in the centrifuge test implements the effective stress-based constitutive model proposed by Yang (2000) with overburden pressure-dependent dilation parameters (contraction parameter c1 increasing with the increase of the initial effective vertical stress and dilation parameters d1 and d2 decreasing with the increase of the initial effective

vertical stress) and 3% viscous damping. The capability of the calibrated model was evaluated using a different free-field lateral spreading centrifuge test. The simulated results were in good agreement with the experiment displacement, acceleration and pore water pressure records. Numerical models were developed and calibrated in Chapter 4 using the displacement, acceleration, and pore water pressure time histories recorded in a lateral spreading centrifuge test with a large, rigid foundation element located in the path of downslope soil movement. The calibration focused in finding an adequate procedure to model the soil-caisson interface. The use of a compression-limited connection and an effective stress-based constitutive model reasonably replicated the boundary displacements, accelerations and pore water pressures recorded in four different centrifuge tests.

Analyses using the aforementioned numerical model with a realistic (i.e., not scaled by centrifugal acceleration) soil permeability and broadband input motions also were performed. The analyses using a realistic permeability yielded higher pressures for the upper 5 m of a 10-m thick loose sand profile, consistent with results obtained by others using large-scale laboratory tests and centrifuge tests.

The computed pressure distributions were analyzed using the strain wedge method (references), an equivalent triangular net pressure distribution, and the net pressure distribution. In general, the strain wedge method using undrained and drained strength parameters (with a porewater pressure ratio, ru = Δ_u/σ'_{vo} = 0.6 for the latter) provides reasonable lower and upper bounds, respectively, to the simulated upslope face pressures. The total pressures on the downslope face of the caisson closely resemble the undrained Rankine active pressure distribution.

Analyses using an equivalent triangular net pressure distribution have shown that the equivalent triangular pressure coefficient (K) is depth-dependent, rather than constant as proposed by others. The depth-dependent triangular pressure coefficient varied from about 2.0 near the surface to 0.5 at a depth of 10 m. This value is more than two times greater than the JRA (2002) design recommendation, but agrees with the reduced coefficient proposed by He et al.(2009) for the Showa Bridge case history.

The net pressure distribution increases from zero at the ground surface at a rate proportional to the square root of depth. The simulated net pressures are roughly bounded by the recommendations of JRA (2002) and He et al., (2009).

REFERENCES

Abdoun, Tarek, Dobry, Ricardo, O'Rourke, Thomas D., and Goh, S. H. (2003). "Pile response to lateral spreads: Centrifuge modeling," J. Geotech. and Geoenviron. Eng., 129(10), 869-878.

API (1987) *Recommended Practice for Planning, Designing and Constructing Fixed Offshore Platforms*.

Ashford, S, R. W. Boulanger, and S. J. Brandeberg (2011) "Recommended Design Practice for Pile Foundations in Laterally Spreading Ground," In: PEER, Ed. Davis, CA: University of California, Davis, p 43.

Ashford, S.A., Rollins, K.M., and Lane, J.D. (2004). "Blast-induced liquefaction for full-scale foundation testing", Journal of Geotechnical and Geoenvironmental Engineering, ASCE, Vol. 130, No. 8, August, pp 798-806.

Ashford, S.A., Rollins, K.M., Bradford V, S.C., Weaver, T.J., Baez, J.I. (2001). "Liquefaction Mitigation Using Stone Columns Around Deep Foundations: Full Scale Test Results," Soil Mechanics 2000. Transportation Research Record No 1736. Transportation Research Board, pp. 110-118.

Ashour, M., G. Norris, and P. . Pilling (1998) "Lateral loading of a pile in layered soil using the strain wedge model," *Journal of Geotechnical Engineering, ASCE*, Vol. 124, No. 4, pp 303-315.

Ashour, M., and Norris, G. M. (2003). "Lateral load pile response in liquefiable soil." J. Geotech. Geoenviron. Eng., 129(5), 404–414.

Bartlett, S. F., and T. L. Youd (1992) "Empirical analysis of horizontal ground displacement generated by liquefaction-induced lateral spread.." Buffalo, N.Y: National Center for Earthquake Engineering Research, Buffalo, N.Y, p 114.

Baziar, M.H. , and A. Ghorbani (2005) "Evaluation of lateral spreading using artificial neural networks," *Soil Dynamics and Earthquake Engineering*, Vol. 25, No. 1, pp 1-9.

Beavers, J.E. (1991) "Costa Rica Earthquake Reconnaissance Report," In: J.E. Beavers, Ed.: Earthquake Spectra, EERI, Supplement B, p 127.

Berrill, J. B., Christensen, S. A., Keenan, R. J., and Okada, W. (1997). "Lateral-spreading loads on a piled bridge foundation." *Seismic Behavior of Ground and Geotechnical Structures,* Seco e Pinto (ed.), Balkema, Rotterdam, 173-183.

Biot, M.A. (1962) "The Mechanics of Deformation and Acoustic Propagation in Porous Media," *Journal of Applied Physics*, Vol. 33, No. 4, pp 1482-1498.

Borja, Ronaldo I., Chao-Hua Lin, Kossi M. Sama, and Gwynn M. Masada (2000) "Modelling non-linear ground response of non-liquefiable soils," *Earthquake Engineering and Structural Dynamics,*, Vol. 29, No. 1, pp 63-83.

Boulanger, R. W., B. L. Kutter, S. J. Branderberg, P. Singh, and D. Chang (2003) "Pile foundations in liquefied and laterally spreading ground during earthquakes: centrifuge experiments & analyses." Davis, California: University of California at Davis.

Boulanger, R.W. , R. Arulnathan, L.F. Jr. Harder, R.A. Torres, and M.W. Driller (1998) "Dynamic properties of Sherman Island peat," *Journal of Geotechnical and Geoenvironmental Engineering*, Vol. 124, No. 1, pp 12-20.

Bozzano, F., A. Caserta, A. Govoni, F. Marra, and S. Martino (2008) "Static and dynamic characterization of alluvial deposits in the Tiber River Valley: New data for assessing potential ground motion in the City of Rom," *Journal of Geophysical Research B: Solid Earth*, Vol. 113, No. 1, p art. no. B01303.

Brandeberg, S. J., and R. W. Boulanger (2004) "OpenSees beam on nonlinear Winkler foundation modeling of pile groups in liquefied laterally spreading ground in centrifuge tests," *Asia-pacific network of centers for earthquake reasearch*. Honolulu, HI.

Brandenberg, S. J., Boulanger, R. W., Kutter, B. L., and Chang, D. (2005). "Behavior of pile foundations in laterally spreading ground during centrifuge tests." J. Geotech. Geoenviron. Eng., 131(11), 1378-1391.

Brown, D.A. and Camp, W.M. (2002). "Lateral load testing for the Cooper River Bridge, Charleston, SC" Proceedings of the International Deep Foundations Congress, Vol. 1 (GSP 116), ASCE, Reston,VA: 95-109.

Cardona, O. D. , and L. E Yamin (1997) "Seismic microzonation and estimation of earthquake loss scenarios: Integrated risk mitigation project of Bogota, Colombia," *Earthquake Spectra*, Vol. 13, No. 4, pp 795-813.

Carrubba, P., Maugeri, M. (1999) "Dynamic soil properties from full scale tests with a vibrating foundation," *2nd international conference on earthquake geotechnical engineering*. Lisbon, Portugal: Balkema, pp 35-40.

Cetin, K. Onder, Raymond B. Seed, Armen Der Kiureghian, Kohji Tokimatsu, Jr. Leslie F. Harder, Robert E. Kayen, and Robb E. S. Moss (2004) "Standard Penetration Test-Based Probabilistic and Deterministic Assessment of Seismic Soil Liquefaction Potential," *Journal of Geotechnical and Geoenvironmental Engineering* Vol. 130, No. 12, pp 1314 -1340.

Chan, A.H.C. (1988) "A Unified Finite Element Solution to Static and Dynamic Problems in Geomechanics," *Civil Engineering*. Swansea, U.K.: University College of Swansea.

Chang, C.-Y., C.-M. Mok, Z.-L. Wang, R. Settgast, C.-C. Chin, H.M. Gonnermann, F. Waggoner, and M.A Ketchum (2001) "Dynamic soil-foundation-structure interaction analyses of large caissons.," *Proc., 4th Int. Conf. on Recent Advances in Geotechnical Earthquake Engineering and Soil Dynamics and Symposium in Honor of W.D. Liam Finn,*. San Diego, CA.

Chen L, Poulos HG (1997). Pile Subjected to Lateral Soil Movements, J. Geotech. Geoenviron. Eng. ASCE 123(9): 802-811.

Chiru-Danzer, M. , C.H. Juang, R.A. Christopher, and J. Suber (2001) "Estimation of liquefaction-induced horizontal displacements using artificial neural networks," *Canadian Geotechnical Journal*, Vol. 38, No. 1, pp 200-207.

Clough, Ray W., and Joseph Penzien (1993) *Dynamics of structures*, New York: McGraw-Hill.

Crespellani, T., C. Madiai, G. Simoni, and G. Vanucchi (2001) "Dynamic geotechnical testing and seismic response analyses in two sites of the Commune of Nocera Umbra, Italy," *Rivista Italiana di Geotecnica*, Vol. 35, No. 4, pp 39-52.

Cubrinovski, M., T. Kokusho, and K. Ishihara (2006). "Interpretation from large-scale shake table tests on piles undergoing lateral spreading in liquefied soils," Soil Dynamics and Earthquake Eng., 26, 275-286.

Darendeli, M. B. (2001) "Development of a new family of normalized modulus reduction and material damping curves," *Civil Engineering*. Austin: University of Texas at Austin, p 395.

Davidenkov, N.N. (1938) "Energy dissipation in vibrations," *Journal of Technical Physics*, Vol. 8, No. 6.

Dobry, R. , S. Thevanayagam, C. Medina, R. Bethapudi, A. Elgamal, V. Bennett, T. Abdoun, M. Zeghal, U. El Shamy, and V.M. Mercado (2010) "Mechanics of lateral spreading observed in a full-scale shake test," *Journal of Geotechnical and Geoenvironmental Engineering* Vol. 137, No. 2, pp 115-129.

Dobry, R., Abdoun, T., O'Rourke, T.D., and Goh, S.H. (2003). "Single Piles in Lateral Spreads: Field Bending Moment Evaluation". Journal of Geotechnical and Geoenvironmental Engineering, 129(10), 879-889.

Dungca J. R., J. Kuwano, A. Takahashi, T. Saruwatari, J. Izawa, H. Suzuki, and K. Tokimatsu (2006). "Shake table tests on the lateral response of a pile buried in liquefied sand," Soil Dynamics and Earthquake Eng.,

Duncan, James M., and Chin-Yung Chang (1970) "Nonlinear analysis of stress and strain in soils," *Journal of the Soil Mechanics and Foundations Division*, Vol. 96, No. SM5, pp 1629-1653.

Elgamal, A., Z. Yang, T. Lai, B. L. Kutter, and D. W. Wilson (2005) "Dynamic response of saturated dense sand in laminated centrifuge container," *Journal of Geotechnical and Geoenvironmental Engineering*, Vol. 131, No. 5, pp 598-609.

Elgamal, A., Z. Yang, and E. Parra (2002) "Computational Modeling of Cyclic Mobility and Post-Liquefaction Site Response," *Soil Dynamics and Earthquake Engineering*, Vol. 22, No. 4, pp 259-271.

Elgamal, A., Z. Yang, E. Parra, and A. Ragheb (2003) "Modeling of Cyclic Mobility in Saturated Cohesionless Soils," *International Journal of Plasticity*, Vol. 19, No. 6, pp 883-905.

GEER, Geo-Engineering Extreme Events Reconnaissance Association (2010) "Geo-engineering Reconnaissance of the 2010 Maule,Chile Earthquake," In: Bray J., and D Frost, Eds.: National Science Foundation, NSF, p 272.

Gerolymos, N., and G. Gazetas (2005) "Constitutive model for 1-D cyclic soil behaviour applied to seismic analysis of layered deposits," *Soils and Foundation*, Vol. 45, No. 3, pp 147-159.

Goh, S.-H. and O' Rourke, T. D., (1999), "Limit State Model for Soil-Pile Interaction During Lateral Spread," Proc. Seventh U.S.-Japan Workshop on Earthquake Resistant Design of Lifeline Facilities and Countermeasures Against Soil Liquefaction, Seattle, WA, August 15-17, Technical Report MCEER-99-0019, Multidisciplinary Center for Earthquake Engineering Research, University at Buffalo, (O'Rourke, Bardet and Hamada, eds.), pp. 237-260.

Gonzalez, Lenart, Tarek Abdoun, and Ricardo Dobry (2009) "Effect of soil permeability on centrifige modeling of pile response to lateral spreading," *Journal of Geotechnical Engineering and Geoenvironmental Engineering*, Vol. 135, No. 1, pp 62-73.

Hamada, M., and T.D. O'Rourke (1992) "Case Studies of Liquefaction and Lifeline Performance During Past Earthquakes." Buffalo, NY: State University of New York at Buffalo, p 341.

Hamada, M., and T.D. O'Rourke (1992) "Case Studies of Liquefaction and Lifeline Performance During Past Earthquakes." Buffalo, NY: National Center for Earthquake Engineering Research, University at Buffalo, NY.

Hashash, Y. M. A. (2005) "DEEPSOIL V 2.6, Tutorial and User Manual. 2002-2005." Urbana Illinois: University of Illinois at Urbana-Champaign, p 49.

Harada, N., Towhata I., Takatsu T., Tsunoda, S. & Sesov, V. 2006. Development of new drain method for prdiction of existing pile foundations from liquefaction effects. Soil Dynamics and Earthquake Engineering, 26 (4): 297–312.

He, Liangcai, Ahmed Elgamal, Tarek Abdoun, Akio Abe, Ricardo Dobry, Masanori Hamada, Jorge Menses, Masayoshi Sato, Thomas Shantz, and Kohji Tokimatsu (2009) "Liquefaction-induced lateral load on pile in a medium dr sand layer," *Journal of Earthquake Engineering*, Vol. 13, No. 7, pp 916-938.

Hudson, M., I. M. Idriss, and M. Beikae (1994) "QUAD4M - A computer program to evaluate the seismic response of soil structures using finite element procedures and incorporating a compliant base." Davis, CA: Center for Geotechnical Modeling, Department of Civil and Environmental Engineering, University of California, Davis, CA.

Hudson, M., Idriss, I.M., and Beikae, M. 1994. (1994) "QUAD4M - A computer program to evaluate the seismic response of soil structures using finite element procedures and incorporating a compliant base.." Davis, CA: Center for Geotechnical Modeling, Department of Civil and Environmental Engineering, University of California, Davis, CA.

JGS, Japanese Geotechnical Society (1996) "Special Issue on Geotechnical Aspects of the January 17, 1995 Hyogoken-Nambu Earthquake," *Soils and Foundations*, p 358.

JRA (2002) "Specification for highway bridges," In: Japan Road Association, Ed.

Kawakami, T. (1996) "Experimental study on countermeasures against liquefaction-induced lateral ground movement by in-ground wall.," *Proc., 6th Japan-US Workshop on Earthquake Resistant Design*

of Lifeline Facilities and Countermeasures for Soil Liquefaction. Buffalo, NY.: NCEER, pp 477-486.

Keane, C.M., and J.H. Prevost (1990) "Preliminary results of a numerical technique to model flow failure induced by soil liquefaction.," *3rd Japan-US Workshop on Earthquake Resistant Design on Lifeline Facilities and Countermeasures for Soil Liquefaction*. San Francisco, pp 253-267.

Kokusho, Takaji, Tomohiro Aoyagi, and Akihiro Wakunami (2005) "In Situ Soil-Specific Nonlinear Properties Back-Calculated from Vertical Array Records during 1995 Kobe Earthquake," *Journal Geotechnical and Geoenvironmental Engineering*, Vol. 131, No. 12, pp 1509-1521.

Kramer, S. L. (2000) "Dynamic response of mercer slough peat," *Journal of Geotechnical and Geoenvironmental Engineering*, Vol. 126., No. 6, pp 504-510.

Kramer, S. L. (1996a) *Geotechnical earthquake engineering*, Prentice Hall, Upper Saddle River, N.J: Prentice Hall.

Kramer, Steven Lawrence (1996b) *Geotechnical earthquake engineering*, Upper Saddle River, N.J.: Prentice Hall.

Kutter, B. L., S. Gajan, K. K. Manda, and A. Balakrishnan (2004) "Effects of layer thickness and density on settlement and lateral spreading," *Journal of Geotechnical and Geoenvironmental Engineering*, Vol. 130, No. 6, pp 603-614.

Kuwano, J., and K. Ishihara (1988) "Analysis of permanent deformation of earth dam due to earthquakes.," *Soils and Foundations*, Vol. 28, No. 1, pp 14-55.

Kwok, A. O. L., J. P. Stewart, Y. M. A. Hashash, N. Matasovic, R. Pyke, Z. Wang, and Z. Yang (2007a) "Use of exact solutions of wave propagation problems to guide implementation of nonlinear, time-domain ground response analysis routines.," *Journal of Geotechnical and Geoenvironmental Engineering*, Vol. 133, No. 11, pp 1385-1399.

Kwok, Annie O.L., Jonathan P. Stewart, Youssef M.A. Hashash, Neven Matasovic, Robert Pyke, Zhiliang Wang, and Zhaohui Yang (2007b) "Use of exact solutions of wave propagation problems to guide implementation of nonlinear, time-domain ground response analysis routines.," *ASCE Journal of Geotechnical and Geoenvironmental Engineering*, Vol. in press.

Lai, C. G., and G. J. Rix (1998a) "Simultaneous Inversion of Rayleigh Phase Velocity and Attenuation for Near-Surface Site Characterization," Georgia Institute of Technology.

Lai, C. G., and G. J. Rix (1998b) "Simultaneous Inversion of Rayleigh Phase Velocity and Attenuation for NearSurface Site Characterization." Atlanta. GA: Georgia Institute of Technology.

Lam, Ignatius, Pedro Arduino, and Peter Mackenzie-Helnwein (2009) "OPENSEES soil-pile interaction study under lateral spread loading," *Contemporary Topics in In Situ Testing, Analysis, and Reliability of Foundations - Proceedings of Selected Sessions of the 2009 International Foundation Congress and Equipment Expo*: American Society of Civil Engineers, pp 206-213.

Lee, M.K., and W.D.L. Finn (1978) "DESRA-2, Dynamic effective stress response analysis of soil deposits with energy transmitting boundary including assessment of liquefaction potential," *Soil Mechanics Series, No. 36*. Vancouver, Canada: Department of Civil Engineering, University of British Columbia.

Lin, Lawrence I-Kuei (1989) "A Concordance Correlation Coefficient to Evaluate Reproducibility," *Biometrics*, Vol. 45, No. 1, pp 255-268.

Liu, M., and D.G. Gorman (1995) "Formulation of Rayleigh damping and its extensions," *Computers and Structures*, Vol. 57, No. 2, pp 277-285.

Liu, W.D., X. Chen, K.K. Chang, and R.A Imbsen (1998) "Performance-based seismic evaluation of bridge foundations.," *Int. Conf. on Geotechnical Earthquake Engineering and Soil Dynamics, .* University of Washington, Seattle, WA,: ASCE Special Publication No. 75, August 3-6, Vol. 2, 1368-1379, pp 1368-1379.

Lu, J., Yang, Z., and Elgamal, A. (2010). "OpenSeesPL 3D lateral plie-ground interaction: User's manual". University of California, San Diego. (https://neesforge.nees.org/projects/OpenSeesPL)

Mageau, D., and S Stauffer (1998) "Lateral spread earth pressures on drilled shafts.," *3rd Int. Conf. on Geotechnical Earthquake Engineering and Soil*. University of Washington, Seattle, WA.: ASCE, pp 1344-1355.

Masing, G. (1926) "Eignespannungen und Verfestigung beim Messing," *Second International Congress on Applied Mechanics*. Zurich, Switzerland, pp 332-335.

Matasovic, Neven (1993) "Seismic response of composite horizontally-layered soil deposits," University of California, Los Angeles, pp xxix, 452 leaves.

Matlock, H. (1970) "Correlations for design of laterally loaded piles in soft clay.," *Proc., 2nd Annual Offshore Technology Conf., Houston*, Vol. 1, pp 577-594.
Mazzoni, S., F. McKenna, M. H. Scott, and G. L. Fenves (2006) "Open System for Earthquake Engineering Simulation User Command-Language," In: NEES, Ed. Berkeley, CA.
Menq, Farn-Yuh (2003) "Dynamic Properties of Sandy and Gravelly Soils," *Civil and Environmental Engineering*. Austin, TX: University of Texas at Austin, p 364.
Muravskii, G. (2005) "On description of hysteretic behaviour of materials," *International Journal of Solids and Structures*, Vol. 42, pp 2625-2644.
Muravskii, G., and S. Frydman (1998) "Site response analysis using a nonlinear hysteretic model," *Soil Dynamics and Earthquake Engineering*, Vol. 17, pp 227–238.
Newmark, N.M. (1959) "A Method of Computation for Structural Dynamics," *Journal of the Engineering Mechanics Division*, Vol. 85, pp 67-94.
Ohtomo, K. (1996) "Soil force on conduit pile system due to liquefaction-induced lateral flow.," *Proc., 6th Japan-US Workshop on Earthquake Resistant Design of Lifeline Facilities and Countermeasures for Soil Liquefaction*. Buffalo, NY: NCEER, pp 541-550.
Okur, D.V., and A. Ansal (2007) "Stiffness degradation of natural fine grained soils during cyclic loading.," *Soil Dynamics and Earthquake Engineering*, Vol. 27, No. 9, pp 843-854.
Olson, S. M., and C. I. Johnson (2008) "Analyzing Liquefaction-induced lateral spreads using strength ratios," *Journal of Geotechnical and Geoenvironmental Engineering*, Vol. 134, No. 8, pp 1035-1049.
Pan, J. L., Goh, A. T. C., Wong, K. S., and Teh, C. I. (2002). “Ultimate soil pressures for piles subjected to lateral soil movements.” J. Geotech. Geoenviron. Eng., 128(6), 530–535.
Park, D., and Y. M. Hashash (2004a) "Estimation of non-linear seismic site effects for deep deposits of the Mississippi Embayment." Urbana: Mid America Earthquake Center, p 276.
Park, D., and Y. M. A. Hashash (2005) "Evaluation of seismic site factors in the Mississippi Embayment. I. Estimation of dynamic properties," *Soil Dynamics and Earthquake Engineering*, Vol. 25, No. 2, pp 133-144.
Parra, E. (1996) "Numerical Modeling of Liquefaction and Lateral Ground Deformation Including Cyclic Mobility and Dilation Response in Soil Systems," *Department of Civil Engineering*. Troy, NY: Rensselaer Polytechnic Institute.
PEER, Pacific Earthquake Engineering Research Center (2000) "PEER Strong Database," PEER.
Phillips, C., and Y. M. A. Hashash (2009) "Damping formulation for nonlinear 1D site response analyses," *Soil Dynamics and Earthquake Engineering*, Vol. 29, No. 7, pp 1143-1158.
Phillips, Camilo, Youssef M.A. Hashash, Scott M Olson, and Mark R. Muszynski (2012) "Significance of small strain damping and dilation parameters in numerical modeling of free-field lateral spreading centrifuge tests," *Soil Dynamics and Earthquake Engineering*, Vol. in press.
PoLam I., Kapuskar M., Chaudhuri D. (1998) Modeling of Pile Footings and Drilled Shafts for Seismic Design, Technical Report MCEER-98-0018
Press, William H., Saul A. Teukolsky, William T. Vetterling, and Brian P. Flannery (1992) *Numerical Recipes in FORTRAN 77 The Art of Scientific Computing*, Cambridge, UK: Cambridge University Press.
Prevost, J.H. (1985) "A Simple Plasticity Theory for Frictional Cohesionless Soils," *International Journal of Soil Dynamics and Earthquake Engineering*, Vol. 4, No. 1, pp 9-17.
Puri, Vijay K., and Shamsher Prakash (2008) "Pile design in liquefying soil," *The 14 th World Conference on Earthquake Engineering*. Beijing, China.
Puzrin, A.M. , and J.B. Burland (1996) "A logarithmic stress–strain function for rocks and soils," *Geotechnique*, Vol. 46, No. 1, pp 157–164.
Pyke, R M (1979) "Nonlinear soil models for irregular cyclic loadings," *Journal of the Geotechnical Engineering Division*, Vol. 105, No. GT6, pp 715-726.
Pyke, Robert (2000) "TESS: A computer program for nonlinear ground response analyses." Lafayette, California: TAGA Engineering Systems and Software.

Rauch, A. F., and J. R. Martin, II. (2000) "EPOLLS model for predicting average displacements on lateral spreads," *Journal of Geotechnical and Geoenvironmental Engineering*, Vol. 126, No. 4, pp 360-371.

Rayleigh, J.W.S., and R.B. Lindsay (1945a) *The theory of sound*, New York, NY: Dover.

Rayleigh, John William Strutt, and Robert Bruce Lindsay (1945b) *The theory of sound*, New York: Dover Publications.

Rollins, K.M., Gerber, T.M., Lane, J.D. and Ashford, S.A. (2005), "Lateral Resistance of a Full Scale Pile Group in Liquefied Sand", *Journal of Geotechnical and Geoenvironmental Engineering*, ASCE, Vol. 131, No. 1, January, pp 115-125.

Ross, G.A., H.B. Seed, and R. R. Migliaccio (1973) "Performance of Highway Bridge Foundations," *The Great Alaska Earthquake of 1964*, pp 190-242.

Schnabel, P.B., J.L. Lysmer, and H.B. Seed (1972) "SHAKE: A computer program for earthquake response analysis of horizontally layered sites." Berkeley, CA: Earthquake Engineering Research Center.

Seed, H. B., K. Tokimatsu, L. F. Harder, and R. M. Chung (1985) "The influence of SPT procedures in soil liquefaction resistance evaluations.," *Journal of the Geotechnical Engineering Division, American Society of Civil Engineers*, Vol. 111, No. 12, pp 1425-1445.

Seed, H. B., R. T. Wong, I. M. Idriss, and K. Tokimatsu (1986) "Moduli and Damping Factors for Dynamic Analyses of Cohesionless Soils," *Journal of the Soil Mechanics and Foundations Division, ASCE*, Vol. 112, No. SM11.

Seed, Harry Bolton, and I. M. Idriss (1970) *Soil moduli and damping factors for dynamic response analyses*, Berkeley: College of Engineering University of California Berkeley.

Seed, R. B., and L. F. Harder (1990) "SPT-based analysis of cyclic pore pressure generation and undrained residual strength," *H. Bolton Seed Memorial Symposium*. Vancouver, B. C., Canada: BiTech.

Shamoto, Yasuhiro, Jian-Min Zhang, and Kohji Tokimatsu (1998) "New Charts for Predicting Large Residual Post-Liquefaction Ground Deformation, ," *Soil Dynamics and Earthquake Engineering*, Vol. 17 pp 427-438.

Sharp, Michael K., Ricardo Dobry, and A.M.ASCE Tarek Abdoun (2003) "Liquefaction Centrifuge Modeling of Sands of Different Permeability," *Journal of Geotechnical and Geoenvironmental Engineering*, Vol. 129, No. 12, pp 1083-1091.

Shengcong, F., and F Tatsuoka (1984) "Soil Liquefaction During Haicheng and Tangshan Earthquake in China; A Review," *Soils and Foundations*, Vol. 24, No. 4, pp 11-29.

Soydemir, C., S.R. Kraemer, W.A. Davidson, and K.E LaPlante (1998) "Geotechnical earthquake engineering design of Charles River Bridges in Boston.," *Proc., 3rd Int. Conf. on Geotechnical Earthquake Engineering and Soil Dynamics*. University of Washington, Seattle, WA.: ASCE, pp 1235-1246.

Taboada-Urtuzuastegui, V., and R. Dobry (1998) "Centrifuge Modeling of Earthquake-Induced lateral spreading in Sand,," *Journal of Geotechnical and Geoenvironmental Engineering*, Vol. 124, No. 12, pp 1195-1206.

Tokida, K., H. Iwasaki, H. Matsumoto, and T. Hamasa (1993). "Liquefaction potential and drag force acting on piles in flowing soils, Soil Dynamic and Earthquake Engineering, Computational Mechanics, (South Hampton, England), 349-364

Ubilla, J., Abdoun, T., and Dobry, R. (2011). "Centrifuge scaling laws of pile response to lateral spreading." International Journal of Physical Modelling in Geotechnics, 11(1), 2-22.

Vucetic, Mladen, and Ricardo Dobry (1991) "Effect of soil plasticity on cyclic response," *Journal of Geotechnical Engineering*, Vol. 117, No. 1, pp 87-107.

Weaver, T., Ashford, S., and Rollins, K. (2005). "Response of 0.6 m cast-in-steel-shell pile in liquefied soil under lateral loading." Journal of Geotechnical and Geoenvironmental Engineering, 131(1), 94–102.

Wang, T. J. and Reese, L. C. (1998). " Design of pile foundations in liquefied soil" Pub. No. 75, ASCE, Geotech, Earthquake Engineering and Soil Dynamics Conf., Seattle, WA, Vol. 2, Aug., 1331-1343.

Wilson, D. W., Boulanger, R. W., and Kutter, B. L. (2000). “Seismic lateral resistance of liquefying sand.” J. of Geotechnical & Geoenvironmental Engrg., ASCE, Vol. 126, No.10, pp. 898-906.

Wilson, E. (2005) "Dynamic analysis by numerical integration," In: E. Wilson, Ed., *Technical Reports*. San Francisco, California: Computers and Structures Inc.

Yamada, S., M. Hyodo, R. Orense, Dinesh S. V, and T. Hyodo (2008) "Strain-Dependent Dynamic Properties of Remolded Sand-Clay Mixtures," *Journal of Geotechnical and Geoenvironmental Engineering*, Vol. 134, No. 7, pp 972-981.

Yang, Z. (2000) "Numerical Modeling of Earthquake Site Response Including Dilation and Liquefaction," *Civil and Environmental Engineering*. New York, NY: Columbia University.

Yang, Z., and A. Elgamal (2002) "Influence of Permeability on Liquefaction-Induced Shear Deformation," *Journal of Engineering Mechanics, ASCE*, Vol. 128, No. 7, pp 720-729.

Youd, T. L., C. M. Hansen, and S. F. Bartlett (2002) "Revised multilinear regression equations for prediction of lateral spread displacement.," *Journal of Geotechnical and Geoenvironmental Engineering*, Vol. 128, No. 12, pp 1007-1017.

Youd, T.L, and Hoose, S.N., (1978). Historic Ground Failures in Northern California Triggered by Earthquakes: U.S. Geological Survey Professional Paper 993, 175 pp.

Youd, T.L., and D.M. Perkins (1987) "Mapping liquefaction-induced ground failure potential," *Journal of the Geotechnical Engineering Division, American Society of Civil Engineers*, Vol. 104, No. GT4. , pp 433-446.

Zekkos, D., Jonathan D Bray, and M. F. Riemer (2006) "Shear modulus and material damping of municipal solid waste based on large-scale cyclic triaxial testing," *Canadian Geotechnical Journal*, Vol. 45, No. 1, pp 45-58.

Zhang, F., M. Kimura, T. Nakai, and T. Hoshikawa (2000) "Mechanical behavior of pile foundations subjected to cyclic lateral loading up to the ultimate state," *Soils and Foundations*, Vol. 40, No. 5, pp 1–17.

Zhang, G. , P. K. Robertson, and R. W. I. Brachman (2004) "Estimating Liquefaction-Induced Lateral Displacements Using the Standard Penetration Test or Cone Penetration Test," *Journal of Geotechnical and Geoenvironmental Engineering*, Vol. 130, No. 8, pp 861-871.

Zhang, J., R. D. Andrus, and C. H. Juang (2005) "Normalized shear modulus and material damping ratio relationships," *Journal of Geotechnical and Geoenvironmental Engineering*, Vol. 131, No. 4, pp 453-460.

APPENDIX A

If $[B]^k = [A]$ and $[A]$ has a matrix of similitude definite diagonal matrix $[D] = diag\{d_j\}$

$[A]$ matrix can be obtained as:

$$[A] = [P][D][P]^{-1} \quad \text{(Eq. 2A 1)}$$

On the other hand $[B]$ can be found to be:

$$[B] = [P][D]^{1/k}[P]^{-1} = [P]\{d_j^{1/k}\}^{1/k}[P]^{-1} \quad \text{(Eq. 2A 2)}$$

Where [P] is a transformation matrix of similitude.

The eigenvalues of matrix [A] are not affected by this transformation. As a result of the previous statement the diagonal [D] should contain all the eigenvalues of matrix [A].

Therefore,

$$[A]^{1/k} = [B] = [P][D]^{1/k}[P]^{-1} = [P]\{d_j^{1/k}\}^{1/k}[P]^{-1} \quad \text{(Eq. 2A 3)}$$

In the problem solved mass, damping and stiffness matrices are symmetrical and positive definite. The dynamical system has eigenvalues ω and normalized eigenvectors Φ. Eigenvalues and normalized eigenvectors have the following relationships with the mass and stiffness matrices respectively:

$$[\Phi]^T[M][\Phi] = [I] \ , \ [\Phi]^T[K][\Phi] = diag\{\omega_j^2\} \quad \text{(Eq. 2A 4)}$$

Because real modes of the system are orthogonal

$$[M]^{-1} = [\Phi][\Phi]^T \ , \ [K] = [\Phi]^{-T} diag\{\omega_j^2\}[\Phi]^{-1} \quad \text{(Eq. 2A 5)}$$

As a result:

$$[M]^{-1}[K] = [\Phi]diag\{\omega_j^2\}[\Phi]^{-1} \quad \text{(Eq. 2A 6)}$$

Based on the results of (Eq. 2A 3 it can be obtained that:

$$\left([M]^{-1}[K]\right)^{1/k} = [\Phi]diag\{\omega_j^{2/k}\}[\Phi]^{-1} \quad \text{(Eq. 2A 7)}$$

Damping matrix [C] is calculated using the following equation:

$$[C] = [M] \sum_{b=0}^{N-1} a_b \left([M]^{-1} [K] \right)^b \qquad \text{(Eq. 2A 8)}$$

If the term b of (Eq. 2A 8 is equal only to ½ the damping matrix can be calculated as:

$$[C] = [M] \; a_{1/2} [\Phi] diag\{\omega_j\} [\Phi]^{-1} \qquad \text{(Eq. 2A 9)}$$

APPENDIX B

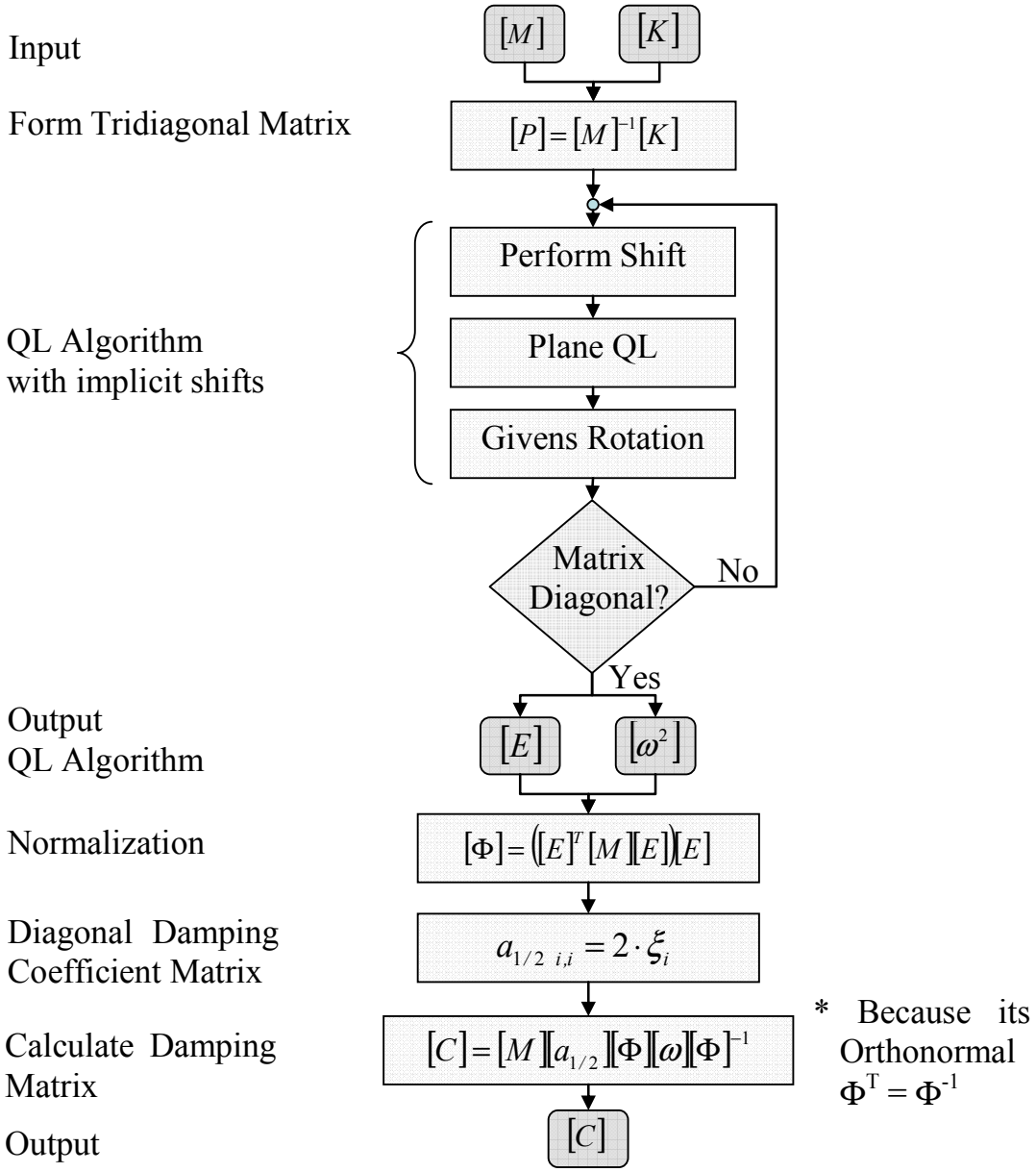
Input
[M]
[K]
Form Tridiagonal Matrix
[P] = [M]^-1 [K]
QL Algorithm
with implicit shifts
Perform Shift
Plane QL
Givens Rotation
Matrix
Diagonal?
No
Yes
Output
QL Algorithm
[E]
[ω²]
Normalization
[Φ] = ([E]^T [M][E])[E]
Diagonal Damping
Coefficient Matrix
a_1/2 i,i = 2 · ξ_i
Calculate Damping
Matrix
[C] = [M][a_1/2][Φ][ω][Φ]^-1
* Because its
Orthonormal
Φ^T = Φ^-1
Output
[C]

APPENDIX C

No	Reference	Year	Description	β	s	γ_r	ξ_{small} [%]	p_1	p_2	p_3	R^2 G/Go	R^2 ξ
1	Vucetic and Dobry	1991	PI = 0	1.000	0.870	0.031	0.882	0.940	0.380	0.550	0.999	1.000
2	Vucetic and Dobry	1991	PI = 15	1.000	0.810	0.070	0.913	0.980	0.380	0.700	0.999	0.997
3	Vucetic and Dobry	1991	PI = 30	1.000	0.810	0.139	0.953	0.960	0.360	0.500	0.999	0.993
4	Vucetic and Dobry	1991	PI = 50	1.000	0.840	0.276	0.979	0.920	0.380	0.500	0.999	0.990
5	Vucetic and Dobry	1991	PI = 100	1.000	0.930	0.562	0.996	0.660	0.280	1.000	0.998	0.991
6	Vucetic and Dobry	1991	PI = 200	1.000	1.140	0.897	1.000	0.600	0.360	0.950	0.999	0.986
7	Boulanger	1998	Sherman Island Peat	0.330	0.840	0.278	1.994	0.820	0.380	1.400	0.995	0.981
8	Seed & Idriss	1970	Upper	1.000	0.930	0.060	0.204	0.700	0.200	0.600	0.999	0.998
9	Seed & Idriss	1970	Mean	1.000	0.870	0.040	0.381	0.980	0.380	1.850	0.999	0.998
10	Seed & Idriss	1970	Lower	1.060	0.810	0.024	0.533	0.980	0.280	3.200	0.999	0.993
11	Zhang et al.	2005	Quaternary Soil PI =0	1.560	0.810	0.139	0.239	0.780	0.280	3.100	0.999	1.000
12	Zhang et al.	2005	Tertiary Soil PI = 0	1.558	0.960	0.053	0.251	0.660	0.260	3.200	0.999	0.999
13	Zhang et al.	2005	Residual Soil PI =0	1.570	0.810	0.076	0.190	0.860	0.320	1.600	0.999	1.000
14	Zhang et al.	2005	Quaternary PI = 15	1.570	0.780	0.170	1.440	0.740	0.200	2.150	1.000	0.997
15	Zhang et al.	2005	Quaternary PI = 30	1.570	0.810	0.194	1.458	0.700	0.200	2.800	1.000	0.996
16	Zhang et al.	2005	Quaternary PI = 50	1.564	0.900	0.214	1.481	0.640	0.240	3.100	1.000	0.998
17	Zhang et al.	2005	Quaternary PI = 100	1.570	0.930	0.318	1.489	0.680	0.300	3.050	1.000	0.998
18	Zekkos et al.	2006	100%<20mm	0.750	0.870	0.095	2.977	0.640	0.200	3.200	1.000	0.999
19	Zekkos et al.	2006	62-76%<20mm	0.750	0.720	0.222	3.966	0.720	0.200	0.650	0.998	0.996
20	Zekkos et al.	2006	8-25%<20mm	0.750	0.780	0.642	3.991	0.640	0.200	0.500	0.999	1.000
21	Borja et al.	2000	6m	1.320	0.990	0.048	3.450	0.840	0.380	3.000	0.996	0.979
22	Borja et al.	2000	11m	1.300	0.870	0.045	1.385	0.980	0.380	2.300	0.998	0.988
23	Borja et al.	2000	17m	1.270	0.720	0.046	1.261	0.980	0.200	4.000	0.999	0.986
24	Darendeli	2001	σ_0' = 0.25 atm - SM	0.980	0.870	0.019	0.977	0.660	0.240	3.000	1.000	0.999
25	Darendeli	2001	σ_0' = 1.0 atm - SM	0.980	0.840	0.036	0.717	0.660	0.220	3.000	1.000	0.999
26	Darendeli	2001	σ_0' = 4.0 atm - SM	1.000	0.840	0.072	0.552	0.660	0.220	3.000	0.999	0.998
27	Darendeli	2001	σ_0' = 16.0 atm - SM	1.000	0.840	0.151	0.575	0.660	0.220	3.000	1.000	0.999
28	Yamada et al.	2008	Dejima Clay Fc = 99.1%	1.000	0.990	0.202	1.093	0.660	0.380	1.100	0.999	0.998
29	Yamada et al.	2008	Dejima Clay Fc = 43.0%	1.000	1.020	0.066	1.484	0.600	0.320	1.650	1.000	0.998
30	Okur & Ansal	2007	PI = 12%	0.750	0.990	0.043	2.878	0.600	0.280	0.500	1.000	0.964
31	Okur & Ansal	2007	PI = 27%	0.756	0.960	0.083	1.986	0.600	0.280	0.550	1.000	0.972
32	Okur & Ansal	2007	PI = 43%	0.748	0.990	0.150	1.393	0.620	0.340	1.500	0.998	0.978
33	Kramer	2000	Mercer Slough peat*	1.020	0.840	0.027	2.857	0.900	0.380	0.500	0.994	0.998
34	Bozzano et. al	2008	Roma's Clay	0.900	1.290	0.138	1.898	0.980	0.300	4.000	1.000	0.989
35	Crespellani et al.	2001	Roma's Clay	0.930	1.200	0.041	4.986	0.920	0.380	3.100	1.000	0.995
36	Carrubba & Maugeri	1999	Roma's Clay	0.750	1.230	0.153	1.999	0.600	0.300	1.300	1.000	0.990
37	Cardona & Yamin	1997	PI=20	1.560	0.660	0.225	2.891	0.760	0.200	2.600	1.000	0.989
38	Cardona & Yamin	1997	PI=40	1.500	0.750	0.338	2.963	0.660	0.200	3.250	1.000	0.993
39	Cardona & Yamin	1997	PI=60	1.560	0.840	0.442	2.985	0.600	0.200	2.350	1.000	0.993
40	Cardona & Yamin	1997	PI=80	1.580	0.870	0.533	2.990	0.600	0.240	3.050	1.000	0.990

No	Reference	Year	Description	β	s	γ_r	ξ_{small} [%]	p_1	p_2	p_3	R^2 G/Go	R^2 ξ
41	Cardona & Yamin	1997	PI=100	1.600	0.900	0.608	2.993	0.600	0.240	2.200	1.000	0.989
42	Cardona & Yamin	1997	PI=150	1.460	0.960	0.649	2.996	0.620	0.280	1.350	1.000	0.988
43	Darendeli	2001	PI=0 /σ'v = 50 kPa	1.000	0.930	0.025	1.031	0.700	0.320	2.550	1.000	0.992
44	Darendeli	2001	PI=0 / σ v = 100 kPa	1.000	0.930	0.031	0.848	0.680	0.300	2.800	1.000	0.994
45	Darendeli	2001	PI=0 / σ 'v = 500 kPa	1.000	0.900	0.057	0.528	0.660	0.280	3.000	1.000	0.996
46	Darendeli	2001	PI=0 / σ v = 1000 kPa	1.000	0.900	0.073	0.436	0.660	0.240	3.100	1.000	0.997
47	Darendeli	2001	PI=20	1.000	0.930	0.050	1.132	0.640	0.240	3.500	1.000	0.996
48	Darendeli	2001	PI=50	1.000	0.930	0.078	1.554	0.640	0.240	3.500	1.000	0.997
49	Darendeli	2001	PI=100	1.000	0.900	0.124	2.260	0.640	0.220	3.500	1.000	0.998
50	Darendeli	2001	PI=200	1.000	0.900	0.215	3.658	0.640	0.200	3.500	1.000	0.999